A DECADE OF EMISSIONS CONTROLS AND THEIR ROLE ON AN EVER-CHANGING ATMOSPHERE

A Dissertation
Presented to
The Academic Faculty

By

Petros Vasilakos

In Partial Fulfillment
Of the Requirements for the Degree
Doctor of Philosophy in Chemical Engineering

Georgia Institute of Technology

May 2018

A DECADE OF EMISSIONS CONTROLS AND THEIR ROLE ON AN EVER-CHANGING ATMOSPHERE

Approved by:

Professor Athanasios Nenes, Advisor
School of Chemical & Biomolecular Engineering and School of Earth & Atmospheric Sciences
Georgia Institute of Technology

Professor Armistead G. Russell
School of Civil & Environmental Engineering
Georgia Institute of Technology

Professor Nga L. Ng
School of Chemical & Biomolecular Engineering and School of Earth & Atmospheric Sciences
Georgia Institute of Technology

Professor Matthew J. Realff
School of Chemical & Biomolecular Engineering
Georgia Institute of Technology

Professor Ryan P. Lively
School of Chemical & Biomolecular Engineering
Georgia Institute of Technology

Date approved: 14 March 2018

THANKS

Many people have helped me throughout my graduate years; without them, this thesis would have not been made possible. Above all, I want to thank my parents and my brother for always being there for me every time I needed them and for all their sacrifices. They have acted as invaluable role-models throughout my life and I have been extremely fortunate to be blessed with them; I would not be the man I am today without them. My two advisors, Athanasios Nenes and Armistead Russell, for patiently mentoring me and turning me into a researcher. Yongtao Hu and Marcus Trail, whose intimate knowledge of atmospheric models will accompany me in my professional years. The Nenes and Russell groups for providing an enabling environment to work in. All my friends here and back home, especially Michael Vlysidis, Thanos Lekkou and George Kotsalis for always lending an ear to my problems and their valuable advice. The Avgoustopoulos family for treating me as one of their own. Bruno Frazzato for initiating me in the art of jiu-jitsu. Yiannis Exarhos for introducing me to the gym and teaching me valuable lessons about being an adult. Becky for tending to all my athletic injuries in the last year and contributing to my well-being. The Georgia Tech and the CRC communities for being awesome. Finally, I would like to express my gratitude to the man in the mirror, for not buckling under the pressure of both life and graduate school; I came to graduate school as a boy but I leave a man.

ACKNOWLEDGEMENTS

TOMAS-RC paper

This work was funded by the Defense Threat Reduction Agency under grant number DTRA1-08-10-BRCWMD-BAA.

Texas-Louisiana air quality work

We acknowledge funding from the Phillips 66. Special thanks to Terry Lathem for his continuous support and research direction, as well as Yongtao Hu for planning a large part of this work.

SOAS paper

This project was funded from the Phillips 66 company. We thank Havala Pye of EPA for providing us with her updated version of CMAQ and for informal communication and guidance.

pH paper

We thank Hongyu Guo for providing us with data and personal discussions that helped shape the paper. We also thank the reviewers of ES&T for providing meaningful feedback that lead to a more scientifically sound and complete paper.

TABLE OF CONTENTS

LIST OF TABLES

LIST OF FIGURES

SUMMARY

The first part of the thesis, looks at the impact that radioactive charging effects can have on aerosol lifetime. The TOMAS microphysics model (Adams & Seinfeld, 2002) is updated to account for interactions between particles that are charged through radioactive decay, and then used to elucidate the impact of charging on particle lifetime and subsequent potential travel distances. It is found that for most cases radioactive charging has a negligible effect on particles, but it can have an appreciable effect when concentrations and sizes are large.

Industrial sources heavily impact ozone and $PM_{2.5}$ concentrations, although their exact impact is not always well understood. To gauge the impact of such sources on important criteria pollutants, the Community Multiscale Air Quality (CMAQ) model with a sensitivity method, in this case the Decoupled Direct Method (Dunker, 1984), is used to identify the exact spatio-temporal patterns of ozone and $PM_{2.5}$ attributed to specific facilities operated by Phillips 66. To that end, an array of different scenarios has been simulated for 2012 and 2017 using the 2017 National Emissions Inventory (NEI), complemented with expansion plan data provided by Phillips 66. Separate sensitivity simulations were carried out to quantify the impact of expansion emissions on ozone and $PM_{2.5}$. A major finding is that ozone formation shifts from a VOC limited regime to a NO_x limited one between the two years, suggestive of diminishing returns for NO_x reductions. Therefore, VOC controls in the future could prove more effective in reducing the impact of industrial activities on ozone concentrations.

Apart from controlling ozone and $PM_{2.5}$, emissions from industrial activities also interact with biogenic precursors and form Secondary Organic Aerosol (SOA), a family of species that is a significant contributor to $PM_{2.5}$ concentrations. To account for such interactions, the CMAQ model was modified to better represent SOA chemistry, using the rich dataset obtained during the Southern Oxidant Aerosol Study (SOAS) field campaign. This was achieved through updates to the existing chemical mechanism, emission improvements and a variety of sensitivity tests aimed at determining an optimal value for the Henry's law constant. With regards to SOA production, our findings indicate that there exists an almost linear relationship between isoprene SOA levels and sulfate concentrations. Further reductions in SO_2 emissions are found to reduce isoprene SOA significantly, which, should be taken into account for future regulatory purposes.

To further elucidate the impact of industrial emissions on $PM_{2.5}$, we looked at aerosol pH and its evolution throughout a decade of emission controls from 2001 to 2011. It has been hypothesized that SO_2 reductions would lead to more alkaline aerosol and a subsequent substitution of sulfate by nitrate as the dominant inorganic $PM_{2.5}$ constituent. An increasingly basic pH will also halt isoprene SOA production, which is strongly dependent on high acidity. By using CMAQ results and the thermodynamic model ISORROPIA, we identified inherent model biases, the major finding being that nonvolatile cations (NVCs) are present in quantities in excess of 1 $\mu g\ m^{-3}$, leading to a decadaly increasing pH trend, reduced SOA production and nitrate substitution. Removal of these cations lead to 2011 pH levels similar to these of 2001, while, at the same time, not predicting nitrate substitution.

CHAPTER I

INTRODUCTION

Aerosols are solid or aqueous particles produced in the atmosphere through a variety of mechanisms, by both anthropogenic activities and natural processes. These microscopic particles play a large role in modulating climate and air quality, through their effects on cloud properties, visibility and human health. Of particular interest are particles emitted by radioactive processes and industrial sources, since they can have some of the most adverse effects on human health, and, although heavily regulated, their lifetime and physical properties are still not entirely understood. To study these particles, various models have been developed, encompassing a multitude of scales, from the microphysical processes that aerosols undergo on a scale of seconds, to their decadal impact on climate change.

On a microphysics scale, radioactive particles behave differently than non-radioactive particles. The constant decay of such aerosol leads to charged populations, which in turn changes their fundamental properties and lifetimes in the atmosphere (Simons, 1981; Clement et al., 1995; Clement & Harrison, 1992; Harrison & Carslaw, 2003; Kim et al., 2014, 2015, 2016). Accurate prediction of the atmospheric lifetimes and dispersion patterns of radioactive particles is necessary in order to minimize the impact of catastrophic events such nuclear reactor meltdowns. Current models that deal with the dispersion of radioactive material do not account for radioactive charging, often leading to predicted plume trajectories that do not match the ones observed (Yoshenko et al., 2006; Christoudias et al., 2013).

On a regional scale, Chemical Transport Models (CTMs) couple meteorology and emissions, allowing pollutants to undergo various removal and formation processes such as coagulation, while tracking their transport and lifetime. CTMs have long been used to study these particles and assist policy makers in their decision making, with significant advances being made in recent years with regards to the physics that they include, leading to increased accuracy. However, since there is a multitude of processes that particulates undergo, from complex chemical reactions to their activation of becoming droplets, it is not possible for even the state-of-the-art models to capture all the interactions. For instance, while ozone and $PM_{2.5}$ formation has been studied since the 70s, driven by the seminal work of Haagen-Smit (Haagen-Smit & Fox, 1994) and the Whitby group (Husar et al. 1971) , and a lot of progress has been made on our understanding of the pathways that lead to ozone production, CTMs such as CMAQ remain biased, exhibiting a tendency to overestimate ambient ozone concentration levels (Travis et al. 2016). Another example is the case of isoprene, a biogenic VOC with yearly global emissions up to 750 Tg yr^{-1} (Guenther et al. 2006). For many years isoprene was thought to not contribute significantly to the total organic mass (OM), with terpenes being considered the dominant contributor to OM (Acosta et al. 2013). Recently however, it was found that particulates derived from isoprene reactions can contribute up to 50% of the total OM (Xu et al. 2015), underlying our incomplete understanding of the diverse chemistry that takes place in the atmosphere. Since then, models have been updated to represent these findings (Pye et al. 2013, Marais et al. 2016), but significant room for improvement remains. Another area with where major breakthroughs have been made recently is the fledging field of aerosol pH. Much of the chemistry that takes place in the atmosphere, occurs in the aqueous phase. pH being a

fundamental property of liquids, can play an important role in chemistry; for example the IEPOX pathway for isoprene heavily relies on highly acidic conditions (Xu et al. 2015). In addition, acidity levels can modulate partitioning of gas phase species in the aerosol such as nitrate (Weber et al. 2016). Despite this, models are scarcely evaluated on their ability to predict aerosol acidity, and this can give rise to many biases from underpredicted organic mass, to substitution of sulfate aerosol by nitrate.

Given the dependence of aerosol pH and SOA formation on industrial emissions, as well as the rapidly changing atmospheric conditions due to emission controls, it is of paramount importance to elucidate the impact that industrial emissions have on these processes. SO_2 a common aerosol precursor, mainly emitted from industrial sources, is converted to sulfate through atmospheric processing, a specie that plays an active role on modulating aerosol pH, while also interacting with isoprene from vegetation to form SOA. The efficacy of this route to produce SOA is directly tied to sulfate levels, as well as aerosol pH – which is also directly controlled by sulfate - pointing to highly complex interactions between air pollution and background precursors.

The goal of this thesis, is to update existing models in order to alleviate many of the inherent biases in them, and then use the improved versions to better understand the impact that emission control strategies had on the atmosphere. Chapter 2 describes updates made to the TOMAS microphysics model to account for the charging of radioactive particles, in order to determine and quantify the impact that such effects have on the lifetime of these particles. In Chapter 3, the Direct Decoupled Method (DDM) – a sensitivity method that quantifies the impact of emission sources on pollutant concentrations - is used for the case study of Phillips 66 facilities in Texas & Louisiana.

Quantification of the impact that anthropogenic sources have on ozone and $PM_{2.5}$ is necessary for policy making, in line with the State Implementation Plan (SIP), since, many counties in these two states are frequently in non-attainment for these two species. Chapter 4 deals with the negative biases of isoprene derived aerosol in CMAQ. Using observations from the Southern Oxidant and Aerosol Study (SOAS) many model updates were made to the chemistry processor, in order to better represent isoprene chemistry, and the updated model was afterwards used to determine the impact of future SO_2 emission controls on SOA formation. Chapter 5 identifies biases in CMAQ that lead to incorrect pH predictions in the model, which in turn adversely affects the model's ability to correctly predict nitrate. After the alleviation of these biases, the validity of the nitrate substitution hypothesis is refuted, and the potential role that organic acids can play on aerosol pH quantified. Finally, Chapter 6, presents future research directions stemming from using the updated models and the tools developed in this thesis.

CHAPTER 2

STUDYING THE IMPACT OF RADIOACTIVE CHARGING ON THE MICROPHYSICAL EVOLUTION AND TRANSPORT OF RADIOACTIVE AEROSOLS

The objective of this chapter is to determine the influence of radioactive charging on the vertical transport of radioactive aerosols in the atmosphere, through its effect on coagulation and deposition, as well as quantify the impact of this charging on aerosol lifetime. Radioactive charging can significantly impact the way radioactive aerosols behave, and as a result their lifetime, but such effects are neglected in predictive model studies of radioactive plumes. The TwO-Moment Aerosol Sectional (TOMAS) microphysical model was extended to account for radioactive charging effects on coagulation in a computationally efficient way. The expanded model, TOMAS-RC (TOMAS with Radioactive Charging effects), was then used to simulate the microphysical evolution and deposition of radioactive aerosol (containing the isotopes ^{131}I and ^{137}Cs) in a number of idealized atmospheric transport experiments. Results indicate that radioactive charging can facilitate or suppress coagulation of radioactive aerosols, thus influencing the deposition patterns and total amount of radioactive aerosol mass available for long-range transport. Sensitivity simulations to uncertain parameters affirm the potential importance of radioactive charging effects. An important finding is that charging of neutral, coarse mode aerosol from background radiation can reduce coagulation rates and extend its lifetime in the atmosphere by up to a factor of 2.

2.1. Introduction

Human activities and events can release large amounts of radioactive particles into the atmosphere; nuclear reactor meltdowns such as the Fukushima and Chernobyl accidents, weapon tests, radioactive waste treatment, as well as coal fired power plants constitute important sources of airborne radionuclides (Chesser et al., 2004; Lujaniene et al., 2007; Yoshida & Kanda, 2012; McBride et al., 1977; Mulpuru et al., 1992). The impacts of this radioactivity on the environment and human health depends largely on where it deposits, and underscores the need for its accurate prediction for policy and first response efforts to accidents and other release events.

Aerosols carrying radionuclides can spontaneously accumulate electrostatic charge, which affects their microphysical evolution in the atmosphere. Because of this, radioactive aerosol can exhibit a distinctly different behavior when compared to non-radioactive (and neutral) aerosol (Simons, 1981; Clement et al., 1995; Clement & Harrison, 1992; Harrison & Carslaw, 2003; Kim et al., 2014, 2015, 2016). Considering charging effects of radioactive aerosols immediately impacts their initial deposition patterns, and following the resistances in series model described in Seinfeld & Pandis (2006), it is expected that areas affected by radioactivity would present different surface resistances to charged aerosol populations. Therefore, the deposition rate for particles of a given size can be enhanced/reduced close to a radioactive surface. Secondary resuspension and redistribution mechanisms from wild fires, dust events and water runoff downwind of nuclear accidents (Lujanienė et al., 2007; Adeyini & Oladiran, 2007; Yoshenko et al., 2006; Yoshenko et al. 2006; Masson et al., 2011), all contribute to the long-term impacts of release events and

are affected by where the primary deposition of radionuclides occur. For example, extensive forest fires between May and August of 1992 in the 30-km ring surrounding the Chernobyl-exclusion zone are known to have emitted radioactive aerosols to the atmosphere, detectable at considerable distances (Lujanienė et al., 2007; Ooe et al., 1988). As a result, important secondary contamination was found in areas that were initially not contaminated by radioactivity. The remobilized radionuclides deposited after wild fires were more concentrated and water-soluble, and therefore easily redistributable by water runoff into subsurface water systems (Lujanienė et al., 2007; Yoshenko et al., 2006).

Charging of radioactive aerosols occurs from the decay of radionuclides, which can be in either the form of α or β emission (Clement & Harrison, 1992). For alpha emission, an alpha particle of a charge of +2 is ejected from the aerosol, leaving a residual charge of -2. Nevertheless, in general, radioactive aerosols undergoing alpha decay become positively charged because alpha particles can cause significant ionization within the aerosols, which leads to the emission of secondary electrons. In β-decay, the emission of energetic electrons results in a residual charge of +1. These ions ejected and transferred their kinetic energy to the gas phase can combine with surrounding gas molecules or other aerosols through collision/adsorption, thereby producing many ion pairs and charged aerosols. Renard et al. (2013) found that many large aerosols in the upper troposphere and stratosphere can be easily charged by diffusion of ions, and the aerosols may gain more charges as their size increases. Negative ions produced from ionizing radiation tend to exhibit a higher mobility than positive ions produced (Gunn, 1954; Mohnen, 1976); this asymmetry in mobility leads to the charging of aerosols through the diffusion of ions onto their surface, with a surplus of negative gas-phase ions over positively charged ions. Ion

mobilities are dependent upon the molecular weight, temperature and pressure of the surrounding gas (Harrison & Carslaw, 2003; Mohnen, 1976; Clement & Harrison, 1992). Therefore, variability of these factors can lead to a range of mobilities, and charging (Clement & Harrison, 1992). The direct ionization of particles from radioactive decay is called "self-charging", while collision/adsorption of gas-phase ions generated by the radioactive decay is called "diffusion charging" (Harrison & Carslaw, 2003; Clement et al., 1995; Clement & Harrison, 1992; Kim et al., 2014, 2015, 2016).

Because radioactive aerosols can be easily discharged by ionizing radiation (Greenfield, 1956), as well as neutralized by ions produced in the containment atmosphere (Clement et al., 1995; Clement & Harrison, 1992), the effects of electrostatic interactions on microphysical processes of aerosols have been frequently neglected (e.g., Greenfield, 1957). However, many radioactive aerosols can be appreciably charged in open air (Kim et al., 2015), suggesting that several microphysical processes of the aerosols can be affected by radioactive charging causing electrostatic interactions [e.g., coagulation (Clement et al., 1995; Kim et al., 2014, 2016)] and impacting the rate of wet scavenging (Tripathi and Harrison, 2001; Sow and Lemaitre, 2017). Chemical transport models (CTMs) with explicit aerosol microphysics are well-posed to consider all the relevant processes that control the transport and deposition of radioactive aerosol (e.g., condensation/evaporation of semi-volatile species, coagulation of particles, cloud processing, wet/dry deposition and horizontal/vertical transport). State-of-the-art atmospheric models, however, do not account for radioactivity impacts on aerosol microphysics (e.g., Yoshenko et al., 2006; Christoudias et al., 2013). This omission introduces an unknown, and potentially important, bias in the predicted deposition patterns following a radioactivity release event.

This chapter is an initial step to develop a comprehensive atmospheric modeling approach to account for the effects of radioactive charging on the microphysical evolution, transport and deposition of radioactive aerosol from the atmosphere. The established TwO-Moment Aerosol Sectional (TOMAS) aerosol microphysical model (Adams & Seinfeld, 2002) is used to simulate the microphysical evolution of atmospheric particulate matter, and is augmented to include electrostatic particle-particle interactions in the presence of radioactive charging. The expanded model, called TOMAS-RC (TOMAS with Radioactive Charging effects) is used to study, with idealized simulations, situations where charging exerts an important influence on the transport and deposition of radioactive particles.

2.2. Methods

2.2.1 TOMAS aerosol microphysical model

The version of the TOMAS model (Adams & Seinfeld, 2002) used here has a resolution of 30 bins, covering particle sizes from 10 nm to 10 μm. TOMAS accounts for all the relevant atmospheric processes of nucleation, condensation, coagulation, vertical mixing, cloud processing and deposition, in order to find the number concentration and size distribution of the modeled aerosol. For the needs of this study only dry deposition, vertical mixing and coagulation were active. TOMAS tracks two independent moments, number and mass, of the aerosol size distribution for each size bin:

$$N_k = \int_{x_k}^{x_{k+1}} n_k(x)dx \quad (1)$$

$$M_k = \int_{x_k}^{x_{k+1}} x n_k(x)dx \quad (2)$$

where N_k, M_k are the total number and mass of aerosol in the *k*-sized bin, $n_k(x)$ is the number of particles with masses included between $x + dx$, and x_k is the lowest boundary of the k^{th} bin. The lowest and the largest boundaries of each cell are defined in terms of

dry aerosol mass, in such a way that the largest boundary has double the mass of the lowest boundary, something that allows for considerable gains in computational efficiency (Adams & Seinfeld, 2002). A detailed description of TOMAS is available elsewhere (Adams & Seinfeld, 2002; Lee & Adams, 2012).

The aerosol size distributions are influenced by microphysical processes (e.g., deposition, vertical layer mixing, and coagulation) occurring in each computational cell. The rate of change for N_k and M_k resulting from coagulation, which is a process modulated by radioactive charging, are given by (Fuchs, 1964; Tzivion et al., 1987, Adams and Seinfeld, 2002):

$$\frac{dN_k}{dt} = 0.5K_{k-1,k-1}{N_{k-1}}^2 - K_{k,k}{N_k}^2 - N_k\sum_{i=k+1}^{I} K_{k,i}N_i + \psi_{k-1}\sum_{i=1}^{k-2} K_{k-1,i}M_i$$
$$-\psi_{k-1}\sum_{i=1}^{k-1} K_{k,i}M_i - \frac{\psi_{k-1}-f_{k-1}}{2x_{k-1}}\xi\sum_{i=1}^{k-1} K_{k,i}M_i\, m_i - \frac{\psi_{k-1}-f_{k-1}}{2x_{k-1}}\xi\sum_{i=1}^{k-2} K_{k-1,i}M_i\, m_i$$

(3)

$$\frac{dM_k}{dt} = K_{k-1,k-1}N_{k-1}M_{k-1} - K_{k,k}N_kM_k + N_k\sum_{i=1}^{k-1} K_{k,i}M_i - M_k\sum_{i=k+1}^{I} K_{k,i}N_i$$
$$+\psi_{k-1}x_k\sum_{i=1}^{k-2} K_{k-1,i}M_i - \psi_k x_{k+1}\sum_{i=1}^{k-1} K_{k,i}M_i + \frac{f_{k-1}}{2}\xi\sum_{i=1}^{k-2} K_{k-1,i}M_i\, m_i$$
$$-\frac{f_k}{2}\xi\sum_{i=1}^{k-1} K_{k,i}M_i\, m_i + \frac{\psi_k-f_k}{2x_k}\xi^3\sum_{i=1}^{k-1} K_{k,i}M_i\, {m_i}^2 - \frac{\psi_{k-1}-f_{k-1}}{2x_{k-1}}\xi^3\sum_{i=1}^{k-2} K_{k-1,i}M_i\, {m_i}^2$$

(4)

where i and k represent the size bins between which coagulation takes place, $K_{k,i}$ is the coagulation coefficient between these two bins, I is the total number of size bins which is equal to 30 for this case, ψ and f are weighting factors described in Tzivion et al. 1987, ξ is the closure parameter determined size range of each bin (here, ξ = 1.0625), x is the lowest dry mass boundary of the cell, m_i is the average particle mass in bin i, and t is the time.

In Eqs. (3) and (4), the coagulation coefficient, K, is the parameter controlling the coagulation rate of aerosols, and it can be affected by several collision mechanisms

involving interparticle forces and flow regimes (Seinfeld and Pandis, 2006). In TOMAS, it is assumed that Brownian motion is the dominant collision mechanism (Adams & Seinfeld, 2002; Lee & Adams, 2012), and the coagulation coefficient is obtained using the interpolation formula of Fuchs (1964) to consider aerosol coagulation in the continuum, transition, and free molecular regimes. In TOMAS-RC, the Brownian coagulation coefficient is augmented to include the effects of radioactive charging, following the suggestions of Clement et al. (1995); Kim et al. (2016), and as described below.

2.2.2 Coagulation of radioactive aerosols

Charging effects on the coagulation rate between particles *i* and *k* are introduced through a "correction factor" multiplier, $\bar{W}_{k,i}$, applied to the Brownian coagulation kernel at each aerosol microphysical step (Fig. 2.1). $\bar{W}_{k,i}$ in TOMAS-RC is based on the "stability function" correction factor formulation neglecting the effects of image forces (Fuchs, 1964; Spellman, 1970; Seinfeld & Pandis, 2006):

$$W_{k,i} = \frac{\gamma}{e^{\gamma}-1} \tag{5}$$

with $\gamma = \frac{j_k j_i e^2}{4\pi\varepsilon_0 \varepsilon (r_k + r_i) k_B T}$, j_k, j_i are the charges of particle *k* and *i* respectively, *e* is the elementary electrical charge, ε_0 is the electrical permittivity of vacuum and ε is the dielectric constant of air. Also, r_k and r_i are the radii of aerosol particles *k* and *i*, respectively, k_B is the Boltzmann constant, and *T* is the temperature. $W_{k,i}$ is applied as an enhancement factor to the Brownian kernel; as the charge of either the colliding particles approaches zero (i.e., $j_k j_i \rightarrow 0$), $\gamma \rightarrow 0$ and $W_{k,i} \rightarrow 1$ (because $e^{\gamma} \sim 1+\gamma$ for small γ), and thus, coagulation rates of the particles become similar to those expected from Brownian diffusion of neutral particles. This limit is relevant for the coagulation between small

particles that typically carry an average charge of less than 1 (γ<0.1), and subsequently their coagulation is not impacted by charging effects. In the case of particles with opposite sign charges, $\gamma<0$ and $W_{k,i}$>1 meaning that coagulation is enhanced; for particles with like charges, $\gamma>0$ and $W_{k,i}$<1 leading to inhibition of coagulation.

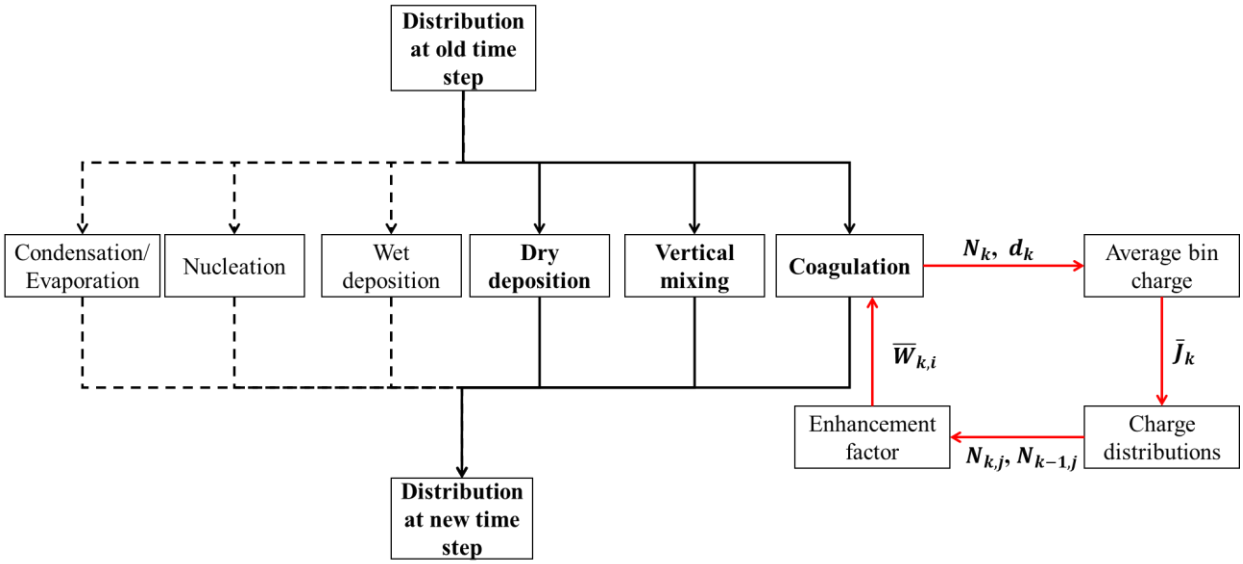

Figure 2.1 Flow diagram of the computational scheme in TOMAS-RC. The number concentration and diameter of each bin are passed from the coagulation subroutine to the aerosol charging subroutine, where the average charge and charge distributions are calculated, and then used to estimate the enhancement factor, which is returned to the TOMAS coagulation module. Processes in bold are the ones active in TOMAS-RC.

Equation (5) is derived assuming coagulation of charged particles in the continuum regime. The correction factor formulations for the transition and molecular regimes are available elsewhere [e.g., Marlow (1980) and Huang et al. (1990)]. Compared to these formulations, equation (5) is less accurate [e.g., up to 10% errors for the transition regime (Huang et al., 1990)]. In contrast to these formulations requiring high computational costs, however, equation (5) is much simpler and computationally more efficient, indicating that the equation may be more suitable for use in three-dimensional transport models. Also,

equation (5) has been used in various modeling and experimental investigations into coagulation of charged particles in the molecular and transition regimes [e.g., Maisels et al. (2002a, 2002b)] because the equation may still provide reliable computational results despite the possibility of errors. For instance, Maisels et al. (2002b) estimated the coagulation coefficient of charged particles in the transition regime using the interpolation formula of Fuchs (1964) and equation 5, and found that the calculation was in good agreement with the measurements. Thus, in this study, equation 5 was used to include the effects of particle charging on particle coagulation in all flow regimes.

Equation (5) depends strongly on the number of charges existing on the coagulating particles. An appropriate theory is therefore required to calculate at each coagulation timestep (Fig. 2.1) the number of charges that develop on the aerosol population. Kim et al. (2016) has evaluated an approach assuming a Gaussian distribution to approximate the charge distribution and found that the errors associated with such an assumption only become significant for particles with diameters smaller than 40 nm. An explicit representation of the charge distribution would be extremely computationally demanding when compared to a Gaussian, as demonstrated in Clement et al. (1995) and Kim et al. (2016). Furthermore, the average charge and deviation values used in the Gaussian distribution are approximated from the exact distributions (Clement & Harrison, 1992), which further reduce the error while achieving desirable computational efficiency. In the presence of self-charging and diffusion charging, the Gaussian distribution used to describe the charge distribution that develops for particles in each size bin *k* (Clement et al., 1995; Gensdarmes et al., 2001; Kim et al., 2016) is:

$$\frac{N_{kj}}{N_k} = \frac{1}{\sqrt{2\pi}\sigma_k} exp\left(-\frac{(j-\bar{J_k})^2}{2\sigma_k^2}\right) \quad (6)$$

where N_{kj} is the number concentration (m^{-3}) of aerosols in size bin k carrying charge j. N_k is the total number of particles in bin k ($N_k = \sum_j N_{kj}$) and $\bar{J}_k$, σ_κ are the mean aerosol charge and standard deviation of the aerosol charge distribution for size bin k, given by:

$$\sigma_k^2 = y_k + \frac{1}{2\omega_k} \;,\; \bar{J}_k = \begin{cases} y_k - \left(\frac{y_k(X-1)}{\exp(2\omega_k y_k - 1)}\right) & \omega_k y_k > 0.22 \\ y_k + \frac{X-1}{2\omega_k} & \omega_k y_k \leq 0.22 \end{cases} , y_k = \frac{\varepsilon_0 \eta_k}{e\mu_- n_0},$$

where $\omega_k = \frac{e^2}{8\pi\varepsilon_0 r_k k_b T}$ is a parameter describing the effects of diffusion charging, $X = \frac{\mu_+}{\mu_-}$ is the asymmetry/mobility ratio, μ_+ and μ_- are the mobilities of positive and negative ions, respectively ($m^2\ V^{-1}\ s^{-1}$), y_k is the positive charge accumulated via self-charging and n_0 is the total number of ions in the air. The Gaussian charge distribution we utilize has been used in previous literature reports (Clement & Harrison, 1992; Clement et al., 1995; Kim et al., 2016) as an approximation of the exact charge distribution calculated numerically in Clement & Harrison (1992). The normal distribution presents a simple, yet accurate representation of the charge distribution of radioactive aerosols [e.g., Gensdarmes et al.(2001)] . For the internally mixed aerosol populations presented here, the Gaussian distribution constitutes an accurate simplification of the steady-state charge distribution as shown in Kim et al. (2016). The size-dependent radioactive decay per particle (η_k), in each size bin, required to obtain y_k is determined from the specific radioactive decay rate η_0 for each species (Clement & Harrison, 1992):

$$\eta_k = \eta_0 r_k^3 \quad (7)$$

Calculation of y_k also requires the total number n_0 of ions (positive and negative) produced from natural radioactivity, cosmic rays, and decay of radionuclides attached to aerosols and is given by (Clement et al., 1995; Harrison & Carslaw, 2003):

$$n_0 = \sqrt{\frac{q_b + q_I}{\alpha_{rc}}}, \tag{8}$$

where q_b is the rate of ionization by radon and cosmic radiation, q_I is the rate of ionization caused by radioactive aerosols, and α_{rc} is the rate coefficient of ion-ion recombination.

Equation 6 applies to background aerosols as well; in this case $\eta_\kappa \rightarrow 0$ so $y_k \rightarrow 0$). The resulting distribution has an average charge, $\bar{J}_k = \frac{X-1}{2\omega_k}$, that represents the effects of diffusion charging acquired by particles from background radiation, and has been validated in a number of studies (e.g., Gensdarmes et al., 2001; Kim et al., 2014; Kim et al., 2016).

The size and charge are important variables in Eqs. (5), (6) and (7) and continuously vary over the whole size distribution. A singular charge distribution ($\bar{J}_k = y_k$, Eq. (6)), reduces to the symmetrical Boltzmann distribution which occurs as the ion asymmetry ratio X approaches 1. The mean charge of each aerosol size bin can then be used to approximately calculate the correction factor. For lower values of X however, the resulting charge distributions are asymmetric and not well approximated by the Boltzmann distribution due to the higher mobility of the negative ions (Clement & Harrison, 1992), making the average charge an insufficient proxy for the correction factor. To overcome this limitation, the average correction factor between particles of size i, k $\overline{W}_{k,i}$ proposed by Clement et al. (1995) and validated by Kim et al. (2016), which can consider the interaction of all charged aerosols, was employed.

$$\bar{W}_{k,i} = 1 + \frac{\sum_{j\neq 0}^{\infty} N_{k,j} N_{i,j} \left(W_{k,i}^{-1} - 1\right)}{\sum_{j}^{\infty} N_{k,j} \sum_{j}^{\infty} N_{i,j}} \quad (9)$$

If repulsive electrostatic forces are predominant among aerosols, the sign of the fractional term in the right-hand side of Eq. (9) is changed to minus and the average correction factor is less than unity (i.e. radioactive charging inhibits coagulation). Radioactive charging impacts in TOMAS-RC are introduced by multiplying the Brownian coagulation coefficient by $\bar{W}_{k,i}$ (Fig. 1).

2.2.3 Optimization of Coagulation Corrections for Broad Charge Distributions

During simulations, the width of the charge distribution for each bin, approximated by $\bar{J}_k \pm 5\sigma_k$, is proposed Kim et al., (2016) to determine the summations in Eq. (9). The larger the average charge and the deviation of the distribution for that bin, the larger the summation index $l = \bar{J}_k \pm 5\sigma_k$ of Eq. (9) becomes, which, in the case of large particles carrying significant charges (Clement et al., 1995; Clement & Harrison, 1992; Kim et al., 2013) can lead to values of *l* of the order 10^3. The computational burden in such situations quickly becomes overwhelming, as the required calculations for the correction factor scale with $k^2 l^2$ at each microphysical TOMAS-RC timestep (because the summations of Eq. (9) need to be recalculated every time to consider all interactions between all size bins *k*, as well as every possible charge value for bin *l*). In the case of radioactive particles with a diameter greater than 2 μm, the average charge attained can be, depending on the radionuclide of question, on the order of thousands, which increases the computation time by at least 10^4 when compared to smaller particles with $\bar{J}_k$ values less than 10. The computational burden is further increased by broadening of the charge distribution – which expands the summation in Eq. (9) to include substantially more terms.

To accelerate calculations while minimizing loss in accuracy, instead of iterating over all possible values of l for each size bin, iterations are done over a limited charge interval about the mean $[\bar{J}_k - 2\sigma_k, \bar{J}_k + 2\sigma_k]$, which for the normal charge distribution encompasses 95% of the possible charge values. Other values for the intervals were tested, spanning from $\bar{J}_k \pm 5\sigma_k$ to $\bar{J}_k \pm \sigma_k$ and the results showed the best agreement with the lowest associated computational cost for $[\bar{J}_k - 2\sigma_k, \bar{J}_k + 2\sigma_k]$. We additionally employ an adaptive, linearly increasing, step for the iterator j of Eq. (8), which was used when the average charge exceeded 100. This step was derived empirically based on simulation results for the cases where $\bar{J}_k$ and σ_k were highest, by determining the limiting case from all the simulation scenarios, which occurred for ^{131}I when the particle size and concentrations were maximum. We find that using a step of $\Delta n_k = \frac{|4\sigma_k|}{100} + 1$ (where Δn_k is the step size for a given particle size r_k, σ_k is the deviation of the charge distribution for size bin k) considerably accelerates the calculations at a minimal loss of computational accuracy.

Figure 2.2 shows the comparison between the approach described in Clement et al. 1995 and the aforementioned scheme, showing the average enhancement factors between particles of a given size r_k, as a function of a coagulating particle with size, r_i. For particles with r_k values of less than 0.345 μm, coagulation tends to be unaffected for smaller sizes and enhanced for larger ones, since particles of that size carry a very small negative charge of less than -1. As small charge means that their coagulation with other small particles is not inhibited, while enhancement is seen for larger sized particles carrying a large positive charge ($\bar{J}_k > 100$). For particles with r_k values of 0.801 μm ($\bar{J}_k \sim 2$), there is an initial enhancement between the negatively charged, small-sized part of the distribution, an

inhibition for mid-sized, positively charged particles, and a subsequent enhancement for the larger, strongly positive particles. Since these particles carry the same sign charge, this enhancement can only be explained by a considerably negatively charged tail of the charge distribution ($\sigma_k = 3.71$) of the particles with r_k=0.801 μm, which shows that the average charge is not a good predictor of radioactive coagulation, and the use of a distribution is necessary. For the larger particles with r_k=1.6 μm ($\bar{J}_k \sim 21.5$), there is an initial expected enhancement of coagulation between them and the negatively charged smaller particles, and a strong inhibition for the positively charged larger particles.

Using the optimizations described above, calculation of $\overline{W}_{k,i}$ in TOMAS-RC is accelerated by up to 3 orders of magnitude. When compared to using the exact summation calculations over a charging distribution that considers ±5 σ about the mean $\bar{J}_k$, there is no apparent loss in accuracy, as the enhancement factors computed for coagulation of ^{137}Cs aerosol (Fig. 2.2) are similar to the ones reported by Clement et al. (1995).

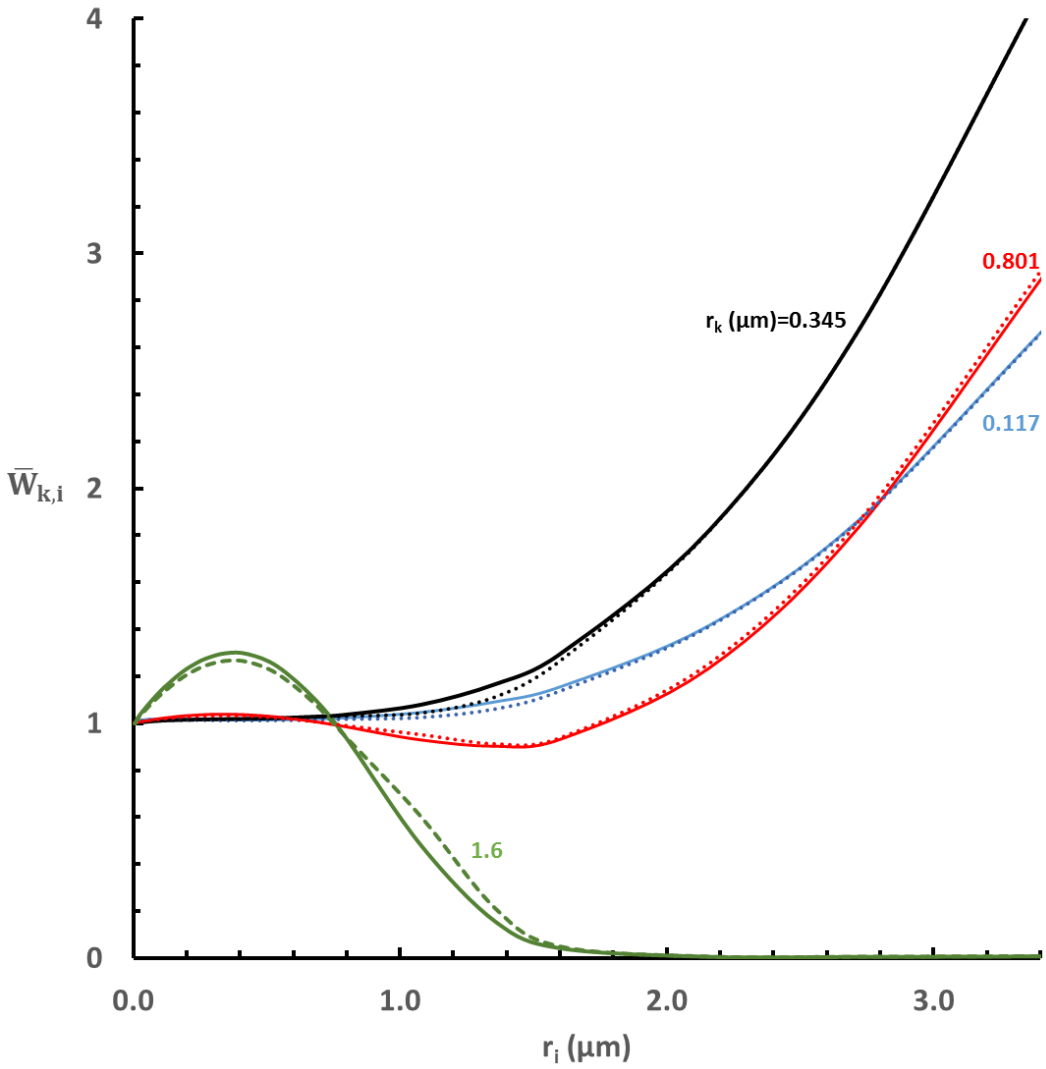

Figure 2.2 Enhancement factors ($\overline{\boldsymbol{W}}_{\boldsymbol{k,i}}$) predicted using TOMAS with the accelerated computation scheme described in section 2.3 (dashed lines) versus the full resolution computations (solid lines) between particles of size r_k and r_i. For fine particles, the enhancement factor increases dramatically with increasing particle size, while for coarser aerosol, it reaches a maximum and then decays to almost 0. The r_i values chosen were the closest that the TOMAS bins describe, to the ones used in Clement (1995).

2.2.4 Atmospheric simulation scenarios

To demonstrate the capabilities of TOMAS-RC, it is used to simulate the deposition of ^{137}Cs and ^{131}I during an idealized radionuclide release incident. Simulation results for neutral background aerosol are obtained under the same initial conditions and given for reference. The specific radionuclides are considered, as they have been released during nuclear plant accidents (Mason et al., 2011; Yoshida & Kanda, 2012; Kauppinen et al., 1986). The characteristics of the idealized simulations are provided in Table 2.1. Values for radioactivity pertinent parameters were obtained from previous studies (Clement & Harrison, 1992; Clement et al., 1995; Kim et al., 2015). The height of the top layer was set to 1 km so that it could capture a potential plume from a nuclear accident (Chesser et al., 2004).

For all simulations considered, three aerosol microphysical processes were accounted for i.e., coagulation, vertical mixing (turbulent diffusion) and dry deposition (Fig. 2.1) – as a means of carrying out a semi-Lagrangian simulation, where an airmass is tracked as it advected away from its release point, but still allowed to vertically mix. Such a simulation resolves the processes that impact the microphysical evolution of the aerosols contained within the column and also can be used to compute the depositional loss of radioactive. The simulation duration is set to 5 days, which covers most of the lifetime of tropospheric aerosol (Seinfeld & Pandis, 2006). We assume that η_0 of the radioactive aerosol is constant throughout the simulation. The effects of radioactive charging were assessed by examining the aerosol fields with and without radioactivity effects and for four different values of the ion mobility ratio (X): 0.7, 0.8, 0.9 and 1, for each radionuclide considered. In all simulations, it was assumed that each of the five vertical levels had an

initial particle population that followed a log-normal distribution with a single mode. Dry deposition was the only active mechanism of aerosol loss from the atmospheric column.

The microphysical characteristics of the radioactive aerosol emissions are highly uncertain, so we assess the importance of radioactive charging for a wide range of initial distributions, by varying the geometric mean diameter, D_g, initial concentration of particles, N_0, and the geometric standard deviation σ_g of the radioactive aerosol. The range of values used for this study is shown in Table 2.2. The results of the sensitivity analysis were evaluated using the column integrated mass ratio (CIMR) of aerosol remaining in the column:

$$CIMR = \frac{MR_t}{MNR_t} \tag{10}$$

where MR_t and MNR_t are the total amounts of mass residing in the column after time t for the radioactive and nonradioactive cases, respectively.

Table 2.1. General simulation conditions

Parameter	Iodine	Cs	Reference
Specific radioactive decay [Bq μm^{-3}]	43800	64	Clement et al., 1992, 1995
The number of ion pairs produced per decay	1945	2067	Kim et al., 2015
Minimum height [m]	200	200	TOMAS default settings
Maximum height [m]	1000	1000	
# Height levels	5	5	
Temperature [K]	293	293	Atmospheric conditions

Table 2.2 Parameter space for sensitivity analysis

Parameter	Range	Notes
Geometric mean diameter (D_g)	30 nm – 5.2 μm	Range of atmospherically relevant sizes
Initial #concentration (Particles m^{-3})	10^6-10^{13}	Range of atmospherically relevant concentrations
Standard geometric deviation (SGD)	1.5-3.0	Range of atmospherically relevant deviations
Mobility ratio (X)	0.7-1	From Mohnen, 1976 & Kim et al., 2014

2.3. Results

Deposition characteristics of radioactive aerosols in the column consisting of five vertical layers were investigated using the TOMAS model with and without the average correction factor (hereafter radioactive and nonradioactive cases, respectively). The column spanned altitudes from 0 to 1000 m with a resolution of 200 m, with each layer having the same amount of initial radionuclide mass. Coagulation characteristics of radioactive aerosols in one layer were investigated first before analyzing the vertical transport and deposition of the aerosols. Then the aerosol size distribution and total mass residing in each layer were analyzed to elucidate the effects of the radioactive charging on the deposition of radioactive aerosols. During these investigations using the TOMAS-RC model under various initial conditions, computational issues (e.g., computational instability which can suddenly increase computational costs) were not observed.

Given that multiple charging mechanisms exist and different particle sizes are involved in each one, a wide range of particle size distributions was used. Particles formed through ion-induced nucleation are a few nanometers in size (Harrison & Carslaw, 2003), while particles in volcanic ash or dust clouds that are charged through friction, reside mostly on the coarse mode with diameters greater than 10 μm (Langmann 2013). For charged radionuclides resuspended during fires, the bulk of radioactive material is contained in giant particles of diameters greater than 25 μm as shown for the case of forest fires conducted in controlled conditions in the Chernobyl exclusion zone (Yoshchenko et al, 2006). Note that this refers to radionuclides that were already deposited on the ground and not new particles formed through charging mechanisms.

2.3.1 Aerosol Size Distributions

Figure 2.3 presents the microphysical evolution, expressed as changes in the size distribution, of ^{137}Cs aerosols at 400-m altitude over time. The initial size distributions were selected so that a significant number of large particles were present, leading to an appreciable impact of radioactive charging. Shown are the changes that would occur in the presence (solid lines) and absence (dashed lines) of radioactive charging. In the presence of charging effects, ^{137}Cs aerosols coagulate more slowly than nonradioactive aerosols. This behavior can be seen in a less dramatic shift of the modal peak towards larger aerosol sizes over time when charges are present (Fig. 2.3). The slow coagulation occurs because numerous negative ions in the atmosphere diffuse more quickly toward the aerosol surfaces (i.e., $X < 1$), so most aerosol acquires a net negative charge (Fig. 2.4a). Since many particles smaller than 0.8 μm are not charged (Fig. 2.4a), their coagulation is almost unaffected between neglecting and considering charging effects, while particles between 0.8 and 5 μm exhibit the most dramatic inhibition (Fig. 2.3), since these are the particles that accumulate the largest amount of negative charges (Fig. 2.4a). Particles larger than 5 μm carry even larger amounts of negative charge, but are not present in significant concentrations (d_g = 1.5 μm) to affect the shape of the number distribution (Fig. 2.3).

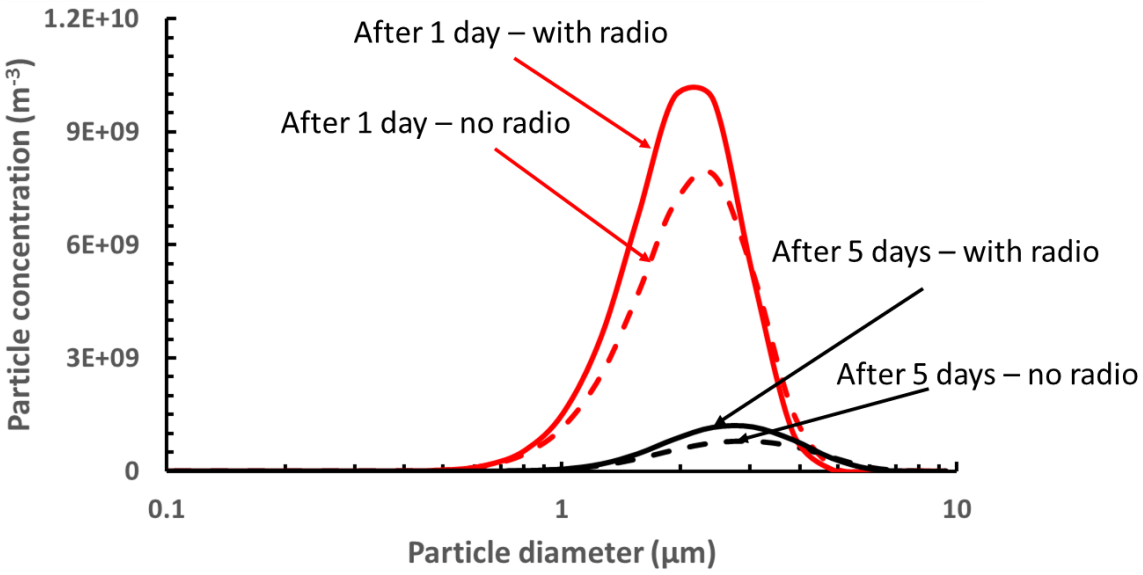

Figure 2.3 Evolution of the size distribution of 137Cs aerosols at 400 m (X=0.7, t = 5 days, dg = 1.5 µm, σg = 1.5, and Nt = 1011 m-3). Shown are results with radioactive decay (solid lines) and without radioactive decay (dashed lines).

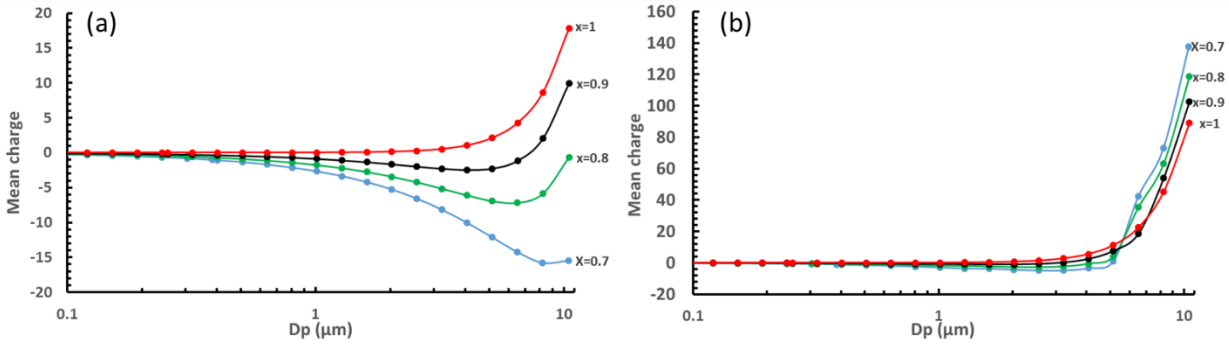

Figure 2.4 Mean charge values for particle sizes between 0.1 and 10 µm, for 137Cs (a) and 131I (b), for X values of 0.7, 0.8, 0.9 and 1.

The evolution of the size distributions of ^{131}I aerosols at 400-m altitude is presented in Fig. 2.5. Similarly to ^{137}Cs, particles below 4 µm are negatively charged, inhibiting their coagulation. Even for a low value of *X* (0.7), however, all particles above 4 µm are positively charged (Fig. 2.4b), leading to notable differences in the predicted distributions when neglecting and considering charging effects. Particles up to 1.3 µm in diameter are

slightly more negatively charged than ^{137}Cs, and the coagulation between those particles and the positively charged larger bins with a diameter of 5 μm and above is significantly enhanced leading to reduced predicted number concentrations of both the large and small particles when compared to assuming Brownian coagulation alone (Fig. 2.5). For particles close to the initial modal diameter of 1.5 μm (where most aerosol numbers lie), and up to sizes of 3 μm, coagulation of the particles is strongly inhibited due to their negative charges (Fig. 2.4b). The rationale behind looking at such a large range of particle sizes is to evaluate the effects of radioactive charging on the microphysical evolution of aerosol populations over a wide range covering from the Aitken to the coarse mode. The presence of such large particles is also expected in dust and volcanic ash clouds (Langmann 2013), as well as radiological debris created during nuclear events.

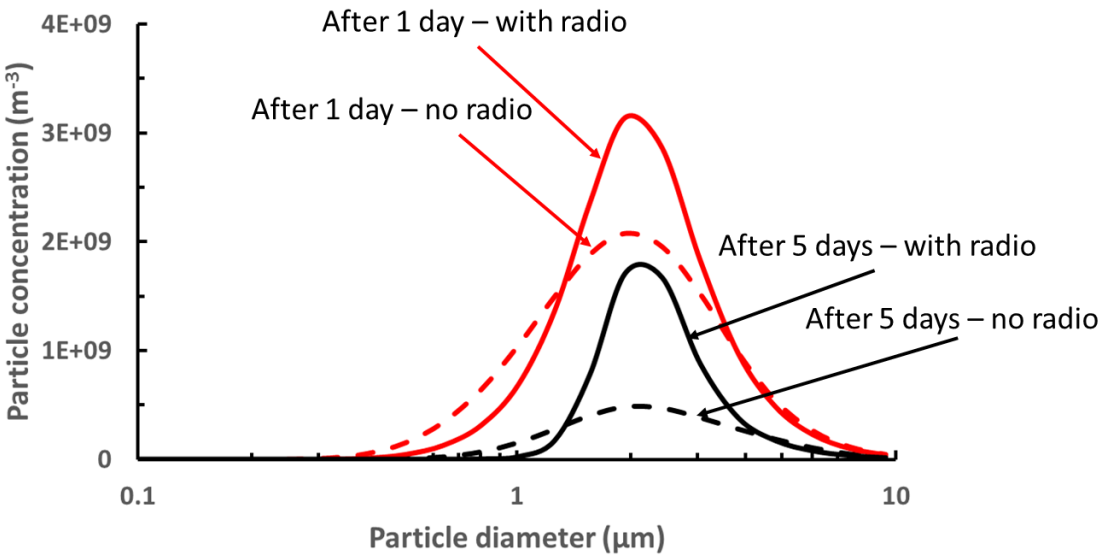

Figure 2.5 Evolution of the size distribution of 131I aerosols at 400 m (X=0.7, t = 5 days, dg =1.5 μm, σg = 2.5, and Nt = 1010 m-3). Shown are results with radioactive decay (solid lines) and without radioactive decay (dashed lines).

For the case of ^{137}Cs, the average charge is negative for all size bins when $0.7 \leq X \leq 0.8$, leading to inhibition of coagulation for all size bins. For X=0.9, the mean charge is negative for all particles below 3 μm, but become positive for larger sizes, leading to inhibition of coagulation between particles of small sizes, and enhancement between particles below and above that threshold. ^{131}I exhibits similar behavior, but because of its much higher decay rate, particles tend to accumulate much smaller negative charges and significantly larger positive ones. For $0.7 \leq X \leq 0.8$, particles up to 4 μm accumulate a small amount of negative charge, while, above that size cutoff all particles are strongly positively charged, implying accelerated coagulation rates between particles belonging to the different sides of the cutoff and inhibition for ones belonging on the same. Larger X leads to the entire size spectrum being positively charged and inhibition across all particle sizes.

2.3.2 Dry deposition fluxes of radionuclides

Figure 2.6 shows contour plots of CIMR from Eq. (10), for the ^{137}Cs aerosol simulation after 5 days of microphysical evolution, as a function of initial geometric mean diameter and initial concentration. As the geometric mean diameter and total concentration of the initial aerosol size distribution increase, so does the CIMR, indicating that fewer ^{137}Cs aerosols were deposited. This behavior means that the lifetime of the radioactive aerosol can increase and particles may deposit over a longer distance away from the source. For the more extreme cases, where the concentrations were upwards of 10^{11} m^{-3} and the geometric mean diameter was larger than 3 μm, the amount of ^{137}Cs aerosols remaining suspended in the atmosphere, and therefore available for transport, was increased by up to 260% (Fig. 2.6a), compared to the case of neutral coagulation. Increasing particle concentrations for a given initial particle diameter, meant that the number of particles that could carry a larger amount of same charges was increased, even though the average charge

is independent of the number concentration, due to the deviation of the charge distribution (Eq. (6)), leading to inhibition. At the same time, increasing the initial particle size for a constant number concentration augments the number of larger particles that are able to sustain a larger number of charges (Figs. 2.4a, b), which in turn translates to stronger impacts of charging on coagulation.

It is important to understand the change in deposition behavior of ^{137}Cs particles as the relative mobility of positive vs. negative particles (i.e., X) changes, especially if the radioactive decay has a range of negative/positive ions produced (certainly the case for diffusion charging in air, where the carrier molecules of ions may be N_2 or O_2 (Harrison & Carslaw, 2003). For situations where X is less than 0.9 (Figs. 2.6a, b), the entire particle distribution is negatively charged (Fig. 2.4a), which leads to a distribution-wide inhibition of coagulation. The inhibition is stronger for the lowest value of X=0.7, since the higher mobility of negative ions leads to particles becoming strongly negatively charged, thereby limiting their interactions. When X~1 (Fig. 2.6d), particles up to sizes of 3 μm have a mean charge of zero, while larger ones are all positively charged with an average charge increasing exponentially with size (Fig. 2.4a), meaning that as the concentration of aerosol larger than 3 μm increases, the coagulation between them is suppressed due to the accumulation of large charges of the same sign. In the case of a mobility ratio of less than 0.9 (Figs. 2.6a, b), the charge of all particles is negative, leading to strong coagulation inhibition.

An interesting behavior is observed on CIMR when X increases from 0.9 to unity (Figs. 2.6c, d); while the amount of mass deposited is increased with increasing X (Figs. 2.6a, b), the opposite trend is observed between X=0.9 and 1 (Figs. 2.6c, d), with the mass

deposited decreasing with an increase in X. The reason for this behavior is that the mean charge of each bin changes sign and from negative becomes positive, even for the smaller sized bins (Fig. 2.4a). This change increases the coagulation rates between the smaller, negatively charged particles and the larger positively charged particles, but at the same time, inhibits the coagulation between the same large particles. An explanation can be found by looking at the definition of the average charge of each bin. For all ^{137}Cs cases simulated, $\omega_k y_k < 0.22$ and therefore $\bar{J}_k = y_k + \frac{X-1}{2\omega_k}$ (Eq. (6)). When $X \leq 0.8$, the fractional term is negative and larger than y_k. However, when X=0.9 and large enough particle sizes, y_k becomes greater than the negative fractional term, leading to these particles becoming positively charged.

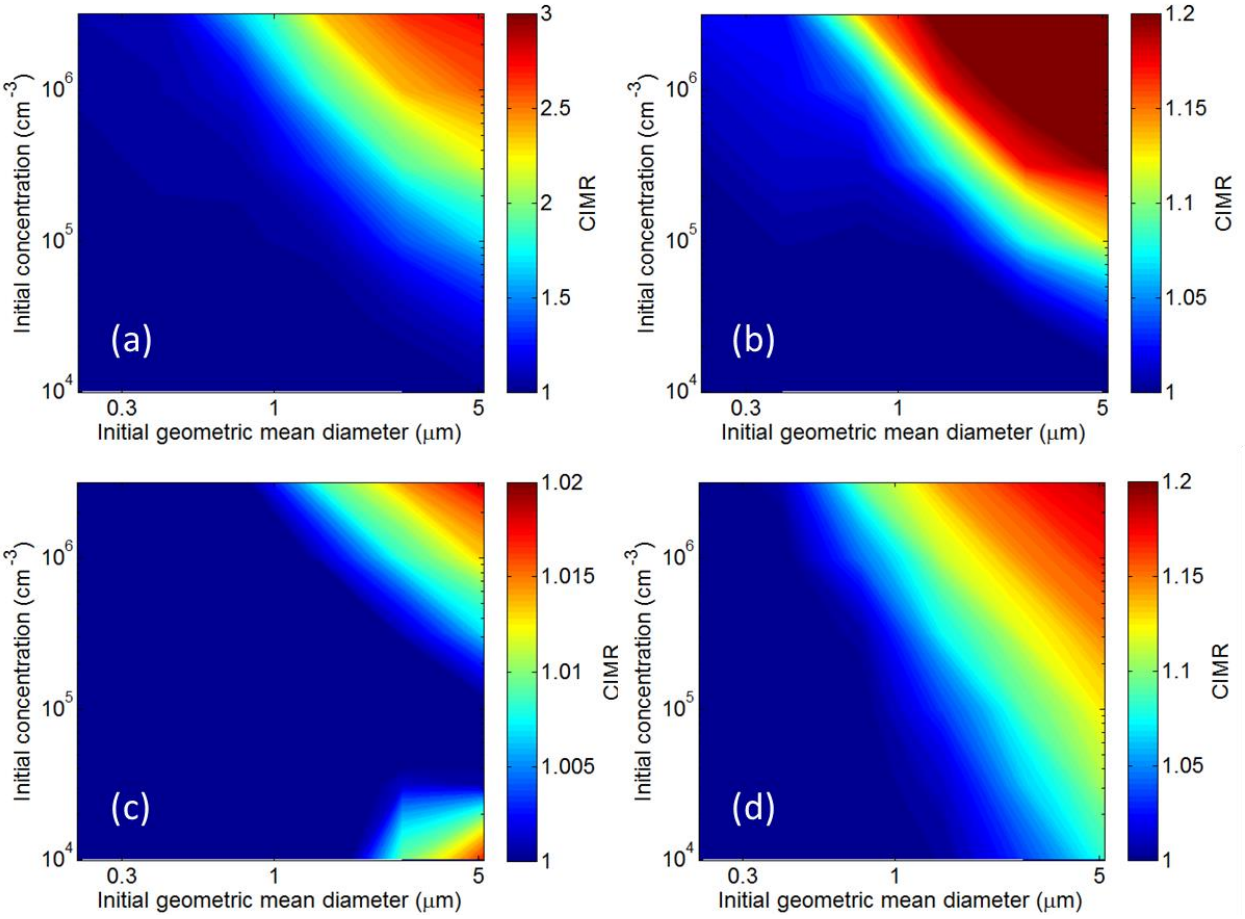

Figure 2.6 CIMR for 137Cs aerosols after 5 days for X values of (a) 0.7, (b) 0.8, (c) 0.9 and (d) 1; $\sigma_g = 2.0$.

Figure 2.7 shows CIMR for ^{131}I aerosols after 5 days under various initial aerosol size distributions. As with ^{137}Cs, less ^{131}I aerosols were deposited, as the mean diameter or total concentration increased. Because the radioactive decay rate of ^{131}I aerosols is nearly 700 times higher than that of the ^{137}Cs aerosols (Table 2.1), the impact of charging is much more pronounced and can lead to up to a factor of 30 more mass remaining after 5 days of atmospheric processing (Fig. 2.7d). Similar behavior to ^{137}Cs was observed, with the average charge of some bins changing sign depending on the mobility ratio (Fig. 2.4b). However, in stark contrast with the ^{137}Cs simulations for the same conditions, all particle

sizes above 5 μm are strongly positively charged regardless of the value of the mobility ratio, with the charge of the largest bins being in excess of a 100. The largest impact of radioactive charging for ^{131}I can be seen in the case of X=0.9 and 1. Looking at the average charge of each bin for these cases, reveals that the entire distribution is positively charged (Fig. 2.4b), which in turn leads to very strong inhibition between all bins, and a resulting 30-fold increase in mass remaining after 5 days, if the emitted particles contain large amounts of radionuclides (Figs. 2.7c, d). The effect is slightly more pronounced for the case of a mobility ratio of 0.9, because the maximum charge attained by the largest particles can be higher than for the case of a mobility ratio of unity (Fig. 2.4b). For X values of 0.7 and 0.8, particles up to 5 μm carry a negative charge that enhances their coagulation with larger positively charged particles, but the significant positive charges attained by the larger particles (Fig. 2.4b) still leads to overall inhibition, and subsequently to high CIMRs values (Figs. 2.7a, b), albeit smaller than the ones predicted when $X\geq0.8$, due to the aforementioned enhancement.

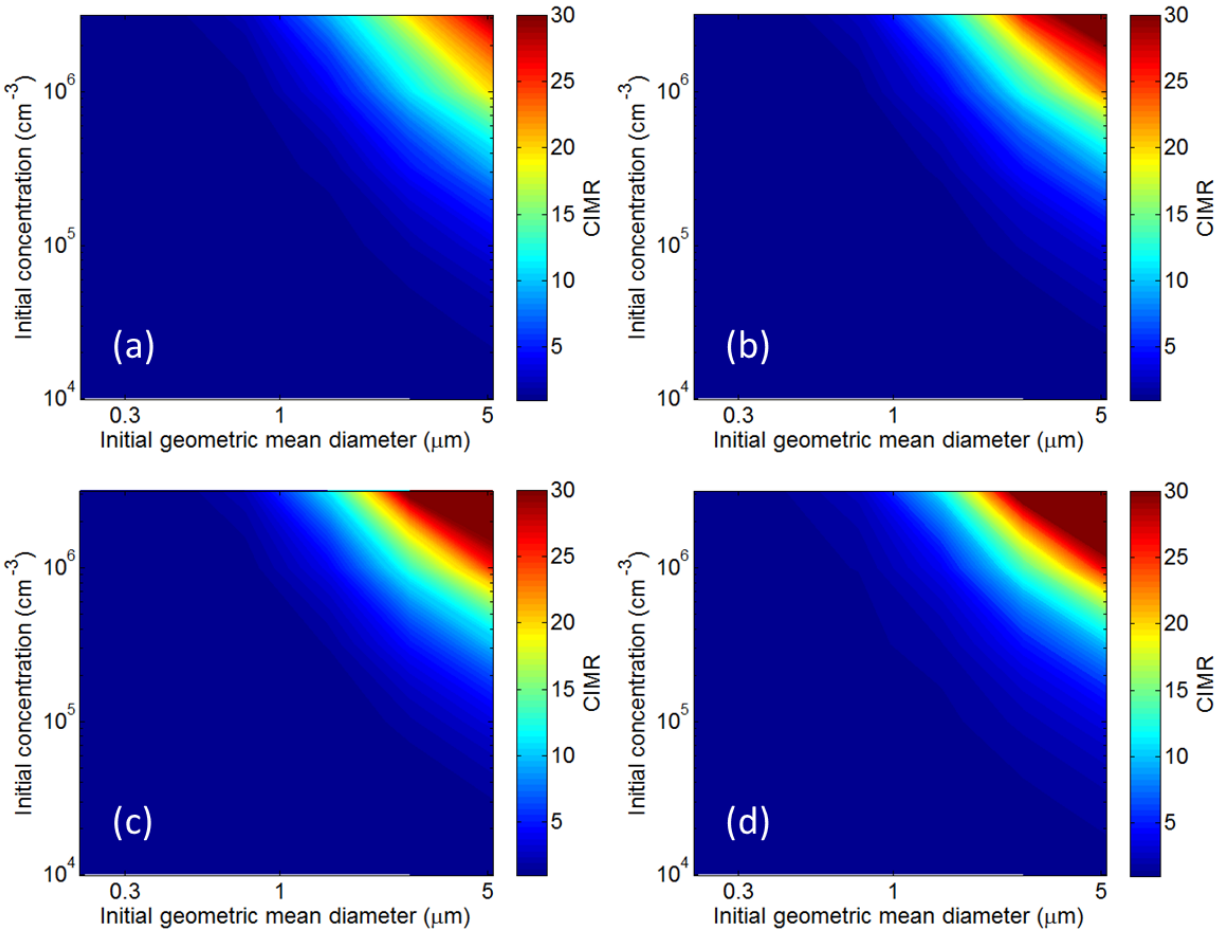

Figure 2.7 CIMR for 131I particles after 5 days for X values of (a) 0.7, (b) 0.8, (c) 0.9 and (d) 1; σ_g = 2.0.

To further determine the impact of possible diffusion charging effects on non-decaying particles, simulations were carried out where the radioactive decay rate of the aerosol population was set to a value of 0. In this case, η_κ=0→ $\omega_k y_k = 0$ and therefore $\bar{J}_k = \frac{X-1}{2\omega_k}$ (Eq. (6)). Diffusion charging can have a significant impact on very coarse aerosol (Gunn, 1954) such as dust and volcanic ash, regardless of its composition. Following the same analysis as with the radioactive particles, the same scenarios were studied and results analyzed using the CIMR. While the impact of diffusion charging on small particles (Fig.

2.8) is negligible, for very large aerosol and high enough concentrations the impact can be significant, especially in environments where many ion pairs are produced, and where the mobility of negative ions is greater than that of the positive ones (X<1). For such cases, all particles gather large negative charges and enhancement factors of less than unity, which inhibits their coagulation and lead to increased aerosol lifetimes.

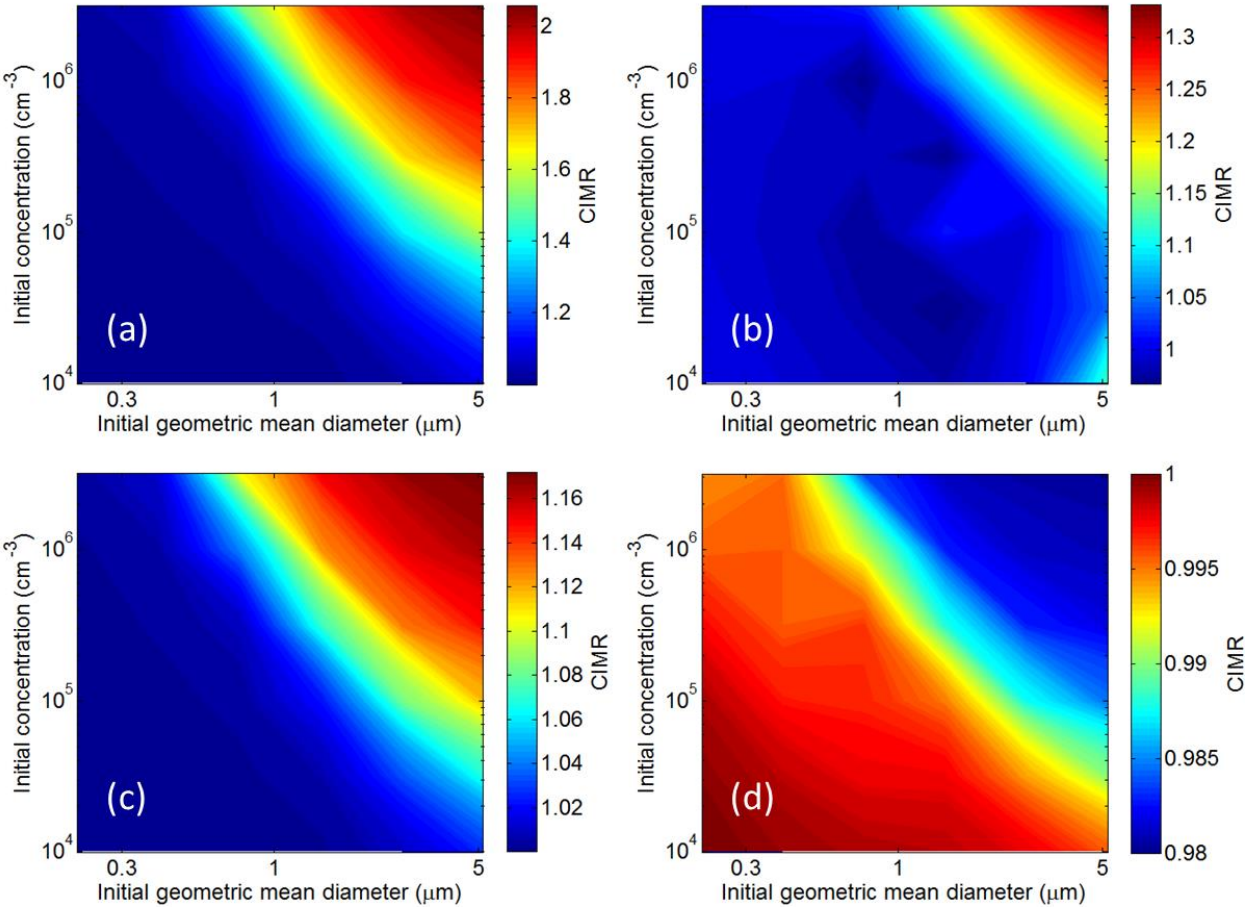

Figure 2.8 CIMR for particles under diffusion charging conditions, after 5 days for X values of (a) 0.7, (b) 0.8, (c) 0.9 and (d) 1; σ_g = 2.0.

For all cases described above, the geometric standard deviation of the initial aerosol size distribution, σ_g, was also found to affect CIMR. Larger values of σ_g simultaneously increase the number of small and large particles, which in effect augments both the

enhancement and inhibition for all cases. Inhibition tends to be favored, since wider distributions carry a higher number of large particles, which subsequently become a larger portion of the total aerosol mass, given that the mass scales cubically with size. These large particles tend to carry the largest amount of charges (Figs. 2.4a, b) and are affected the most by radioactive charging. Therefore, increasing their mass fraction for any value of the mobility ratio will lead to overall inhibition, and also extend the impact of radioactivity to lower initial particle concentrations and diameters, since even in this case an abundance of large particles will be present.

2.4. Conclusions

This chapter describes the development of the TOMAS-RC model, an expanded version of the TOMAS microphysics model to explicitly treat the effects of radioactive charging on the microphysical evolution during the transport and deposition of radioactive particles away from a radiation source. Electrostatic charges induced by radioactive decay, through the mechanisms of self- and diffusion charging, can magnify or reduce the coagulation rates of radioactive particles by producing electrostatic attractive or repulsive forces. Effects are introduced as a multiplication factor applied to the Brownian coagulation kernel of TOMAS; explicit treatment of the discretized nature of the size distribution, the charge distribution within each size bin and accelerations of the calculation procedure are discussed in detail.

The TOMAS-RC model was applied to study the dispersion and microphysical evolution of radioactive particles within a vertically-dispersing atmosphere, and simulations were carried out for aerosols carrying numerous ^{131}I and ^{137}Cs atoms for a wide range of initial aerosol conditions and ion mobilities. Radioactive charging for both

radionuclides was found to often have an important impact on the evolution of the particle size distributions and subsequent dry deposition of radioactive aerosol. The effects increased as the initial size or concentrations of radioactive particles increased, due to different ion concentrations determined by equations (7) and (8). The ratio of mobilities of the positive ions to the negative ions, *X*, was found to also have a very strong effect on the evolution of the particle size distribution and deposited particles, especially for the case of ^{137}Cs particles, where depending on the value of *X*, some bins of the aerosol distribution can switch sign and behavior altogether (charging enhancing vs. inhibiting coagulation). It should be noted that, the charge signs of ^{137}Cs and ^{131}I aerosols can be opposite because the signs depend on their radioactivity levels and ion concentrations which determine their dominating charging mechanisms, as shown for the case of particles larger than 5 μm for all *X* values.

Through a series of highly idealized simulations, it is shown that the charging of radioactive aerosols can have an appreciable effect on how particles are deposited, with important implications for predicting dispersal patterns after nuclear accidents. However, it has been assumed that only one type of radionuclide is present. More realistic aerosol may contain external or internal mixtures of radionuclides, with very different microphysical evolution from the ones describe here. For example, if both ^{137}Cs and ^{131}I are present in the same column as externally-mixed aerosol, the coagulation would be highly facilitated and thus the deposition rates of radioactive aerosols should be enhanced. Multigenerational products from the decay of radionuclides during atmospheric transport can create conditions of variable *X* (dependent on particle size and composition) that can lead to very different depositional patterns as well. Coagulation of externally mixed bins,

or condensation/evaporation of semi-volatile radionuclides (e.g. ^{131}I, ^{132}I) can create particles of varying compositions, which in turn translates to different rates of radioactive decay and charging mechanisms. Further decay products of radionuclides (e.g. ^{132}Te to ^{132}I) can shift the balance between diffusion and self-charging (Kim et al., 2017), and that behavior can induce significant uncertainties in modeling.

Since dry deposition is considered, the potential role of radioactive charging on wet scavenging is not considered. However, the potential acceleration of the coagulation between fine particles from charging could make these particles larger and therefore more effective cloud condensation nuclei (CCN), increasing the efficiency by which they are removed from the atmosphere through wet deposition and warm rain process modulation. Coagulation of radionuclides with larger, charged dust particles which are very efficient ice nuclei (IN) may also affect deposition patterns by promoting cold rain processes. Future and ongoing modeling activities should focus on a full account of all such effects to fully elucidate the impact that radioactive charging effects can have on the transport of radioactivity across the globe.

CHAPTER 3

THE IMPACT OF PHILLIPS 66 FACILITIES ON AIR QUALITY IN THE TEXAS-LOUISIANA AREA

This chapter summarizes the work conducted to better understand and quantify the Impacts of Energy Sector Emissions on Air Quality, with a focus on sensitivity modeling for Phillips 66 facilities, for the June 2012 episode over Texas and South Louisiana, expansion plans for the Baytown and Sweeny facilities in 2017. An array of different scenarios has been simulated, in order to gauge the overall air quality impact of the Phillips 66 facilities within the domain in 2012. For 2017 the same scenarios were simulated, using the 2017 National Emissions Inventory (NEI), complemented with the expansion plan data provided by Phillips 66. Separate sensitivity simulations were carried out to quantify the impact of expansion emissions on ozone and PM2.5. For both years, the maximum contribution out of all Phillips 66 and Chevron Phillips Chemical Company facilities within the modelling domain is 1 μg m-3 to the hourly average PM2.5, 70% of which comes from primary particulate emissions and SO2 conversion, and 3 ppb to the maximum 8-hour average O3 in the cell where they are located. The impact of the Sweeny and Baytown expansions in the emitting gridcell is found to be 0.6 ppb and 0.1 μg m-3 for the maximum 8-hour ozone and mean PM2.5 concentrations respectively, and less than 0.1 ppb/0.01 μg m-3 downwind. A notable difference between 2012 and 2017, is that ozone formation shifts from a VOC limited regime to a NOx limited one, suggestive of diminishing returns for NOx reductions. Therefore, VOC controls in the future could prove more effective in reducing the impact of industrial activities on ozone concentrations.

3.1 Texas-Louisiana-Oklahoma air quality simulations description

The linkage between emissions from energy sector operations, and other sources, was studied using the CMAQ-WRF-SMOKE modeling system (Byun & Schere, 2006). Meteorological simulations for the 2012 episode were conducted using the Weather Research and Forecasting model version 3.6.1 (WRFv3.6.1) (Shamarock et al. 2008) for four domains, nested within each other:

1. A coarse, 36km resolution domain covering the entire continental US
2. A 12km resolution grid over parts of Texas and Louisiana
3. Two separate 4km resolution grids covering Houston and Tulsa respectively.

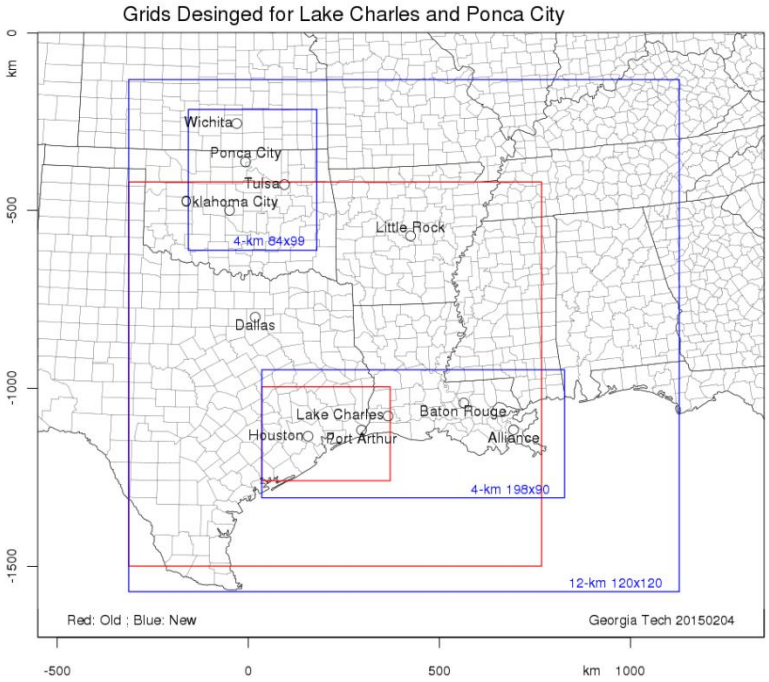

Figure 3.1 Nested grids down to 4-km resolution, with lower blue 4-km grid covering Houston, Lake Charles and Alliance areas

Meteorological inputs consisted of North American Regional Reanalysis (NARR) data, along with Automatic Data Processing (ADP) surface and upper observational data. Simulated meteorology was compared against observations to evaluate its accuracy.

The Sparse Matrix Operator Kernel Emissions (SMOKE) modeling framework was used in order to prepare model-ready emissions for the 2012 and 2017 episodes. The current version of the SMOKE platform includes 20 sectors for emissions processing, described below (adapted from ftp://ftp.epa.gov/EmisInventory/2011v6/v2platform):

1. **AFDUST**: Particulate emissions from fugitive dust sources
2. **AG**: Agricultural ammonia emissions
3. **AGFIRE**: Agricultural burning emissions
4. **BEIS**: Biogenic emissions generated using the BEIS model, version 3.6.1.
5. **C1C2RAIL**: Emissions from C1 and C2 commercial marine sources, including ports and navigable waterways. Railway emissions are also part of this sector
6. **C3MARINE**: Ocean going class 3 marine port and underway emissions within, or close to, the US mainland
7. **NONPT**: Area source emissions not included in other sectors
8. **NONROAD**: Off highway mobile source emissions
9. **NP_OILGAS**: Area source oil and gas emissions
10. **ONROAD**: On highway mobile source emissions, excluding California. This sector is processed using SMOKE-MOVES
11. **ONROAD_CA_ADJ**: On highway mobile source emissions, California only
12. **OTHAFDUST**: Particulate emissions from fugitive dust sources in Canada

13. **OTHAR**: Area source emissions from Canada and Mexico
14. **OTHON**: Mobile source emissions from Canada and Mexico
15. **OTHPT**: Point source emissions from Canada, Mexico, and offshore areas
16. **PTEGU**: Electric generating unit emissions. This sector incorporates CEM (Continuous Emissions Monitoring) hourly emissions for a majority of sources
17. **PTNONIPM**: Point source emissions from industrial activities – the Phillips 66 facilities are included in this sector
18. **PTFIRE**: Point source emissions from year specific controlled burning and wild fires
19. **PT_OILGAS**: Point source oil and gas emissions
20. **RWC**: Area source residential wood combustion emissions
21. **EXPANSION**: New sector created for 2017 using the Sweeny/Baytown emissions

Emissions used for all the 2012 & 2017 episode scenarios – expansion emissions are listed on Table 3.1.

Table 3.1 Total emissions for each expansion unit on a yearly basis

Project	VOC (TPY)	NOx (TPY)	SO2 (TPY)	PM (TPY)	PM10 (TPY)	PM2.5 (TPY)	CO (TPY)
P66 Fractionation Plant	23.91	24.68	28.77	5.94	5.94	5.68	33.64
P66 Tier 3 Gasoline	26.30	8.24	3.19	1.74	1.74	1.74	8.98
P66 Butane/Butylene Storage	2.73	-	-	-	-	-	-
P66 Export Propane	11.82	0.51	5.94	0.02	0.02	0.02	3.65
CPChem Baytown Ethylene Plant Expansion (Ethane Cracker)	103.88	165.60	16.56	56.87	56.87	52.35	587.73
CPChem Sweeny Polyethylene Units	92.62	21.43	2.44	14.39	14.28	4.72	99.69
CPChem Sweeny Ethylene Expansion (10th furnace)	6.65	17.10	8.04	8.49	8.49	8.49	37.60
P66 + CPChem Totals	**267.91**	**237.56**	**64.94**	**87.45**	**87.34**	**73**	**771.29**

We employed CMAQ version 5.0.2 (CMAQv5.0.2) with Direct Decoupled Method capability (Cohan et al. 2005) for our simulations. CMAQ runs were conducted for the same grids used for WRF. A comprehensive list of the scenarios simulated is found on Table 3.2.

Table 3.2 Simulated scenarios for the episodes of interest

2012 simulations				
Scenario name	**Resolution**	**Year**	**Brief description**	**Status**
CONUS 36	36	2012	Continental US domain, used to provide boundary and initial conditions	Completed
SE US 12	12	2012	SE US domain, used to provide boundary and initial conditions	Completed
SE US P66 facilities	12	2012	Sensitivity of ozone and PM to P66 facilities at the SE	Completed
SE US onroad	12	2012	Sensitivity of ozone and PM to onroad sources over the SE	Completed
SE US refineries	12	2012	Sensitivity of ozone and PM to all refineries over the SE	Completed
Houston4	4	2012	Baseline CMAQ simulation for the Houston-Louisiana domain	Completed
Houston P66 facilities	4	2012	Sensitivity of ozone and PM to P66 facilities at Houston and Louisiana	Completed
Houston refineries	4	2012	Sensitivity of ozone and PM to onroad sources at Houston and Louisiana	Completed
Houston onroad	4	2012	Sensitivity of ozone and PM to all refineries at Houston and Louisiana	Completed
Houston all anthropogenic	4	2012	Sensitivity of ozone and PM to all anthropogenic sources at Houston and Louisiana	Completed
Houston all industrial sources	4	2012	Sensitivity of ozone and PM to all industrial sources at Houston and Louisiana	Completed
2017 simulations				
Scenario name	**Resolution**	**Year**	**Brief description**	**Status**
2017 CONUS 36	36	2017	Continental US domain, used to provide boundary and initial conditions	Completed
2017 SE US 12	12	2017	SE US domain, used to provide boundary and initial conditions	Completed
2017 Houston4	4	2017	Baseline CMAQ simulation for the Houston-Louisiana domain	Completed
2017 Houston P66 expansion	4	2017	Sensitivity of ozone and PM to CPC expansions at Houston and Louisiana	Completed
2017 Houston P66 facilities	4	2017	Sensitivity of ozone and PM to P66 facilities at Houston and Louisiana	Completed
2017 Houston refineries	4	2017	Sensitivity of ozone and PM to onroad sources at Houston and Louisiana	Completed
2017 Houston onroad	4	2017	Sensitivity of ozone and PM to all refineries at Houston and Louisiana	Completed
2017 Houston all anthropogenic	4	2017	Sensitivity of ozone and PM to all anthropogenic sources at Houston and Louisiana	Completed
2017 Houston all industrial sources	4	2017	Sensitivity of ozone and PM to all industrial sources at Houston and Louisiana	Completed

3.2. Results

3.2.1. Meteorology

Meteorology for all domains was evaluated against observations, and evaluation results for the Houston domain are shown in Figure 2. With the exception of nighttime windspeed (Figure 3.2c) - which is a known WRF issue, most likely due to an inherently biased planetary boundary layer (PBL) suppression during the night (Hu et al. 2013) – the temperature, relative humidity and wind direction (Figures 3.2a, b, d) are well-predicted, given that the WRF simulations are driven with reanalysis fields and observations. The

statistical analysis conducted (Table 3.3) indicates that the simulated meteorology is accurate and compares very favorably with the observations for all the study domains.

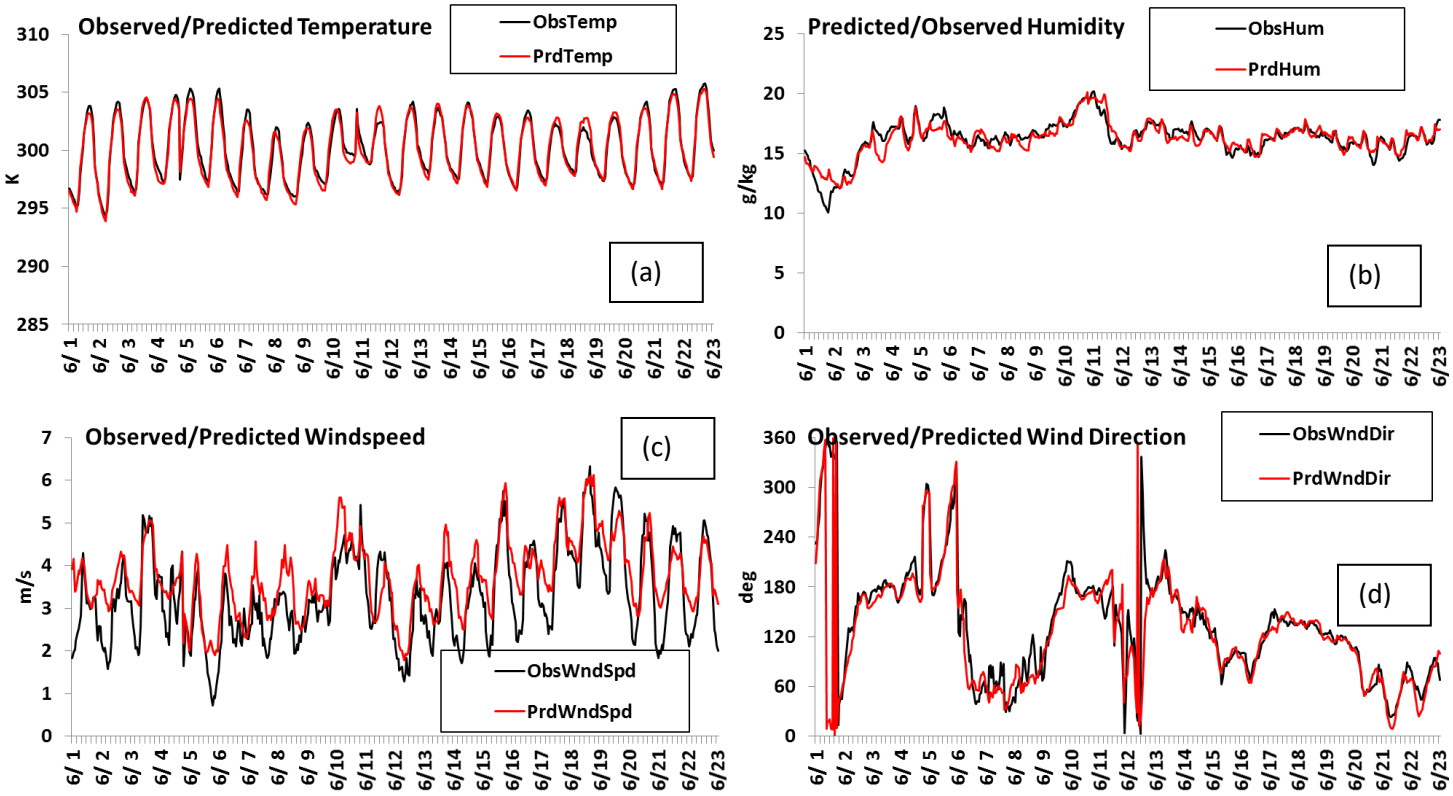

Figure 3.2 Modelled and observed temperature (a), humidity (b), windspeed (c) and wind direction (d) for the Houston domain

Table 3.3 Meteorology criteria for an accurate meteorological simulation

	Wind speed bias	**Wind speed RMSE**	**Wind direction bias**	**Wind direction Gross error**
Good simulation criteria	±0.5	2	±10	30
This simulation	0.44	2.01	-0.95	31.6
	Air temperature bias	**Air temperature RMSE**	**Humidity bias**	**Humidity Gross error**
Good simulation criteria	±0.5	2	±1	2
This simulation	-0.14	2.19	-0.07	1.24

3.2.2. 2012 CMAQ air quality simulations

This section covers the air quality modeling results for the June 1st to 30th 2012 episode. Fields for the maximum 8-hour ozone and mean PM2.5 are shown in Figures 3.3 & 3.4.

Overall, the highest concentrations of ozone are observed over industrial and urban areas in the Northeast and the Gulf. CMAQ does not allow for deposition of ozone over bodies of water leading to its accumulation and high concentrations at coastal areas. PM levels are elevated in urban areas, but also at the forests of Alabama and Mississippi, attributed to the increased emissions of biogenic precursors leading to SOA production (Xu

et al. 2016, Carlton et al. 2013 Budisulistiorini et al. 2015 & 2017, Paulot et al. 2009), which contributes to the higher PM concentrations.

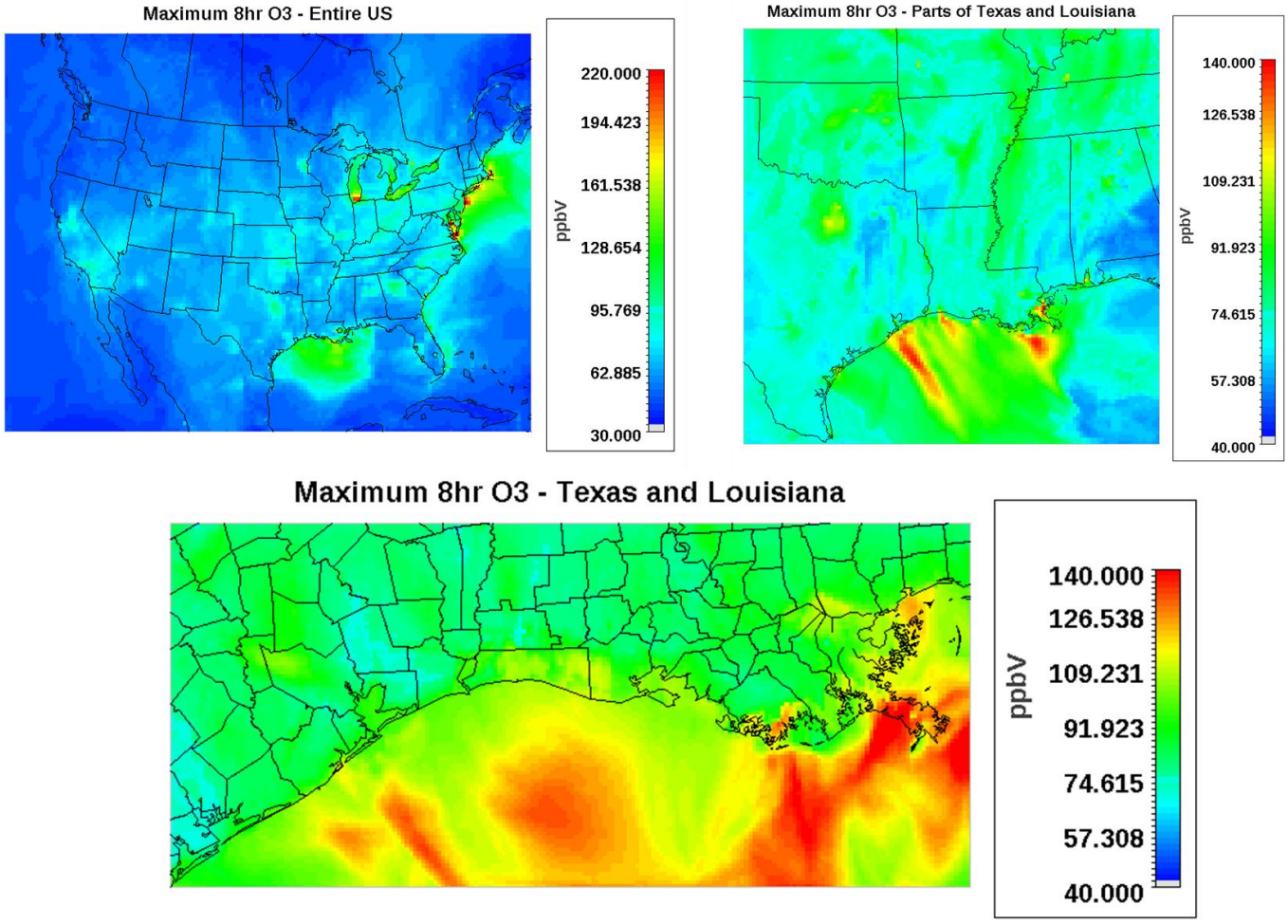

Figure 3.3 Maximum 8-hour ozone fields for every modeling domain for the episode month (2012). The value at each grid cell corresponds to the maximum 8-hour average observed over the entire episode.

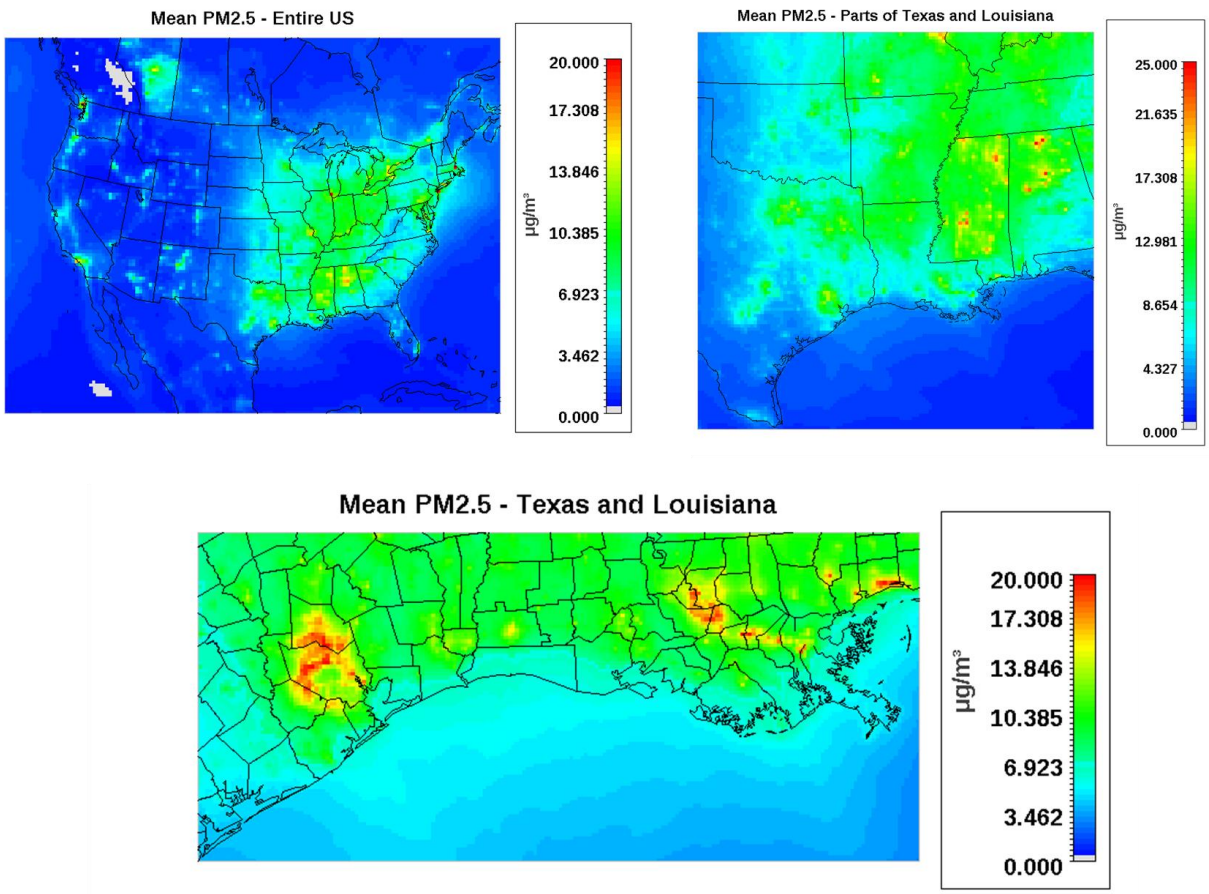

Figure 3.4 2012 episode mean PM2.5 fields for every modeling domain. The value at each grid cell corresponds to the episode mean value.

3.2.3. Sensitivity simulations

Sensitivity analyses were conducted using the Direct Decoupled Method (DDM) in CMAQv5.0.2 for the list of scenarios described on Table 3.1. Ozone was most sensitive to NO_x emissions from onroad sources and VOC emissions from industrial activities.

Of all the Phillips 66 and Chevron Phillips Chemical Company facilities in the modeling domain, NO_x emissions from the Chevron Phillips Chemical Company Cedar-Bayou plant had the strongest impact on Houston's ozone of about 6 ppb in the emitting gridcell, when in comparison onroad sources and the entirety of industrial emissions contribute upwards of 20 ppb and 14 ppb in the same gridcell respectively. VOCs emitted from the Phillips 66 Lake Charles facility had the strongest impact to the maximum 8-hour ozone in the vicinity, adding 1 ppb to the maximum 8-hour average in the facility's gridcell which is about 25% of the contribution of all refineries in the vicinity. Over the entire domain, ozone was most sensitive to NO_x, indicating a VOC-high regime. With regards to $PM_{2.5}$, both Lake Charles and the Chevron Phillips Chemical Company Cedar-Bayou plant add 1.5 $\mu g\ m^{-3}$ to the mean concentration in the cell they are located in. Specifically, the Cedar-Bayou plant is a significant contributor to the $PM_{2.5}$ load in the gridcell, accounting for 53% of the total anthropogenic contribution to $PM_{2.5}$ for the episode, with the impact rapidly dropping to about 10% 40 km far from the source.

The sensitivity patterns, which radiate outwards from the source, are due to meteorology and subsequent long-range transport of NO_x & VOCs, which affect the maximum 8-hour ozone at locations further away from the source. The greater the distance from the NO_x & VOC emission, the later the ozone concentration responds to perturbations.

In particular, the characteristic pattern from the Lake Charles facility which extends towards the Gulf (Figures 3.5, 3.6), is the model's response to the prevailing winds

during different days. While winds were mostly blowing North until the 20th of June, for the later part of the episode (20th to 30th of June) they were blowing to the South which transported NO_x & VOCs towards the sea, leading to the observed criss-cross sensitivity pattern. The maximum 8-hour ozone over the Gulf is observed during that period.

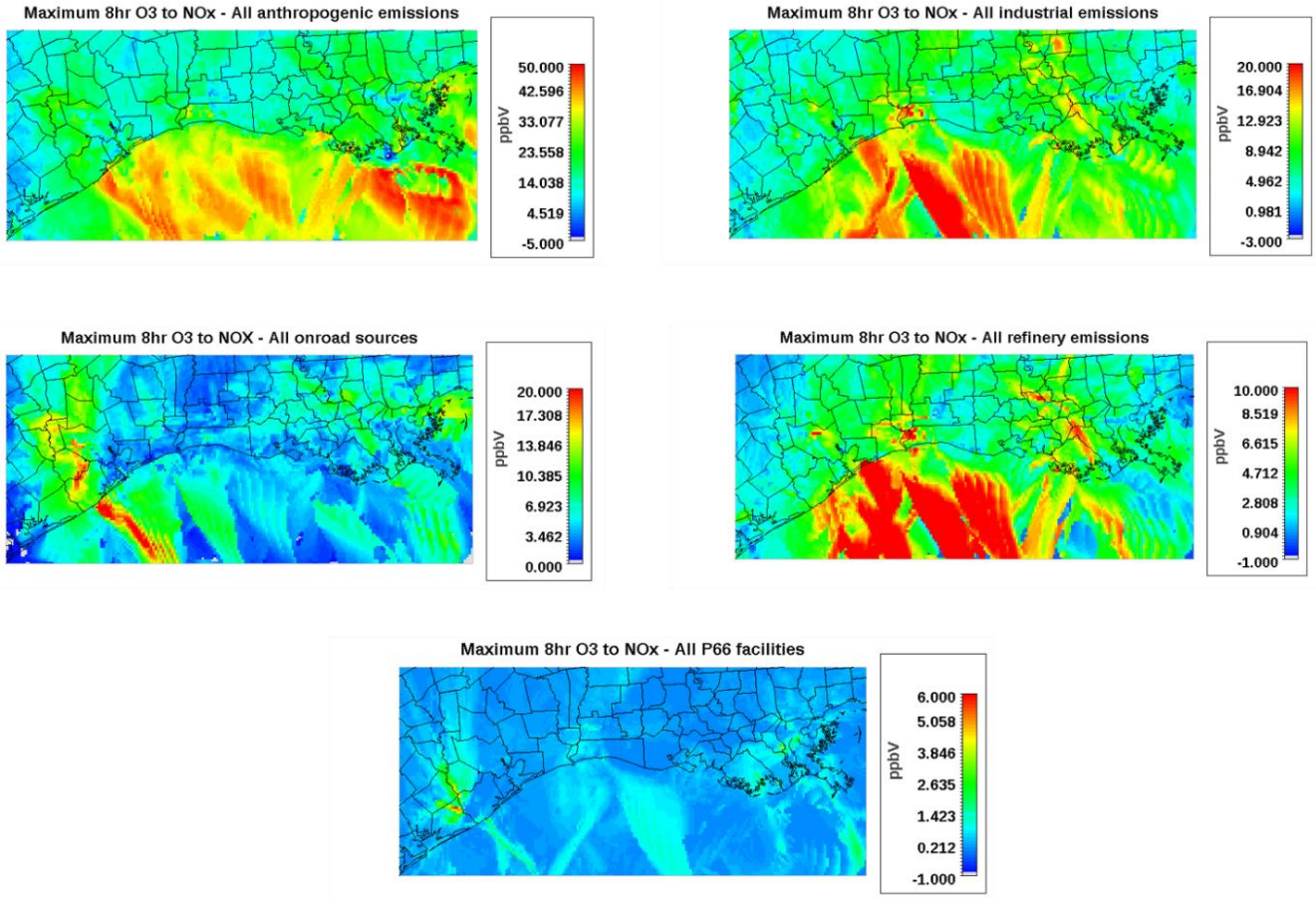

Figure 3.5 2012 episode maximum 8-hour ozone sensitivity to NO_x to emissions from all anthropogenic activities, industrial operations, onroad sources, refining and all Phillips 66 facilities. The maximum 8-hour ozone sensitivity, corresponds to the sensitivity of ozone to NO_x at the time the maximum 8-hour ozone is observed, which, is different for each cell

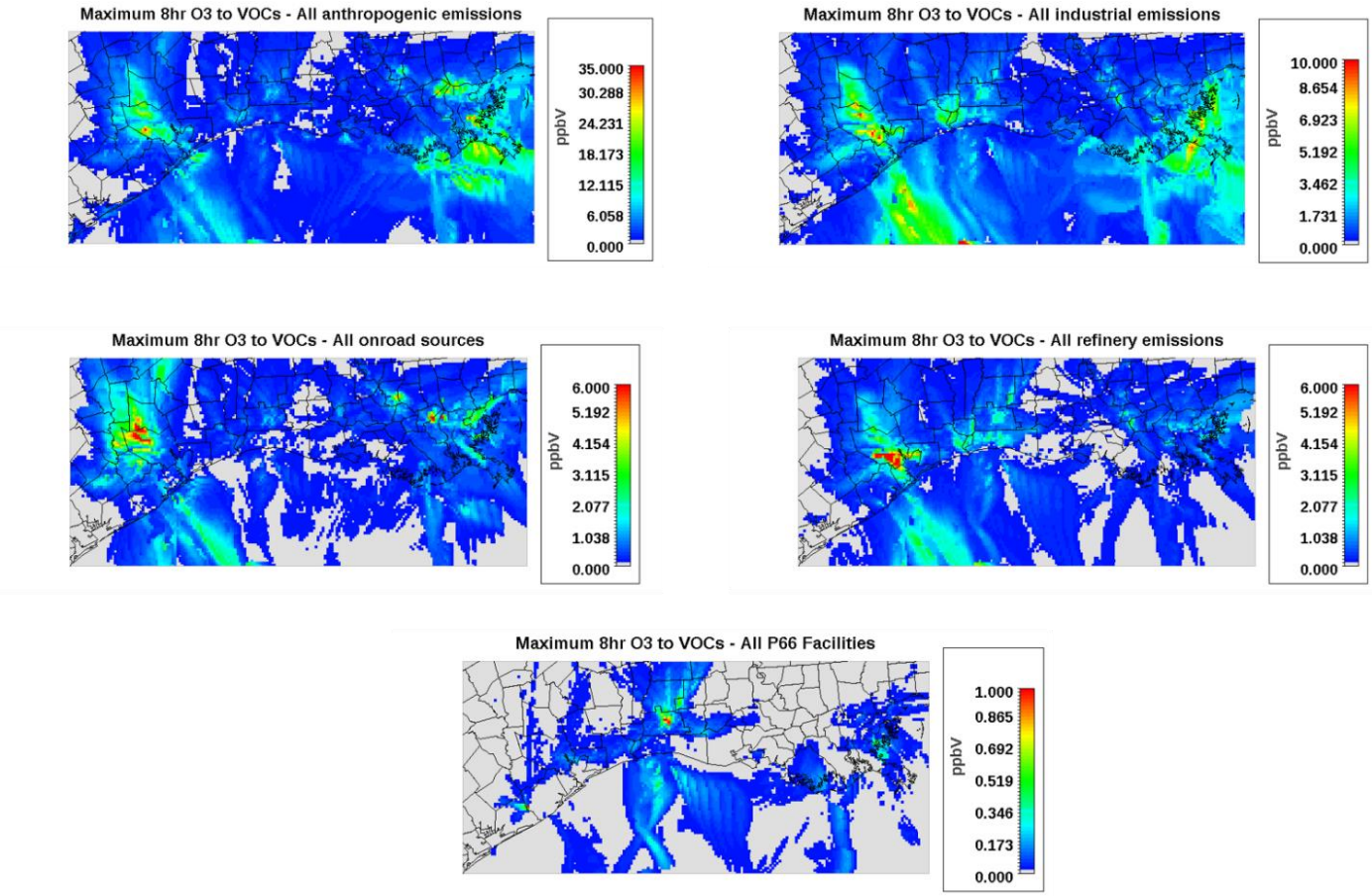

Figure 3.6 2012 episode maximum 8-hour ozone sensitivity to VOCs to emissions from all anthropogenic activities, industrial operations, onroad sources, refining and all Phillips 66 facilities. The maximum 8-hour ozone sensitivity, corresponds to the sensitivity of ozone to VOCs at the time the maximum 8-hour ozone is observed, which, is different for each cell

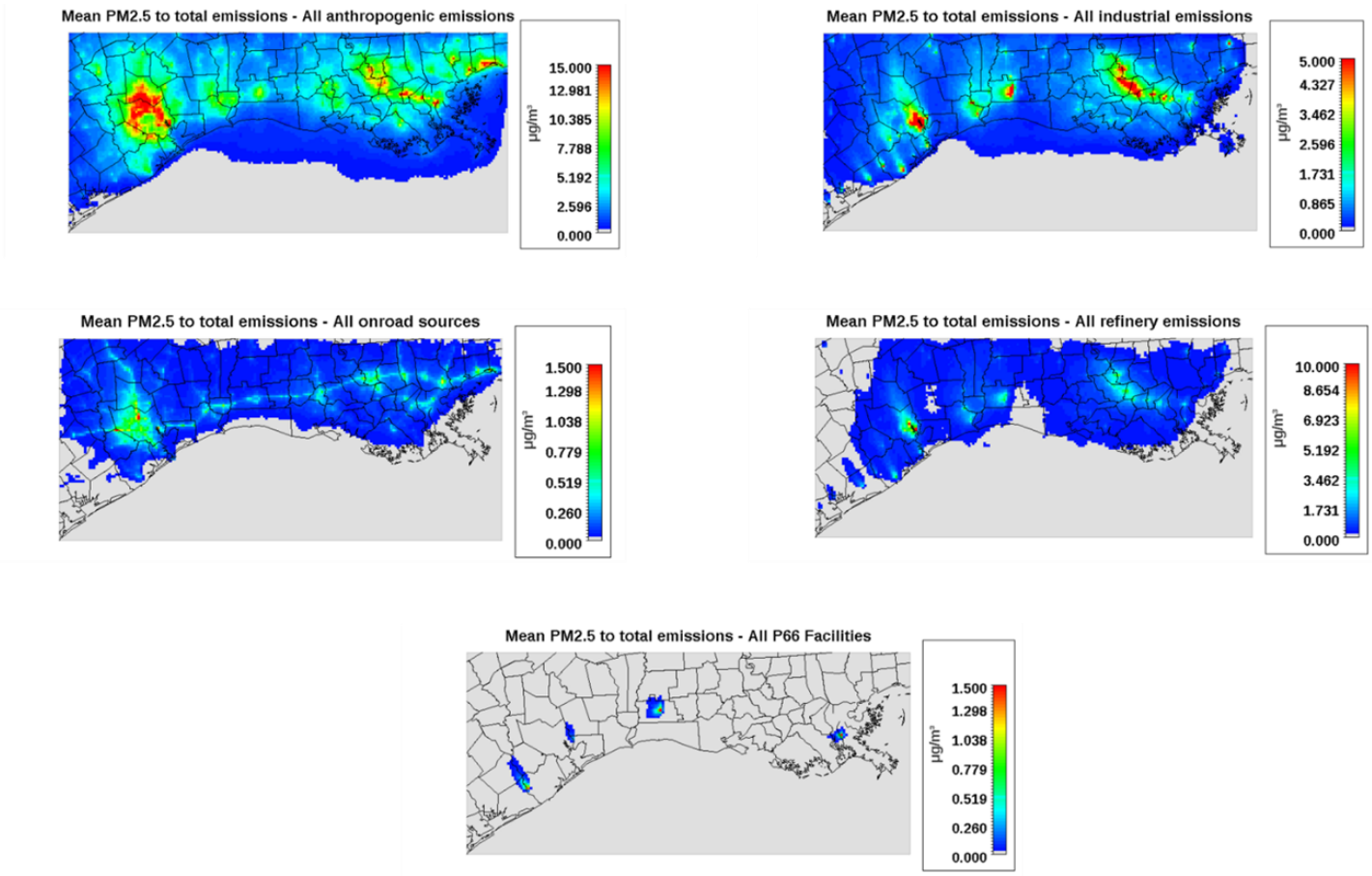

Figure 3.7 Mean PM2.5 sensitivities to total emissions from all anthropogenic activities, industrial operations, onroad sources, refining and all Phillips 66 facilities

3.2.4. CMAQ evaluation

We compared our simulations against observations of ozone and $PM_{2.5}$ for the episode period using data from 366 different AQS sites across the US for all the domains; the evaluation results are shown on Table 3.4. Simulations show adequate agreement for hourly ozone concentrations, although negatively biased by about 30% - similarly, the maximum 8-hour ozone concentrations for the episode are also biased by the same factor. Particulate matter is captured well by the model, with a positive bias of 30%, but with good agreement for the other metrics.

Table 3.4 Statistical evaluation for ozone and PM. The cutoff signifies that all values below that threshold are ignored. Metrics shown are: mean bias error (mbe), root mean square error (rmse), mean bias (mb), mean error (me), normalized mean bias (nmb), normalized mean error (nme), as well as the linear regression parameters (a is the intercept and b is the slope) for the least square regression between measurements (independent variable) and simulations (dependent variable). Criteria taken from Simon et al. 2012

species	cutoff	unit	mbe	rmse	mb	me	nmb	nme	r2	a	b
8hrO3	nocut	ppmv	0.0087	0.0160	0.0087	0.0131	-28.10	42.29	0.415	0.021	0.609
M8hO3 criteria	-	-	-	10.3	5	8.1	6.94	11.55	0.29	-	-
PM2.5	0.000	ug/m3	3.4762	6.9885	3.4762	5.1990	33.07	49.46	0.471	2.185	1.123
PM2.5 criteria	-	-	-	-	-	-	30	50	0.4	-	-

3.2.5. 2017 modeling and sensitivity simulations

To assess the impact of the expansion plans on air quality, CMAQ sensitivity simulations have been conducted for the year 2017 using the 2017 NEI inventory, incorporating the emissions provided by Phillips 66. The 2017 NEI inventory was prepared by the EPA by extrapolating the existing 2011 one to 2017; the formal release of the 2017 NEI is scheduled for 2020 (2017 NEI Final Plan, EPA). The meteorology used for the simulations is the same as with the 2012 episode.

For 2017, the same analyses with 2012 using the Direct Decoupled Method (DDM) in CMAQv5.0.2 were conducted. Overall sensitivity of O3 to NOx goes down for all sources when compared to 2012 (Figure 3.5 vs. Figure 3.8), attributed to NOx reductions, resulting in a 1 ppb reduction to domain-average NO_x concentrations. As with 2012, ozone is still mostly impacted by NO_x emissions from onroad sources, and VOC emissions from industrial activities (Figure 3.9). The sensitivity of $PM_{2.5}$ goes down for all sectors due to emission reductions (Figure 3.10). Due to meteorology being the same between the two years, identical patterns are observed.

Similarly with 2012, NO_x emissions from the Cedar-Bayou plant had the strongest impact on Houston's ozone, while, VOCs emitted from the Lake Charles facility had the strongest impact to the maximum 8-hour ozone in the vicinity for Phillips 66 facilities. The magnitude of these sensitivities remains largely the same between 2012 and 2017.

It is interesting to note that while ozone sensitivity to NO_x emissions is reduced in magnitude for all sectors when compared to 2012, its sensitivity to VOCs goes up by a total of approximately 40% for the aggregate of human emissions, which is indicative of a shift to a NO_x limited regime (Figures 3.8, 3.9). A finding which, for regulatory purposes, means that controlling for NO_x emissions is starting to show diminishing returns, and VOC reductions are becoming more efficient at controlling ozone.

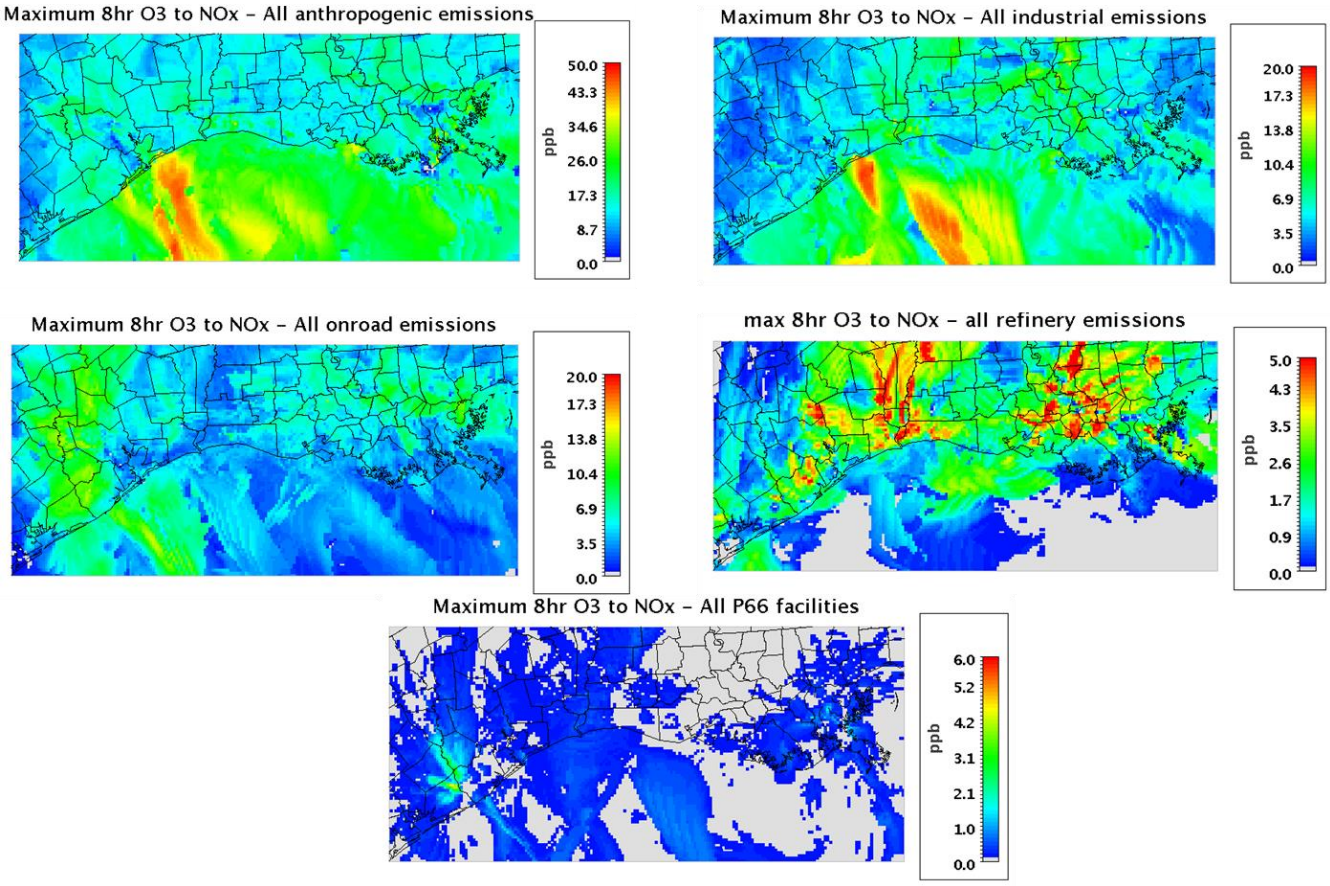

Figure 3.8 2017 episode maximum 8-hour ozone sensitivity to NO_x to emissions from all anthropogenic activities, industrial operations, onroad sources, refining and all Phillips 66 facilities. The maximum 8-hour ozone sensitivity, corresponds to the sensitivity of ozone to NO_x at the time the maximum 8-hour ozone is observed, which, is different for each cell

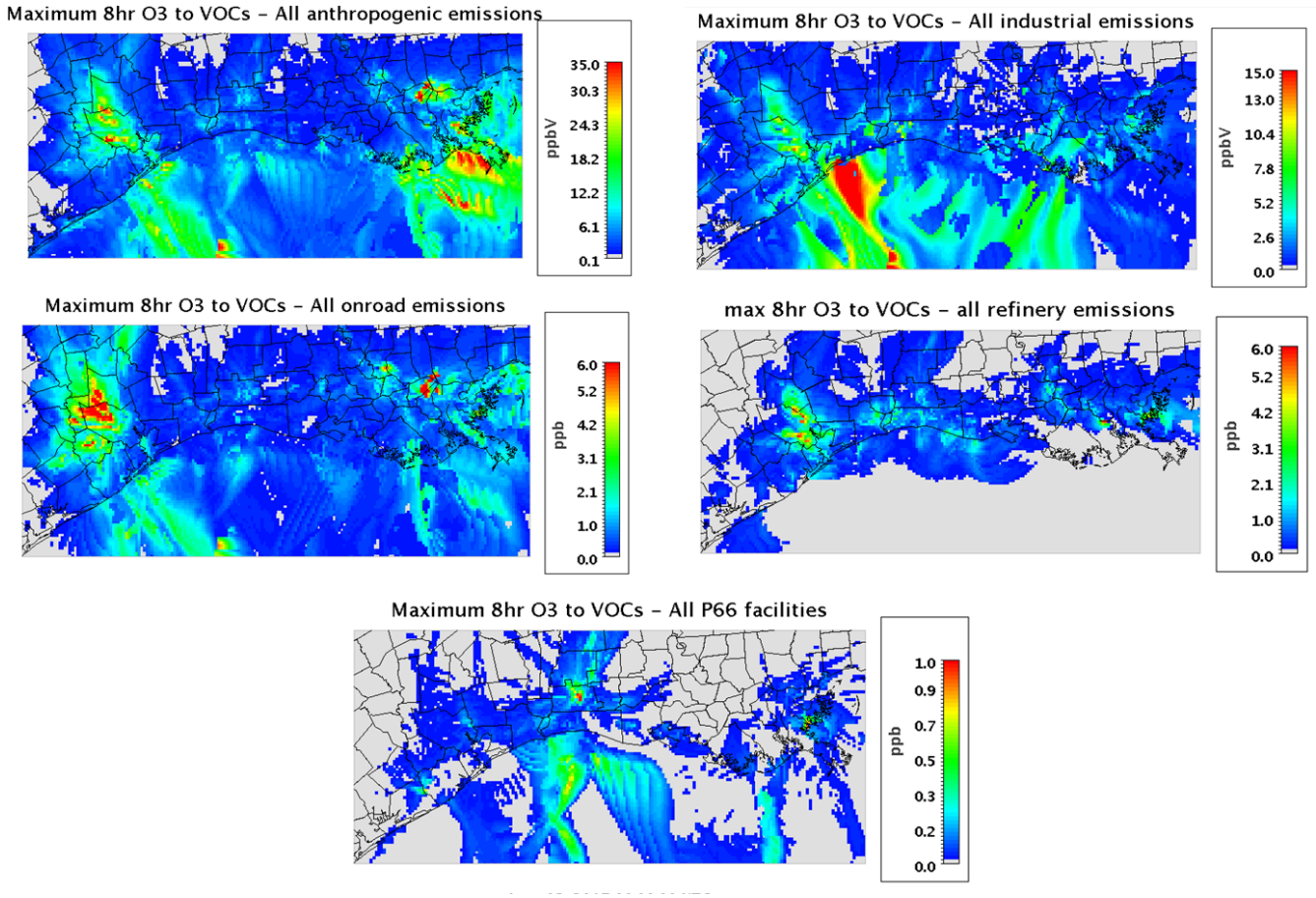

Figure 3.9 2017 episode maximum 8-hour ozone sensitivity to VOCs to emissions from all anthropogenic activities, industrial operations, onroad sources, refining and all Phillips 66 facilities. The maximum 8-hour ozone sensitivity, corresponds to the sensitivity of ozone to VOCs at the time the maximum 8-hour ozone is observed, which, is different for each cell

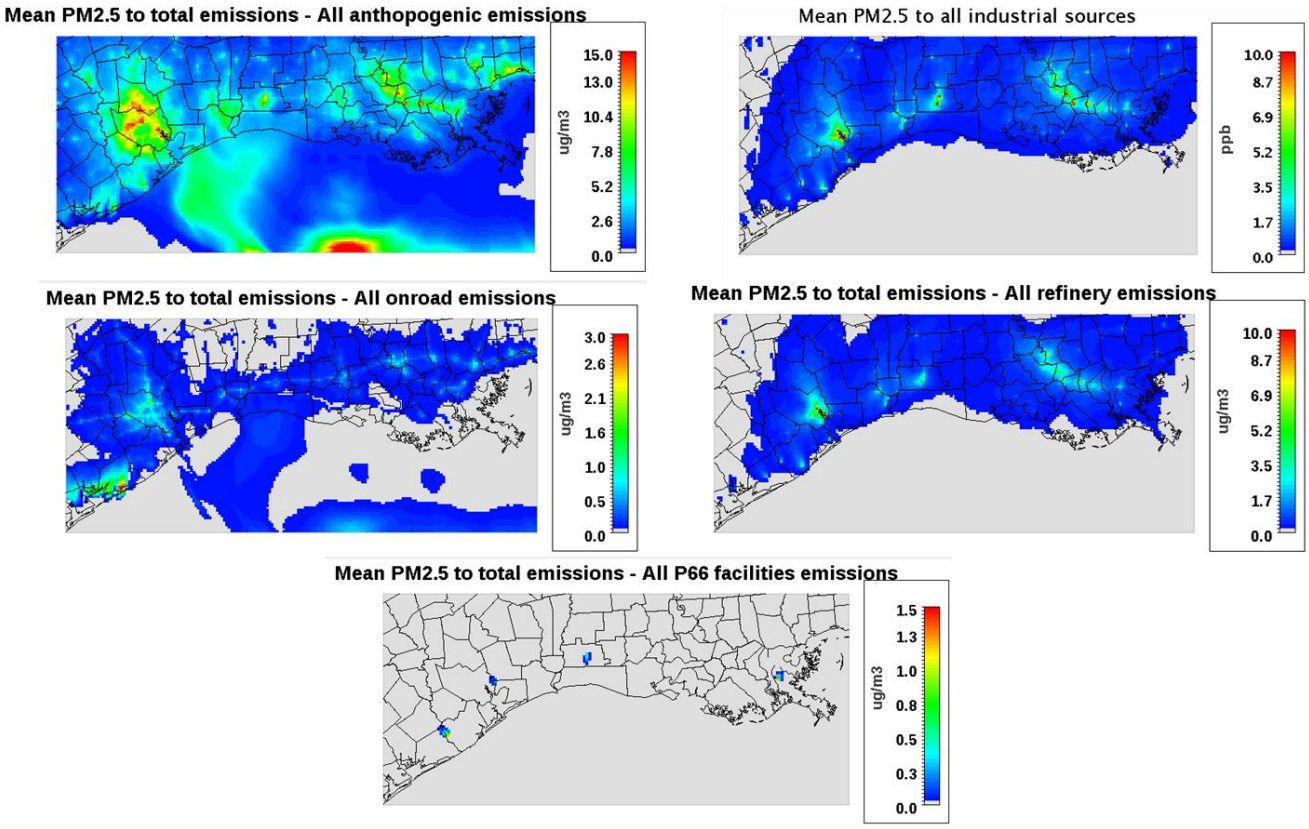

Figure 3.10 2017 episode mean PM2.5 sensitivities to total emissions from all anthropogenic activities, industrial operations, onroad sources, refining and all Phillips 66 facilities

3.2.6 Expansion impact on air quality

The expansions include the P66 Sweeny Fractionation plant, P66 Sweeny Tier 3 Gasoline unit upgrades, Freeport LPG Export Terminal, P66 butane/butylene storage, CPChem Ethane Cracker, CPChem polyethylene Units, and CPChem Ethylene Expansion (10th furnace). As expected, sensitivity patterns for the Baytown and Sweeny expansions follow the ones of Cedar Bayou due the meteorology. To validate the modelling results, the ratio of sensitivities was compared to the ratio of emissions from these two facilities, and they were found to be in excellent agreement.

In 2017, the total impact of the expansion to the maximum 8-hour ozone is 0.6 ppb at the emitting grid cell, and it rapidly abates further from the source, being less than 0.1 ppb 20 km away. The same is observed for $PM_{2.5}$, with its sensitivity to total emissions being 0.1 μg m^{-3} at the emitting grid cell and less than 0.01 μg m^{-3} 20 km away. As with 2012, meteorology shifts to south prevailing winds after the first 20 days, which affects the predicted sensitivity patterns.

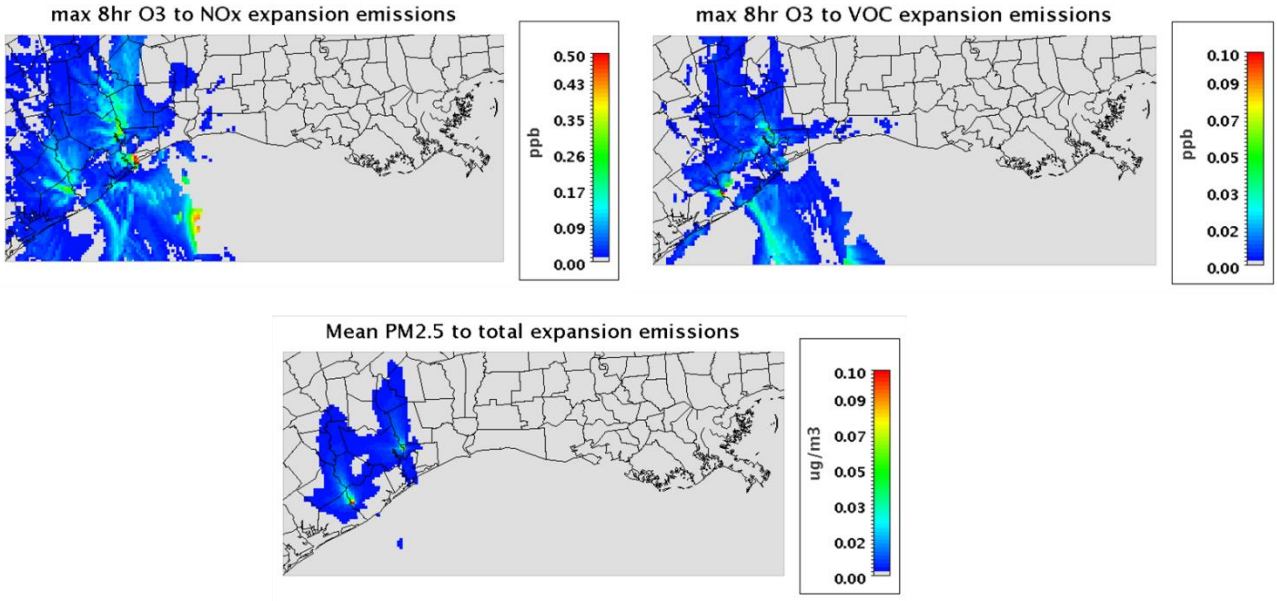

Figure 3.11 2017 episode maximum 8-hour ozone sensitivity to NOx and VOCs, and mean PM2.5 sensitivity to total emission of the two expansions

CHAPTER 4

CONSTRAINING IEPOX AND IEPOX-DERIVED SOA FORMATION IN CMAQ

Biogenically derived aerosol has been found to have appreciable impacts on climate and air quality. There are large uncertainties however, associated with the magnitude of this impact, mainly because of the incomplete understanding of their production mechanisms, which leads to significant underprediction of biogenic Secondary Organic Aerosol (SOA) levels in state-of-the-art Air Quality models. To address this issue, we utilize the rich 2013 Southern Oxidant and Aerosol study (SOAS) dataset of both ground and aloft measurements, collected at the Centrerville, Alabama site to enhance the extensive mechanism of IEPOX-mediated SOA formation implemented in the Community Multiscale Air Quality (CMAQ) model (Pye et al., 2013). A wide range of sensitivity studies were carried out to investigate the main sources of uncertainty in the process of isoprene conversion to SOA through the IEPOX pathway. Available observations of key intermediate species (isoprene, IEPOX, ISOPOOH, MVK, MACR, methyltetrols, organosulfates and others), were used to constrain highly uncertain reaction rate constants, as well as partitioning and deposition coefficients of the relevant species. The Henry's law coefficient for IEPOX was found to be one of the most important of parameters that controls aqueous isoprene OA products, and a value of 1.9×10^7 M atm^{-1} provides the best agreement with measurements. Results suggest a strong correlation of isoprene OA with sulfate, and little correlation with acidity or liquid water content, consistent with correlations derived from the SOAS data set. Moreover, given the ever-reducing SO_2 emissions, we investigated the response of IEPOX aerosol to further reductions for the

entire US, where, consistent with previous literature an almost linear decrease of IEPOX aerosol is seen for a corresponding decrease in sulfate.

4.1 Introduction

Isoprene (C_5H_8) is the most common abundant Biogenic Volatile Organic Compound (BVOC) emitted by foliage and trees (Guenther et al. 2006), constituting a significant contributor to the total SOA load especially in the Southeastern (SE) US, where observations have found that isoprene-derived OA can comprise up to 30% of the total organic aerosol (OA) (Xu et al. 2015). Anthropogenic pollutants interact with isoprene gas phase products (Weber et al. 2007, Xu et al, 2015) through a multi-step chemical mechanism, as seen from correlations between biogenic SOA (BSOA) and sulfate which support this finding (Weber et al. 2007, Xu et al. 2015, Budisulistiorini et al. 2015, 2017).

One of the main gas-phase oxidation products of isoprene are isoprene epoxydiols (IEPOX), which is a fourth-generation product of isoprene's reaction with the hydroxyl radical. The proposed mechanism requires that IEPOX diffuses from the gaseous phase in an acidic, aqueous environment, where it reacts with a nucleophilic seed such as SO_4^{-2} to produce SOA (Nguyen et al. 2014b). This SOA exhibits an almost linear association with the amount of available sulfate (Xu et al. 2015), while, at the same time, showing little dependence on liquid water content and acidity, suggesting that sulfate is the controlling factor for the amount of isoprene OA being produced in the SE US. Given that natural emissions of BVOCs such as isoprene and terpenes in the SE are the highest in the continental US, and coupled with significant anthropogenic emission sources in the vicinity such as power plants and automobiles, increased aerosol formation is expected (Kleindienst et al. 2007). The interactions between the anthropogenic and biogenic species have been

extensively studied in recent years (Xu et al. 2015, Budisulistiorini et al. 2015, 2017, Pye et al. 2013); the underlying mechanisms of SOA formation however, are still not fully constrained since parameters controlling specific reaction steps remain highly uncertain (Lin et al. 2013, Nguyen et al. 2014).

One reason that makes observations in the Southeast of such interest, is that biogenically-derived SOA can comprise up to half of the total organic mass in the summer time and up to 30% year-around ((Kleindienst et al., 2007, Offenberg et al., 2011, Weber et al., 2007, Xu et al., 2016). Terpene species such as a-pinene and b-pinene, are significant contributors to the mass of SOA, since they react very fast with atmospheric oxidants with high yields (Acosta 2013). In addition, recent studies (Carlton et al. 2013) have shown that isoprene is also producing SOA, and its mass yield is not only significant, but in many cases surpasses that of terpenes. Most of this SOA is formed through the IEPOX pathway, with the major products being methyltetrols, organosulfates and to a lesser extent, organonitrates (Pye et al. 2013, Budisulistiorini et al. 2015, 2017). Given the high levels of aerosol water, low aerosol acidity and high SO_2 emissions (Guo et al. 2015, Weber et al. 2016) high levels of IEPOX-OA are expected, something that is validated by both measurements (Xu et al. 2015) and modelling studies (Pye et al. 2013).

In this study, we utilize the observations from the SOAS campaign taken at the Centerville, Alabama, Southeastern Aerosol Research and Characterization (SEARCH) (Edgerton et al. 2005, 2006) monitoring location, which took place between June 1st and July 15th, 2013. The objectives of the campaign are detailed in Carlton et al. 2013, with a strong focus on investigating the interactions between anthropogenic emissions and BVOCs. Since the campaign took place in a densely-forested area, the emissions of BVOCs

such as isoprene, a-pinene and b-pinene, were expected to be high and therefore play an important role in the region's climate. High concentrations of SOA were observed, and SOA resulting from isoprene oxidation alone exhibited concentrations of the order of 2 $\mu g/m^3$ (Budisulistiorini et al. 2015, Xu et al. 2015).

By making use of the existing measurements of gas-phase precursors and aerosol, we evaluate and improve the isoprene OA formation mechanism in CMAQ, by constraining reaction rate constants for isoprene oxidation, as well as partitioning parameters such as the uncertain Henry's law constant. CMAQ exhibits a negative bias in modelled OA concentrations (Pye et al. 2013), especially SOA from isoprene oxidation. Only recently was the IEPOX pathway implemented in CMAQ (Pye et al. 2013) and GEOS-Chem (Marais et al. 2016), but large uncertainties remain in system controlling parameters. This chapter aims at performing an extensive comparison of model results to data, and calibration of model constants to enable the model to reproduce the observed correlation between sulfate and isoprene SOA, as well as reduce the bias between predicted and observed organic matter. Given the close relationship between sulfate and IEPOX-OA (Xu et al. 2015), and the expectation that SO_2 emissions will keep declining in the future, we investigated the sensitivity of IEPOX-OA levels to sulfate reductions over the entire US and performed an assessment of potential future scenarios.

4.2 Methods

4.2.1 Chemical transport model & measurements

For the needs of this chapter, the Community Multiscale Air Quality (CMAQ) model was used (Byun and Schere 2006). CMAQ is a three-dimensional, Eulerian, atmospheric chemistry and transport model, that simulates the processes atmospherically relevant compounds undergo such as emission, diffusion, chemical reactions and deposition. A version of CMAQ with extended isoprene chemistry (Pye et al. 2013) is employed, that includes formation of IEPOX OA (hereafter IEPOX OA) from the reactive uptake of isoprene epoxides into aqueous phase aerosol. The aqueous phase formation of IEPOX-OA is controlled by the IEPOX uptake coefficient (Pye et al. 2013), which is a function of Henry's law coefficient (H).

Simulations were conducted using a 36 km x 36 km resolution grid over the continental US for the SOAS campaign period, with 5 days used as a start-up. Meteorological data were developed using the Weather Research Forecasting (WRF) model and converted to CMAQ inputs using the MCIP processor. Unless otherwise stated, all results shown in this paper are specific to the grid cell that includes the Centreville site, to allow for comparison with the SOAS measurements.

The base biogenic emissions were calculated online using the Biogenic Emission Inventory System (BEIS) (Vukovich and Pierce, 2002). BEIS uses the meteorological data in order to obtain variables governing the magnitude of BVOC emissions, such as solar irradiance (SR), temperature (T), as well as land data (plant type and plant coverage of each grid cell) to determine the fluxes of BVOCs. Non-volatile cations have been found to have a significant impact on pH and they have been found to be present in incorrect

amounts in CMAQ (Fourotan et al. 2017, Vasilakos et al. 2018) and therefore they have been removed from the simulations as to not bias the results.

Multiple simulations were conducted in order to gauge the ability of the model to reproduce the measurements (Allen et al., 2015, Nguyen et al. 2014b, Brophy and Farmer 2015, Carlton et al., 2013) and the correlations that govern them, and parameters and inputs associated with IEPOX-OA formed via the IEPOX mechanism were modified accordingly.

For the sulfate sensitivity tests, total SO_2 emissions across the US were reduced by 25, 50, 75 and 100% and their impact on IEPOX-OA was quantified.

4.2.2 Chemical mechanism

Chamber experiments and field observations find that the dominant pathway for the formation of SOA through isoprene involves the formation of intermediate IEPOX, (Lin et al. 2013, Nguyen et al. 2014, Budisulistiorini et al. 2015, 2017, Xu et al. 2015). However, current CTMs do not replicate this finding, suggesting this could be a major shortcoming in CTMs, that explains the low bias in OA simulated, in general, and the IEPOX-OA levels in particular. In recent modelling studies (Pye et al. 2013, Marais et al. 2016), a similar mechanism was introduced in CMAQ and GEOS-Chem, using IEPOX as an intermediate for isoprene OA formation and found that 15-20% of the total SOA can be attributed to isoprene oxidation products. The mechanism as is implemented in the CMAQv5.0.2 is described in Figure 4.1.

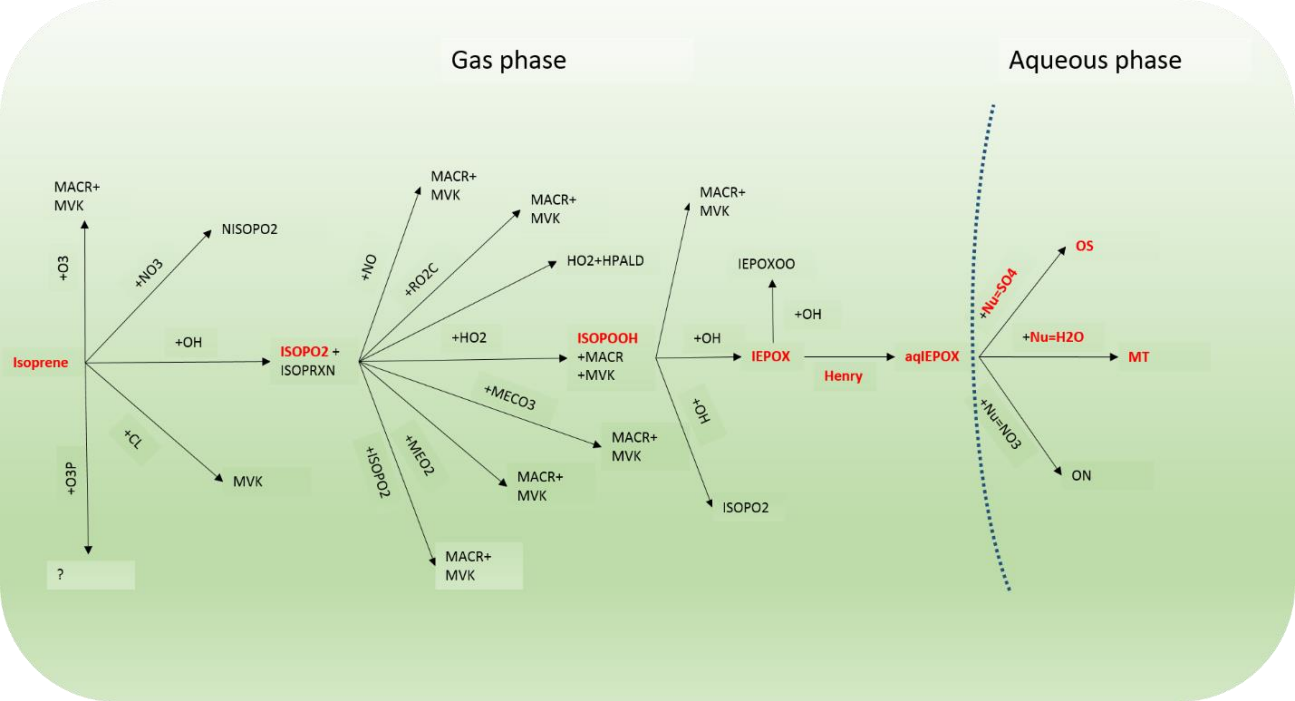

Figure 4.1 IEPOX OA formation mechanism as implemented in the latest version of CMAQ (Pye et al. 2013)

4.3 Results

4.3.1 Ozone, NOx and sulfate

In all simulations including the base scenario, there is good agreement between the measurements and the simulated values of atmospherically relevant compounds at the Centreville site. Ozone is strongly correlated with the measurements, but exhibits a consistent positive bias of approximately 10 ppb (Figure 4.2a), while NO_x is captured well, albeit with less variability than the measurements (Figure 4.2b). Reasons for positive biases in model simulations of ozone in the SE US have been explored in Travis et al. 2016 and could include but are not limited to errors in vertical mixing and production rates within the PBL. For aerosol species, sulfate closely tracked the measurements (Figure 4.2d), but is 26% lower during the mid-day. Although there is an appreciable amount of isoprene OA predicted for the SE US, for the SOAS site IEPOX-OA was much lower than the

amount estimated from the PMF measurements by almost 1.2 μg m^{-3}. All of the above species, except for IEPOX-OA, changed little with the modifications discussed below. for the optimal H simulation is about 30% lower than the PMF factor for SOAS (Xu et al. 2015) (Figure 4.2c).

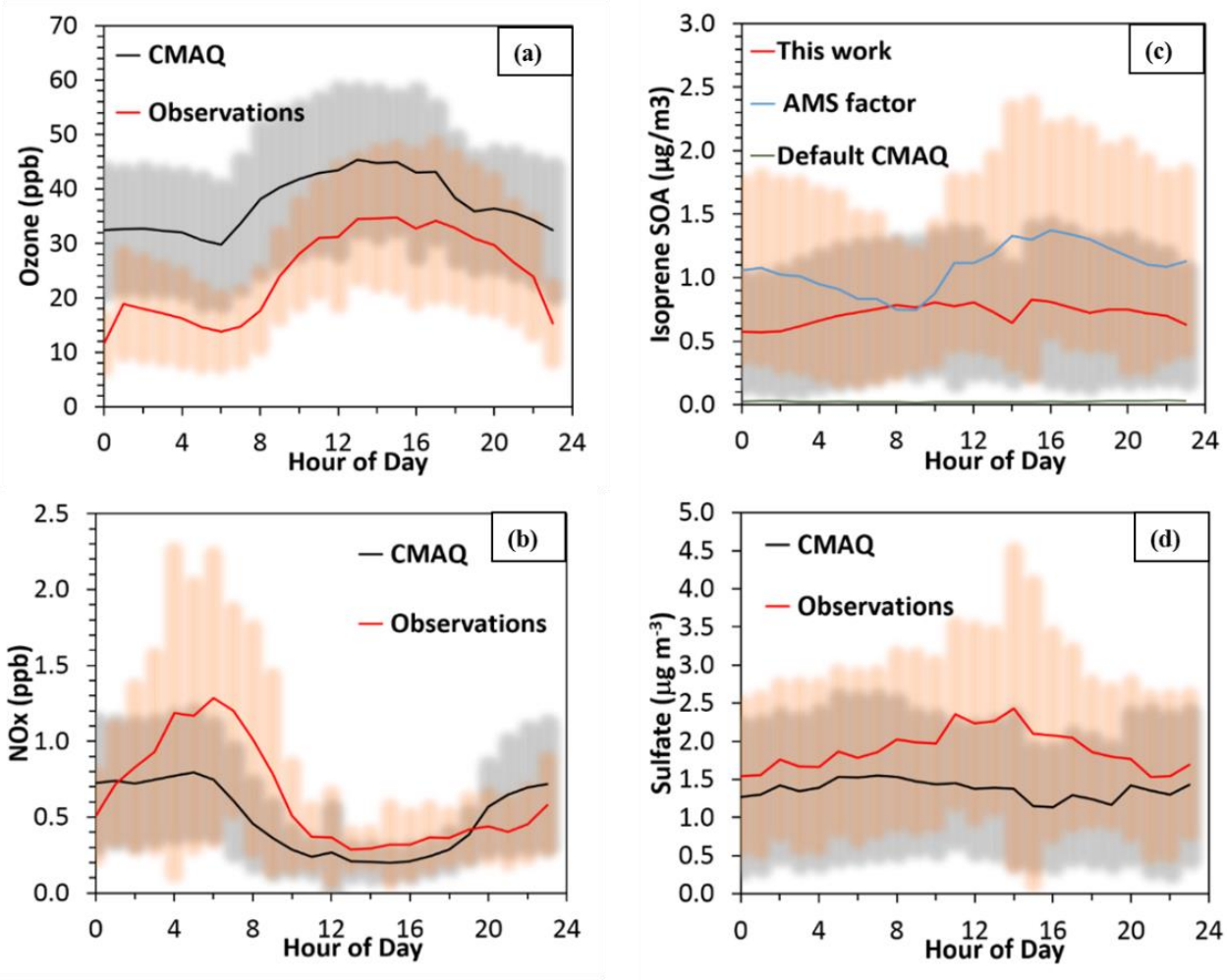

Figure 4.2 Diurnal profiles during the SOAS campaign for measured (red) and simulated (black) (a) ozone, (b) NO_x, (c) isoprene SOA and (d) sulfate. The shaded areas represent one standard deviation at each diurnal hour

4.3.2 Henry's law sensitivity tests and updates to the simulations

4.3.2.1 Baseline simulation

Our initial simulation (hereafter baseline) was using the default version of CMAQ as described in Pye et al. 2013. For this case, the Henry's law coefficient for IEPOX was set to 2.7e6 M atm^{-1}. Biogenic emissions for isoprene were not changed and left to the value generated by BEIS. The deposition surrogate used to calculate the dry deposition of IEPOX was methylhydroxyperoxide (CMAQ species VD_OP), with a relatively low H of 3.1e2 M atm^{-1}. The planetary boundary layer height (PBL) was calculated by the WRF meteorology and used as is.

Results from the baseline simulation indicated that IEPOX-OA was severely underestimated, especially methyltetrols (MT) and organosulfates (OS). Isoprene levels were biased low during the day time and exhibited a night time high, suggesting that the isoprene emissions from BEIS were not accurate (Figure 4.3). However, IEPOX levels were overestimated when compared to the observations by a factor of 10. The relative ratios of IEPOX derived OA (OS to MT) compared favorably with the observations, suggesting that the aqueous chemical mechanism represents the underlying physics accurately. Similarly, important gas phase and aerosol species, such as ozone, NO_x and sulfate were accurately predicted, although with some bias. To alleviate the issues identified with the simulation, we applied a number of sequential updates to the model by making use of the available measurements, in order to ensure that the gas phase products were as close as possible to the observed values before attempting any changes in the aqueous chemistry.

4.3.2.2 PBL prescription & Isoprene emission fitting (IEF)

In order to rectify the unrealistic isoprene profile, the first change we applied to the model was the assimilation of PBL data available from SOAS. The PBL height predicted

from WRF was biased high during the day and biased low during the night compared to observations, which is a known issue with WRF (Hu et al. 2013), that could explain the isoprene daytime low and its nighttime high. Results from the PBL simulation, indicated that this change had little impact on all important tracers. Daytime isoprene levels remained similar to the baseline simulation, while there was a slight decrease of the nighttime high by 1 ppb (Figure 4.3). The PBL simulation indicated that the behavior of the isoprene levels was driven by the emissions and not by the meteorology, corroborated by simulated temperature profiles that closely matched the observed profiles.

Isoprene emissions in our simulations were under-predicted during the day time and overestimated during the night time, which led to the spike in isoprene concentration during the night (Figure 4.3). To rectify the issue, the measured isoprene emissions as well as the emissions predicted by BEIS were used, in order to come up with scaling factors with which modelled isoprene emissions were multiplied at each model timestep as to better match the observed and simulated levels. As an initial guess the ratio of the measured to simulated values was used, which was then optimized through multiple linear regressions, to achieve better agreement between model and measurements. This simulation (referred to as isoprene emissions flux, or IEF) significantly improved isoprene levels and eliminated the daytime low and the nighttime high (Figure 4.3).

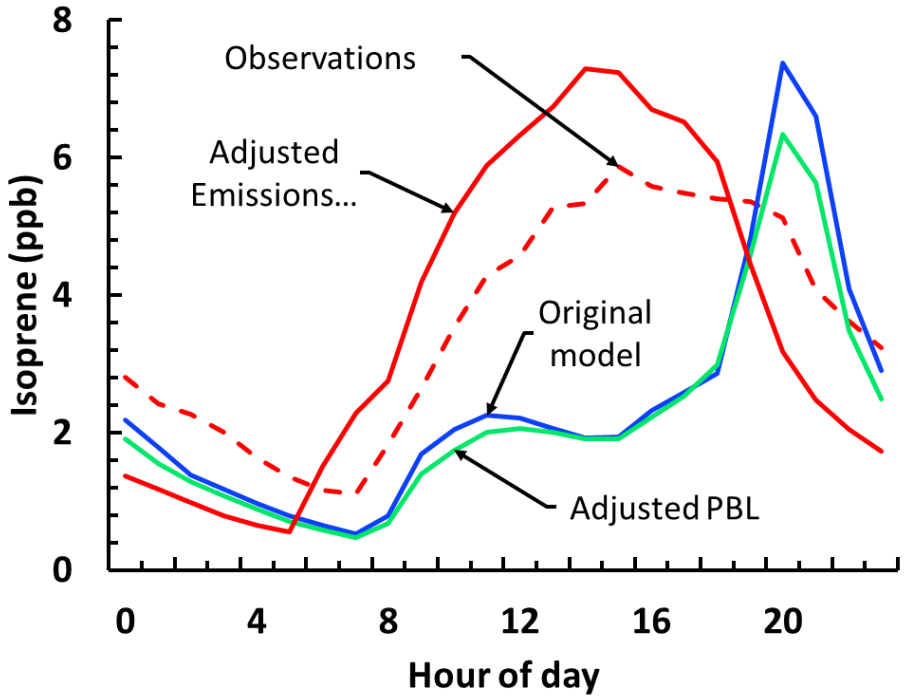

Figure 4.3 Observed (dashed-red), default model (blue), adjusted PBL (green) and adjusted emissions (solid red) isoprene diurnal profiles for the Centreville gridcell. Concentrations at each hour correspond to the campaign average for that hour

4.3.2.3 IEPOX deposition correction (DEP)

While the IEF simulation improved isoprene levels, the extreme overestimation of IEPOX still remained. Dry deposition for IEPOX is expected to be a significant loss process, given the stickiness of the molecule (Paulot et al. 2009); however, the deposition surrogate used in CMAQ was methylhydroxyperoxide which has a Henry's law constant four orders of magnitude less than that of IEPOX, meaning that depositional loss of IEPOX to wet surfaces was most likely significantly underestimated (depositional time scale of τ=11 h). By changing the surrogate to HNO_3 in the deposition-adjusted (DEP) update, the timescale was reduced by 50% and there was a marked decrease of IEPOX levels to half of what they originally were. Surprisingly, IEPOX-OA levels were not impacted by this

change, suggesting that other processes were rate-controlling with regards to SOA production.

4.3.2.4 Updated IEPOX gas phase oxidation and Henry's law sensitivity tests

After both the IEF and DEP changes, the IEPOX levels were still positively biased when compared to observations. A potential reason could be the underestimation of the gas phase IEPOX oxidation loss to OH. The rate constant used for the gas phase loss of IEPOX for the previous simulations was 1.5e-11 cm^3 $molecules^{-1}$ s^{-1} (Paulot et al. 2009). We updated the rate constant for the gas phase loss of IEPOX to OH, to a value of 3.6e-11 cm^3 $molecules^{-1}$ s^{-1} (Jacobs et al. 2013). The updated oxidation simulation, slightly reduced IEPOX levels by 5%, while keeping IEPOX-OA levels approximately constant. The IEPOX overestimation remained (Figure 4.4) which implies that the existing sinks are still not significant enough or there is another removal process (for example an additional gas phase reaction) which is not included in the model. The precursors to IEPOX such as ISOPOOH compare well with the measurements, corroborating that the issue lies in one of the IEPOX sinks.

After the above changes, and ensuring that there is sufficient gas phase IEPOX available to react in the aqueous phase, the negative bias for IEPOX-OA persisted and the linear relationship between sulfate and IEPOX-OA was still not captured (Xu et al 2015). The IEPOX Henry's law constant is one of the most uncertain parameters of the system (Eddingsaas et al. 2010) and at the same time one the most important ones, since it directly controls the amount of IEPOX that is available in the aqueous phase to produce SOA. The literature reported range for the Henry's law constant for IEPOX spans more than 2 orders of magnitude (Eddingsaas et al. 2010, Pye et al. 2013, Wang et al. 2017), so a number of sensitivity tests were performed to estimate a value led to the most consistent results

between the model and measurements, using as a constraint the correlation between sulfate and IEPOX-OA from Xu et al. (2015), since it's a better indicator for the accuracy of the chemical processes included in the model than the concentration of IEPOX-OA. We observed an almost linear relationship between the average levels of isoprene OA and the logarithm of H (Figure 4.5). A value of 1.9×10^{7} M atm^{-1}, which is similar to recent estimates, yields the best overall agreement (Budisulistiorini et al. 2015, Nguyen et al. 2014, and Chan et al. 2010). A comprehensive list of simulated scenarios is shown in Table 5.1.

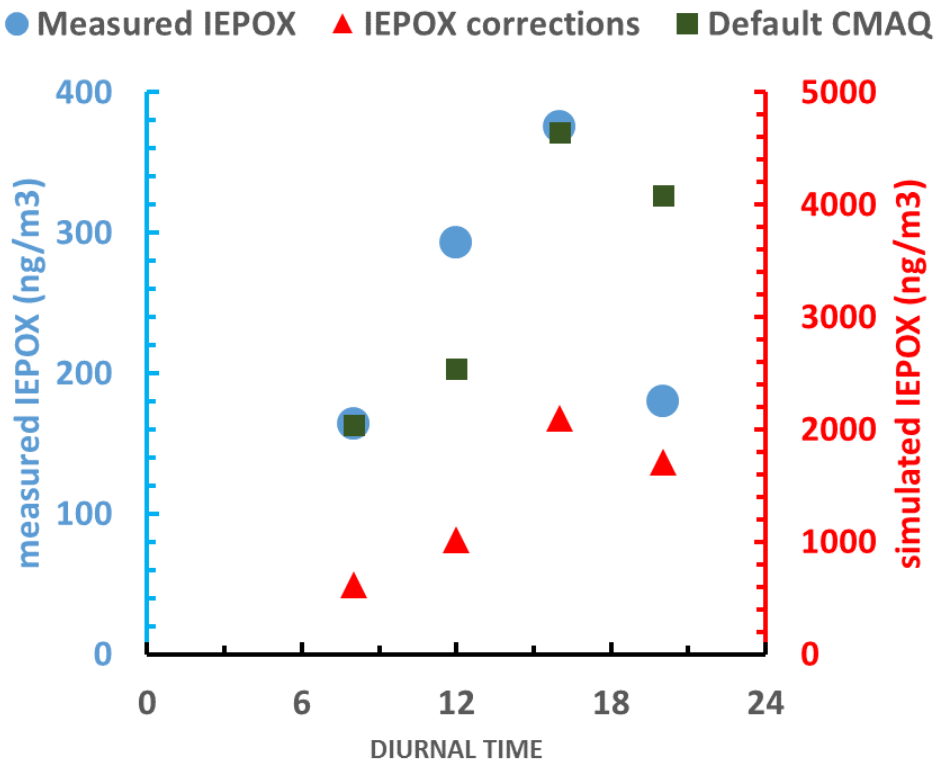

Figure 4.4 Measured (cyan), default CMAQ (green) and corrected (red) IEPOX diurnal concentrations. The IEPOX corrections data refers to IEPOX levels after updating both the deposition surrogate and the reaction rate constant for the OH^{-} reaction

Table 4.1 List of simulated scenarios and their specifications. The Henry's law coefficient H is equal to 2.7 106 M atm^{-1}

SIMULATION NAME	*PBL VALUE*	*ISOPRENE EMISSIONS*	*IEPOX DEPOSITION SURROGATE*	*IEPOX+OH⁻ OXIDATION CONSTANT*	*H* SCALING FACTOR*
BASELINE	default	default	VD_OP	Paulot	1
PBL	assimilated	default	VD_OP	Paulot	1
IEF	assimilated	changed	VD_OP	Paulot	1
DEP	assimilated	changed	HNO3	Paulot	1
OXIDATION	assimilated	changed	HNO3	Jacobs	1
HENRY 1	assimilated	changed	HNO3	Jacobs	2.5
HENRY 2	assimilated	changed	HNO3	Jacobs	5
HENRY 3	assimilated	changed	HNO3	Jacobs	7
HENRY 4	assimilated	changed	HNO3	Jacobs	9
HENRY 5	assimilated	changed	HNO3	Jacobs	10
HENRY 6	assimilated	changed	HNO3	Jacobs	100

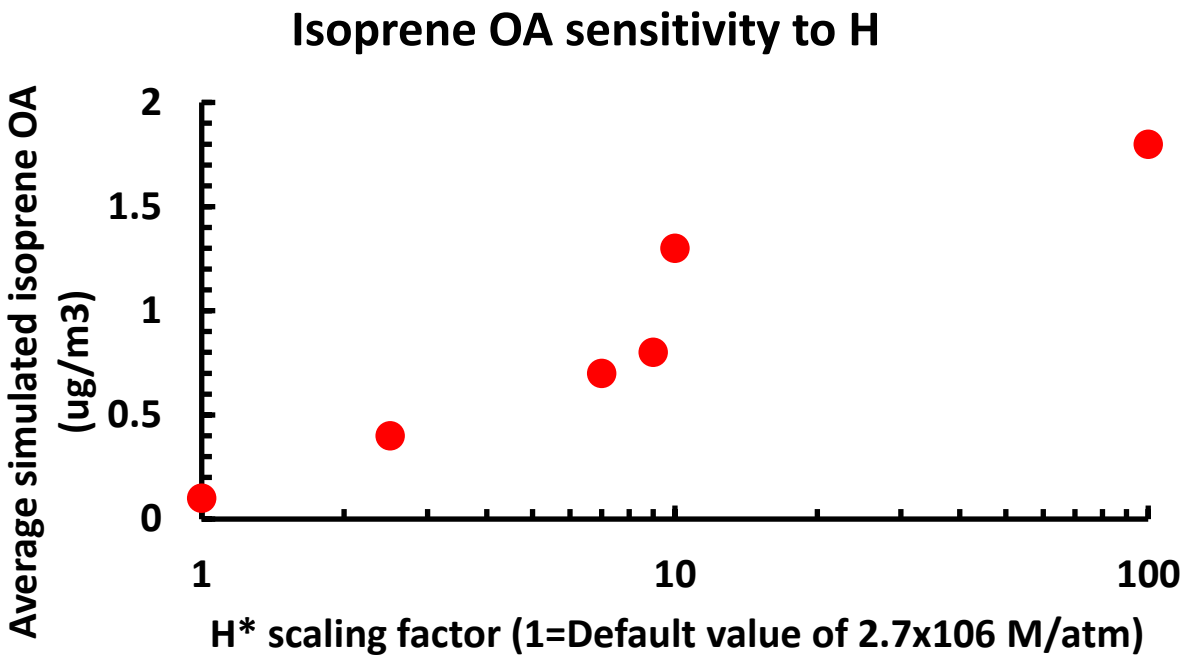

Figure 4.5 - Results for Henry's law sensitivity tests. The x axis is in units of 2.7e6 M/atm, which corresponds to the default H value in the Pye 2013 CMAQ version

4.4 Comparing aqueous SOA to observations

4.4.1 Polyols and organosulfates

In the base simulation, methyltetrols (MTs) were underestimated (Figure 4.6). The suite of changes described above increased MT levels which are closer to observed levels. Although triols are not included in the current version of CMAQ, model MTs can be a first order approximation to the sum of the measured triols and MTs.

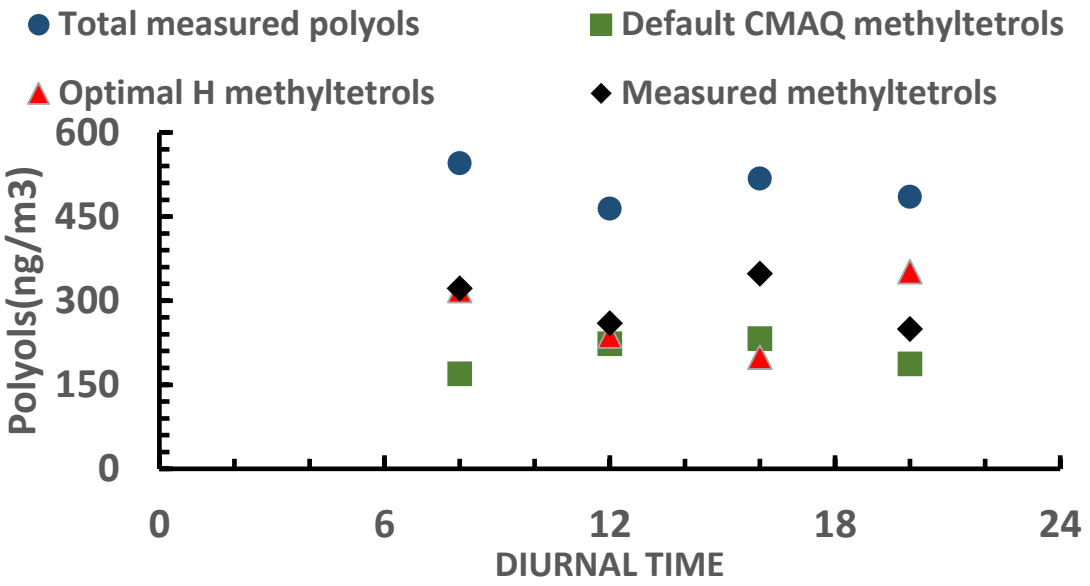

Figure 5.6 4 hour averaged diurnal concentrations for measured methyltetrols (black) and total polyols (blue), default CMAQ (green) and optimal H CMAQ (red)

Similar to MTs, organosulfates were also biased low in the base simulations (Figure 5.7). The revised model inputs and parameters increased OS levels, they are still lower than the measurements.

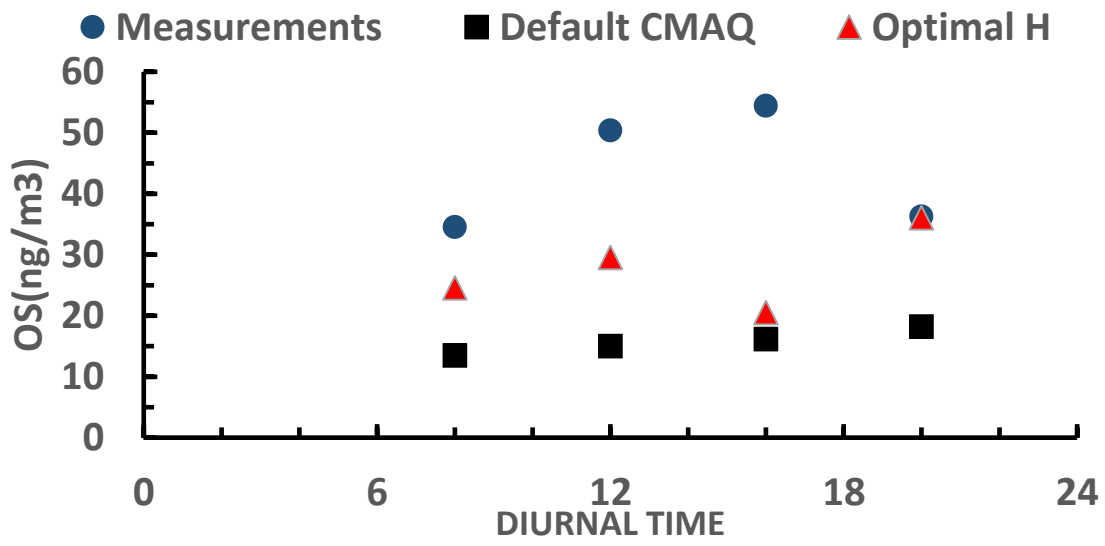

Figure 5.7 - 4 hour averaged diurnal concentrations for measured organosulfates (blue), default CMAQ (black) and optimal H CMAQ (red)

For both OS and MT, the time of the largest discrepancy between the measurements and model is in the afternoon. Given that it has been shown that sulfate controls the amount of isoprene OA being produced (Xu et al. 2015, Budisulistiorini et al. 2015), the underestimation can be attributed in part to the low bias in the simulated sulfate during the mid-day (Figure 4.2d).

4.4.2 Correlation with sulfate

Recent studies (Xu et al. 2015, Budisulistiorini et al. 2015, 2017) have observed a strong correlation between sulfate and isoprene OA in the vicinity of the SE US. To test the validity of the isoprene OA production mechanism in the current version of CMAQ, we used the coefficients of this linear relationship (slope and intercept) as the main parameters to be optimized with our Henry's law sensitivity tests.

In the base case, there was a correlation between sulfate and isoprene OA; however, the levels of isoprene OA were far too low and the slope almost 0 (Figure 4.8). Using an H of $1.9x10^7$ M/atm, the simulated and observed correlations achieve remarkable agreement.

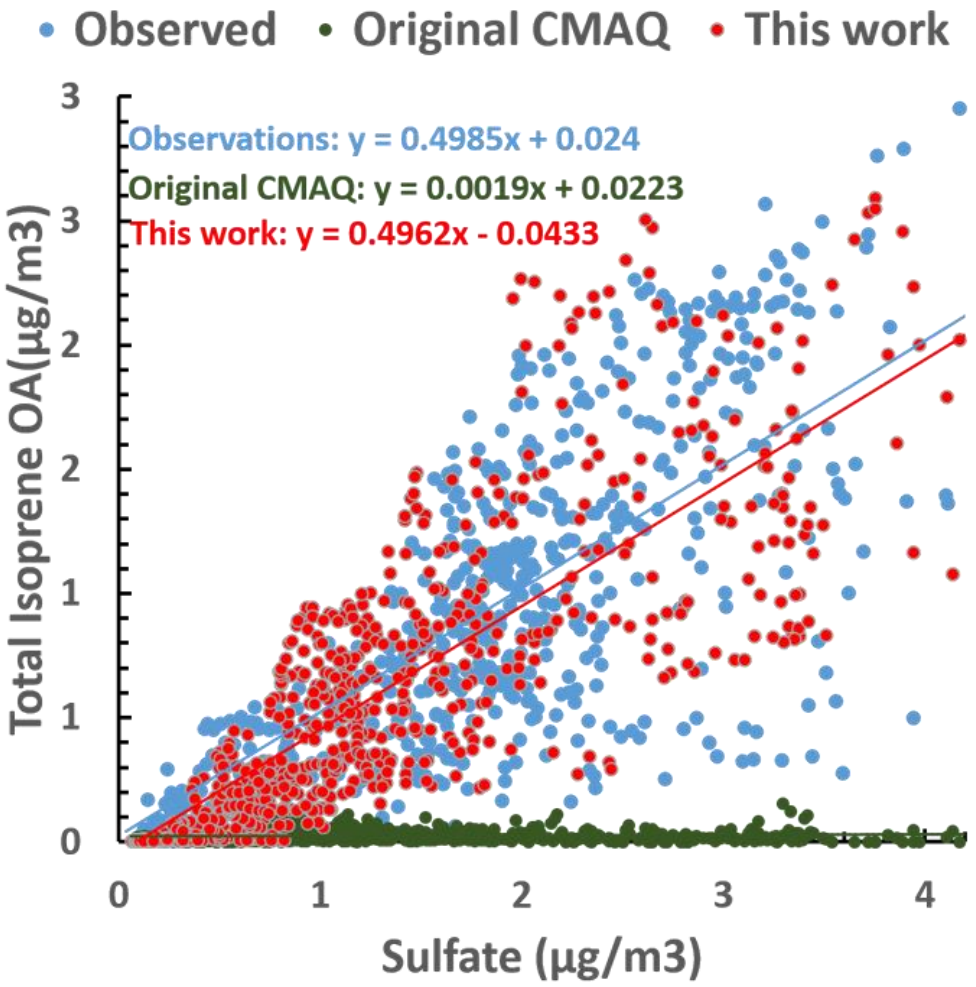

Figure 4.8 - Correlation between sulfate and isoprene OA for the SOAS observations (blue), base scenario (green) and optimal H simulation (red)

The other two important parameters which have been found to control the formation of isoprene OA are acidity (H^+) and particle water (H_2O_{ptcl}) (Surrat et al. 2010, Nguyen et al. 2014, Xu et al. 2015, Budisulistiorini et al. 2015). However, for the case of the SE US, only weak correlations between isoprene OA and H^+ or H_2O_{ptcl} have been observed (Xu et al. 2015, Budisulistiorini et al. 2015).

There is an abundance of aerosol water in the SE, while, at the same time, the mean pH in Centreville was close to 1 (Guo et al. 2015, Vasilakos et al. 2018). The weak correlation can be explained since at high aerosol water levels and low pHs, they are not limiting parameters, and small changes in their value do not affect isoprene OA levels.

Another possible explanation for the strong correlation with sulfate and the weak correlation with H^+ and H_2O_{ptcl}, is the competition between acidity and particle water, since increased levels of particle water lead to dilution of ions and reduced pH. In addition, the dilution could weaken a potential salting-in effect, suppressing the IEPOX uptake from the gas phase.

We observe similar behavior in the model when we perform multivariate linear regression on our results, indicating that the current version of the model is able to correctly capture the chemistry behind IEPOX-OA production. The regression coefficients are provided in Table 4.2.

Table 4.2 Results for multiple linear regression of IEPOX-OA with respect to sulfate, particle water and H^+

Regression variable	Regression coefficient in the measurements (Xu et al. 2015)	Regression coefficient for the simulations
Sulfate	0.424	0.527
Water	-0.004	0.029
H^+	0.009	0.007

4.5 The impact of dust on IEPOX-OA

NVCs are present in all size ranges of atmospheric aerosol, although predominantly found in the coarse mode (Guo et al. 2017, Fang et al. 2017, Vasilakos et al. 2018). Recently, biases in CMAQ have been identified, where incorrect amounts of NVCs are distributed in the accumulation mode (Vasilakos et al. 2018), leading to aerosol pH predictions that are inconsistent with the ones obtained using measurement data (Guo et al. 2015, Vasilakos et al. 2018). Given the dependence of IEPOX-OA formation on particle acidity, pH biases can also translate to biases in its formation. Because of that, NVCs have been removed from the previous simulations, but a separate simulation to determine their impact was carried out.

Figure 4.9 quantifies the impact that NVCs can have on IEPOX-OA levels, after all the updates have been implemented on the code, while using the optimal H value. Specifically, when they are excluded from the model (Figure 4.9a), high concentrations of IEPOX OA are observed in the forested areas of the SE and Eastern US up to 1.8 $\mu g\ m^{-3}$ in the Ozarks, Tennessee and Arkansas area, consistent with literature sources (Carlton & Baker, 2011). The pH values for these areas are very low ranging from 0 to 1.5, in agreement with the overall trends from Guo et al. 2015. When the CMAQ predicted NVCs are included in the simulation (Figure 4.9b), the spatial pattern for IEPOX OA remains the same, albeit with marked decreases in concentrations everywhere in the domain. Specifically, the difference between the two simulations is nearly 0.6 $\mu g\ m^{-3}$ - almost 30% (Figure 4.9c) - driven by the increased pH in the simulation where NVCs are included,

where it's almost 1 to 2 units higher. This discrepancy in pH predictions is a major source of biases in CMAQ for not only IEPOX OA but also aerosol nitrate (Vasilakos et al. 2018) and needs to be addressed in a future model update.

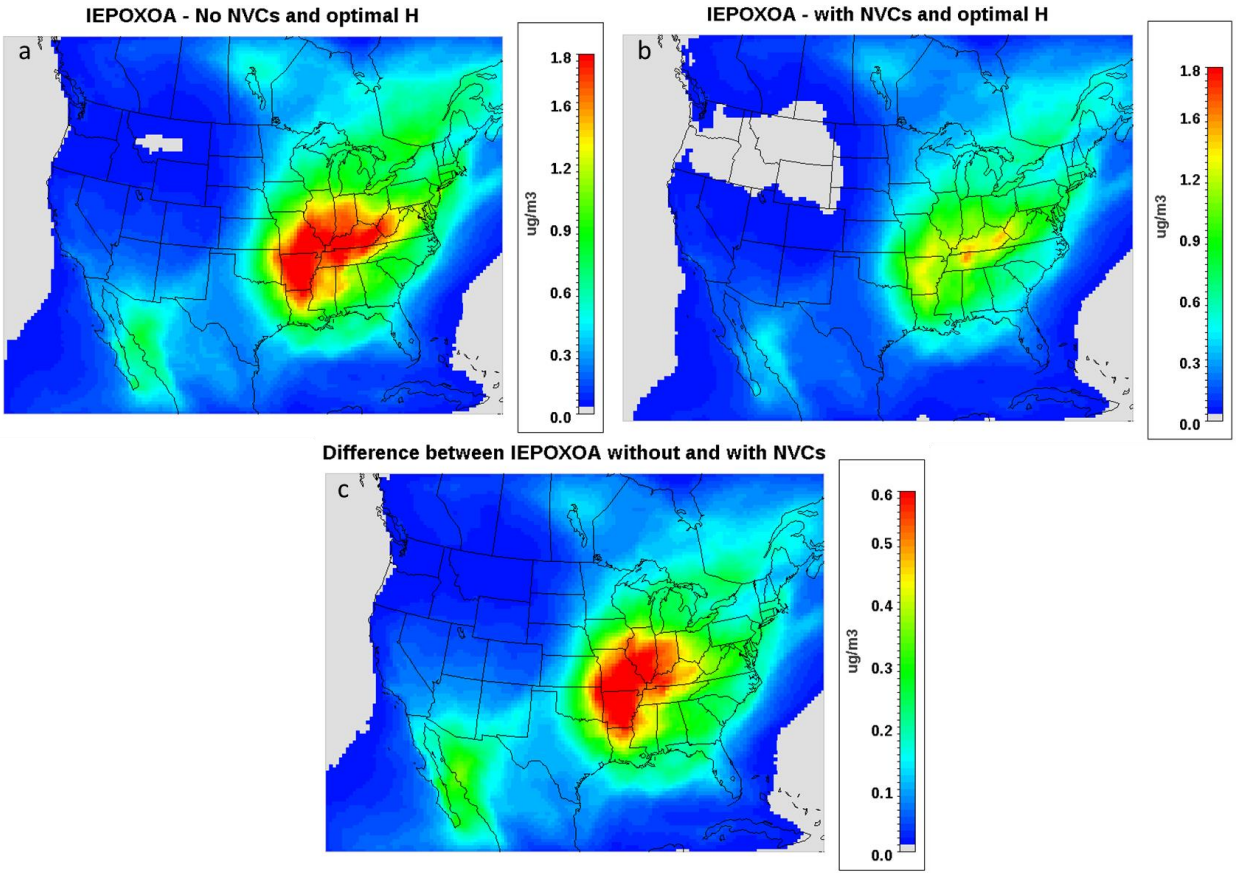

Figure 4.9 Campaign average predicted IEPOX OA when NVCs are excluded (a) and included (b) in the simulations, as well as the difference (c) between the two fields. Simulations for these cases are carried out with all the code updates active

4.6 SO_2 reductions and the future of IEPOX OA

Throughout the preceding decade, great strides have been made with regards to improvements on air quality, driven by continuous emission reductions. SO_2 in particular has seen decreases of almost 7% per annum (Blanchard et al. 2011) for the last decade.

Since IEPOX OA formation and SO_4 availability are intertwined, it is expected that IEPOX OA levels will drop in response to the SO_2 reductions, something that has been corroborated in previous modelling studies looking at the effect of SO_4 reductions on IEPOX OA (Budisulistiorini et al. 2017). To investigate, we used the updated model and decreased total SO_2 emissions by a set amount (25, 50, 75 and 100%) to quantify the impact of future reductions on IEPOX OA.

The greatest decreases in magnitude are seen for the first 25% in reductions (Figure 4.10a), with an almost 60% drop in IEPOX OA production over the Eastern and SE US, consistent with results from Budisulistiorini et al. 2017. This is a combination of multiple factors, since the removal of sulfate from the system translates to slightly more alkaline aerosol, coupled with markedly reduced liquid water availability. Further reductions (Figure 4.10b, c, d) also affect IEPOX OA levels, but the drop in IEPOX OA levels is not as pronounced. This is because the removal of sulfate rapidly reduces particle water, until a threshold value of about 1 $\mu g\ m^{-3}$ is achieved when no sulfate exists in the system. While the drop in water concentrations is the highest for the first 25% of removed SO_2, it decreases in magnitude when more sulfate is removed. When approaching 100% SO_2 removal, production of OS is shut down and the only constituents of IEPOX OA is methytetrols and a negligible amount of organonitrates ($ON \leq 0.01\ \mu g\ m^{-3}$). The other isoprene OA pathways from methacrylic acid epoxide (MAE) as well as hydroxymethylmethyl-α-lactone (HMML) are still producing approximately the same amount of aerosol throughout all simulations.

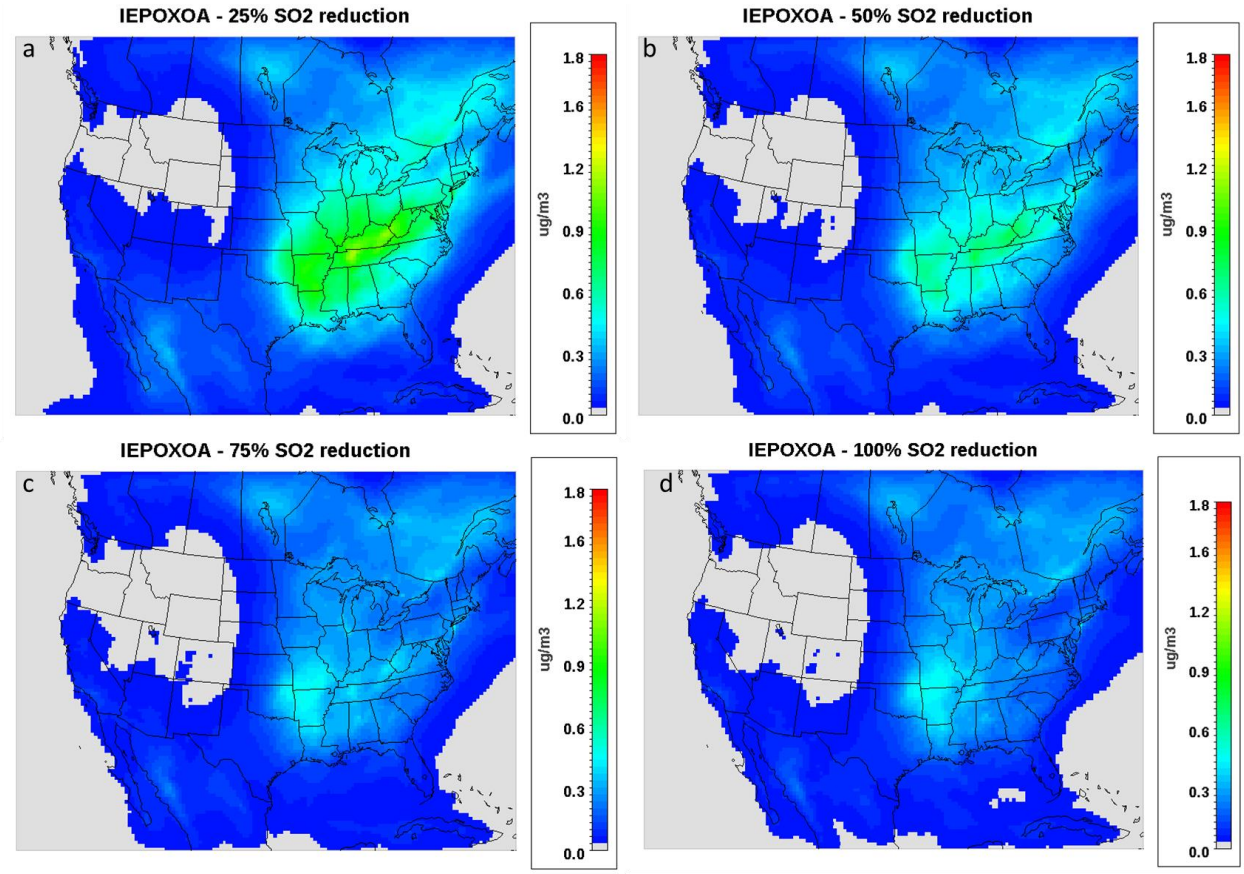

Figure 4.10 Simulated IEPOX OA fields over the CONUS for 25% (a), 50% (b), 75% (c) and 100% (d) SO_2 emission reductions

4.6 Conclusions

Organic matter and isoprene aerosol in particular are significantly underestimated in current CTMs. The recent study by Xu et al. 2015 underscored the importance of anthropogenic influence on isoprene OA formation and the potential of IEPOX-OA to comprise a significant part of the total aerosol mass. Utilizing a CMAQ version with updated isoprene chemistry we conducted simulations for the SOAS campaign period, and made model updates based on the extensive data set available from the campaign. We tested the ability of the model to reproduce the observed levels of IEPOX-OA, as well as the relationship between IEPOX-OA and sulfate.

The base configuration of CMAQ captured the dynamics of ozone, NO_2 and sulfate, though there was a positive bias in ozone and a negative bias in sulfate in the afternoon. Isoprene-derived SOA levels, as well as OA in general, were biased low. In addition the current version of BEIS implemented in CMAQ, produced isoprene emissions which were dynamically inconsistent with the observed values. Model parameters and inputs that control the formation of isoprene-derived aerosols were varied to improve its representation of SOA formation, focusing on SOA resulting from IEPOX chemistry. In particular, isoprene emissions were adjusted to be more in accordance with the observed concentrations and fluxes and the treatment of IEPOX were made that led to IEPOX and other species were more in line with observations. The Henry's law constant for IEPOX was found to be of particular importance. A value of 1.9×10^7 M atm^{-1} led to closest agreement between modelled and observed concentrations of isoprene-derived SOA also captured the observed correlation of sulfate and isoprene OA.

The updates to the model also led to little correlation between isoprene OA and acidity (H^+) or particle water (H_2O_{ptcl}), consistent with recent studies (Xu et al. 2015 &

Budisulistiorini et al. 2015). The high aerosol water levels and low pH found in the SE US (Guo et al. 2015, Weber et al. 2016) is a possible explanation for the lack of correlation since at this regime they do not constitute limiting parameters. An increase of H_2O_{ptcl} would be accompanied with dilution of H^+, negating the possible increase of IEPOX OA production. However, this may very well change in the future with additional SO_2 reductions, since the aerosol is expected to become slightly more alkaline, while, at the same time, available aerosol water will drop significantly.

Results indicate the need for changes in the calculation of isoprene emissions in BEIS, and the more accurate representation of the physical processes that IEPOX undergoes during its lifetime. Laboratory experiments and field studies elucidating the formation of IEPOX triols, which are not included in the model, and comprise a significant portion of IEPOX OA, would also allow for a better prediction of the remaining isoprene OA fraction not predicted by CMAQ.

CHAPTER 5

UNDERSTANDING NITRATE FORMATION IN A WORLD WITH LESS SULFATE

SO_2 emission controls, combined with modestly increasing ammonia, have been thought to generate aerosol of significantly reduced acidity, where sulfate is partially substituted by nitrate. However, neither expectation agrees with decadal observations in the Southeastern US, suggesting that a fundamentally different response of aerosol pH to emissions changes is occurring. We postulate this "nitrate substitution paradox" arises from a positive bias in aerosol pH in model simulations, exacerbated by reductions in SO_2 emissions. This bias can elevate pH to where nitrate partitioning is readily promoted, leading to behavior consistent with "nitrate substitution". CMAQ simulations are used to investigate this hypothesis; predictions of $PM_{2.5}$ pH for 2001 emissions compare favorably with observations; for 2011 emissions however, predicted pH increases by 1 unit, presenting a positive trend not seen in the observations. Non-volatile cations (K^+, Na^+, Ca^{+2} and Mg^{+2}) in the fine mode are found responsible for most of this trend. pH biases of 1 unit can induce a nitrate bias of 1-2 μg m^{-3} which may further increase in future projections, reaffirming an otherwise incorrect expectation of "nitrate substitution". Evaluation of predicted aerosol pH against thermodynamic analysis of observations is therefore a critically important, but overlooked, aspect of model evaluation for robust emissions policy.

5.1 Introduction

Aerosol acidity is a driver of many important atmospheric processes (Guo et al. 2015, Weber et al. 2016, catalyzing the conversion of isoprene oxidation products to form secondary organic aerosol (SOA) (Xu et al. 2015, Pye et al. 2013, Surrat et al. 2010, Eddingsaas et al. 2010), driving the semi-volatile partitioning of key aerosol species processes (Guo et al. 2015, Weber et al. 2016), as well as the solubilization of iron, copper and other trace metals in aerosol which may serve as nutrients for ecosystems (Meskhidze et al. 2003), but also prove toxic for humans (Ghio et al. 2012, Fang et al. 2017). Significant reductions in primary pollutant emissions over the last decades has greatly improved air quality in the developed world, and is also thought to fundamentally affect aerosol acidity. SO_2, an important aerosol precursor and a major driver of its acidity, has seen decreases of about 6% yr^{-1} over the 2001-2011 period alone in the US, with a continued anticipated downward trend (West et al. 1999, Pinder et al. 2007, 2008). Emissions of NO_x and the resulting acidic HNO_3, are also declining. In contrast, ammonia, the primary basic fine mode aerosol precursor, is either constant or increasing (Pinder et al. 2007, 2008, Heald et al. 2012), owing to intensified agricultural activity and livestock farming from the demands of population growth. These trends have created the expectation that the aerosol has and will become increasingly neutralized (West et al. 1999, Pinder et al. 2007, 2008, Heald et al. 2012, Tsimpidi et al. 2007, Saylor et al. 2015), with ammonium sulfate being replaced, at least in part, by ammonium nitrate (West et al. 1999, Bauer et al. 2007, Bellouin et al. 2007, Li et al. 2014, Goto et al. 2016).

The concept of "nitrate substitution" of sulfate has largely been based on the notion that nitrate is volatile when the aerosol is acidic, and in turn aerosol is acidic when

insufficient amounts of total ammonia (i.e., gas+aerosol) or dust non-volatile cations (NVCs) exist to neutralize aerosol sulfate. Based on this conceptual model, aerosol ionic molar ratios have largely been used as proxies of aerosol acidity (pH), so that when the aerosol ammonium to sulfate molar ratio approaches 2 (the composition of ammonium sulfate), aerosol is assumed "neutral" and only then nitrate aerosol can form (Fisher et al. 2011, Hennigan et al. 2015, Wang et al. 2016, Silvern et al. 2017). Modeling studies have corroborated this view, predicting that nitrate substitution may be prevalent in the future, including the Southeastern US (SE US) (Heald et al. 2014, Baeur et al. 2007, Bellouin et al. 2011, Li et al. 2014, Goto et al. 2016, Vayenas et al. 2005, Karydis et al. 2016). A more careful analysis however (Guo et al. 2015, Weber et al. 2016, Hennigan et al. 2015, Guo et al. 2016) reveals that this conceptual model of aerosol acidity and conditions for nitrate substitution fails; thermodynamic analysis of SE US aerosol observations instead show that fine mode aerosol remains strongly acidic, despite a 70% reduction in sulfates, and more than sufficient total ammonia to neutralize it. The strong acidity is maintained by the large difference in volatility between sulfate and ammonia (Guo et al. 2015, Weber et al. 2016), so large changes in total ammonia concentrations are required for a notable change in aerosol acidity, about one order of magnitude increase in NH_3 concentration per unit increase in aerosol pH (Guo et al. 2015 & 2017a). However, ammonia gas deposits relatively rapidly, limiting its build up except in high emissions regions. Throughout the decade, the levels of aerosol nitrate have remained relatively constant throughout the US (Guo et al. 2015, Weber et al. 2016, Pye et al. 2009). The persistent strong aerosol acidity in turn explains why nitrate aerosol has not considerably increased over the last decades, and is unlikely to appear in the immediate future in the SE US. These findings constitute a

"paradox", as the same thermodynamic models (e.g., ISORROPIA-II Fountoukis & Nenes 2007) used to demonstrate the aerosol tendency for strong acidity in the SE US (Guo et al. 2015, Weber et al. 2016) using ambient data, is also used in 3D modeling studies (Pye et al. 2009, Heald et al. 2012) for the region that predict nitrate substitution as a possible aerosol response.

Reconciling the "nitrate substitution paradox" requires a careful examination of aerosol thermodynamics and the conditions under which nitrate partitioning to the aerosol is favored. Meskhidze et al. (2003) and later Guo et al. (2016) showed that for aerosol nitrate formation to occur, aerosol pH needs to exceed a certain characteristic value (that depending on the temperature and the amount of liquid water, ranges between a pH of 1.5 and 3; Guo et al., 2017). If aerosol pH is therefore high enough (typically above a pH of 2.5 to 3), a behavior consistent with "nitrate substitution" emerges, because any inorganic nitrate forming from NO_x chemistry mostly resides in the aerosol phase. When pH is low enough (typically below 1.5 to 2), nitrate remains exclusively in the gas phase (as HNO_3), regardless of the amount produced, and "nitrate substitution" is not observed. Between these "high" and "low" pH values, a "sensitivity window" emerges (of typically 1-1.5 pH units), where partitioning shifts from nitrate being predominantly found as gas to where it is mostly found as an aerosol. Therefore, if a model is for any reason biased in its prediction of aerosol pH, it may be preconditioned towards nitrate prediction biases. The sensitivity to pH biases is strongest when the aerosol lies in the pH "sensitivity window", which is often the case for atmospheric aerosol (Guo et al. 2015, 2016 & 2017, Bougiatioti et al. 2016). When below this "pH sensitivity window", aerosol nitrate is almost nonexistent and

relatively insensitive to emissions (and pH biases); when above the window, almost all nitrate resides in the aerosol phase, and directly responds to NO_x emission controls.

If aerosol were composed only of non-volatile sulfate and semi-volatile nitrate and ammonium, prediction biases in pH could result only from errors in RH, and large errors (e.g., order of magnitude) of NH_3, NO_x and SO_2 because pH is relatively insensitive to changes in these aerosol precursors (Hennigan et al. 2015). Acidity however can also by modulated by other soluble inorganic cations from seasalt and mineral dust, such as K^+, Na^+, Ca^{+2} and Mg^{+2}. The low volatility of these cations allows them to preferentially neutralize sulfates over NH_3, and, even in small amounts elevate particle pH to levels that can promote the partitioning of nitrates to the aerosol phase (Fountoukis & Nenes 2007, Guo et al. 2017). NVCs tend to reside in the coarse mode aerosol (Guo et al. 2015, West et al. 1999, Vayenas et al. 2005), with a fraction found in smaller particles, while sulfate tends to reside in the fine mode (Guo et al. 2015, West et al. 1999, Vayenas et al. 2005); the degree to which NVCs can affect fine mode pH therefore lies in the degree to which the two types of species mix across different particle sizes. Potential interactions between inorganics-organics can also affect aerosol acidity. However, recent studies driving thermodynamic models utilizing water associated with organics find only minimal differences between predicted pH (Guo et al. 2015, Bougiatioti et al. 2016). In the presence of very high NVCs (for example in sea-spray aerosol), where the aerosol has much higher pH, the pH can approach the pK_a of organic acids, leading to conditions where their dissociation can contribute to aerosol acidity (Laskin et al. 2012).

Although aerosol models are evaluated in terms of their ability to predict the concentration of aerosol species (including across size), no studies to date focus on their

ability to predict aerosol pH across size, even though it is known to potentially vary up to 6 units (Fang et al. 2017, Bougiatioti et al. 2016, Li et al. 2017). Evaluation of models in this context is challenging, since there is no direct measurement of acidity for an aerosol population, making thermodynamic models the most accurate way of inferring pH. Furthermore, given that most of this pH variability occurs in the PM_1 to $PM_{2.5}$ range (Fang et al. 2017), it is quite likely that model assumptions on how aerosol species interact within a mode (degree of internal mixture), especially for particles in the 1-2.5 μm range, may lead to pH prediction biases that drive model behavior.

This aim of this chapter is to address the underlying reasons for the "nitrate substitution" paradox, and in the process, provide a conceptual framework for quantifying and understanding the importance of aerosol pH biases. The guiding hypothesis of this work is that aerosol pH prediction bias fundamentally changes predicted aerosol behavior and the underlying cause of the paradox. The approach is demonstrated with the Community Multiscale Air Quality (CMAQ) model (Byun & Schere 2006) and is based on predictions of pH over the 2001-2011 period in the Southeastern/Eastern US, being the region for which aerosol pH trends are constrained by observations. The role of internally-mixed nonvolatile cations in $PM_{2.5}$ as a source of the pH bias is then assessed.

5.2 Methods

5.2.1 Predicting aerosol pH and composition

CMAQ is a three-dimensional, Eulerian, atmospheric chemistry and transport model, that simulates the processes atmospherically relevant compounds undergo such as emission, diffusion, chemical reactions and deposition (Byun & Schere 2006). CMAQ version 5.0.2 was used in this study, and simulations were carried out using a 36-km

horizontal resolution grid, with 13 vertical layers, over the continental US (CONUS) for the entire years of 2001 & 2011. Meteorological data were obtained offline from the Weather Research Forecasting (WRF) model. The same meteorology was used between the two years to eliminate potential biases of temperature and relative humidity on pH predictions. Model-ready emissions for 2011 were obtained using the National Emissions Inventory 2011 inventory (NEI 2011) for the Carbon Bond 05 (CB05) chemical mechanism. To estimate the 2001 emissions, the 2011 emissions for SO_2, NO_x, NH_3, CO, VOCs and primary PM from anthropogenic sources were scaled on a per-species basis using the Air Pollutant Emissions Trends Data; emissions for other species were kept constant. Emissions of biogenic species were calculated online using the Biogenic Emission Inventory System (BEIS).

The aerosol thermodynamic model ISORROPIA-II (subversion 2.2 - dated 2012 – Fountoukis & Nenes 2007) was used online in CMAQ to drive the semivolatile partitioning of inorganic species, and, offline to analyze the predicted $PM_{2.5}$ pH, nitrate partitioning tendency and sensitivities thereof to nonvolatile cations. It should be noted that ISORROPIA and CMAQ only account for the thermodynamic interactions between inorganic species and do not treat organics. Offline calculations were conducted using the hourly gas and particle phase concentrations output from CMAQ for the 2001 and 2011 simulations, which includes NVCs, and using them as input to ISORROPIA-II. The thermodynamic calculations online and offline were carried out in forward mode, meaning that the temperature, relative humidity, as well as all aerosol and gas phase concentrations were known and used as input, assuming that the aerosol is in a metastable state, where only one aqueous phase is allowed to exist (Fountoukis & Nenes 2007). While this

assumption is not always necessarily true, especially under conditions of low relative humidity (RH<30%) where the aerosol can exist in glassy, amorphous states, for the majority of cases observational data shows that it is a valid assumption (Guo et al. 2015, Bougiatioti et al. 2016, Liu et al. 2017). We run the model under a variety of conditions to determine the impact of NVCs from dust and sea salt (Ca, Mg, K, Na) on pH, its seasonal variability, as well as the effect of pH and temperature on nitrate partitioning.

5.3 Results and discussion

5.3.1 Predicted Sulfate, ammonium & nitrate

For the main inorganic aerosol species (SO_4, NO_3 and NH_4), CMAQ captures the observed downwards trends (Park et al. 2006, Hand et al. 2012, Blanchard et al. 2013a, b, Kim et al. 2015, Saylor et al. 2015) over the CONUS during the course of the decade (Figure 5.1). As expected, sulfate over the entire US drops significantly between 2001 and 2011, by about 30%, with major decreases in the Eastern US of about 2 $\mu g\ m^{-3}$. Areas impacted the most by these reductions, are places of significant industrial activity or with significant coal-fired electricity generating units (EGUs), such as the Ohio River Valley, Baton Rouge in Louisiana and South Carolina. Ammonium levels remain rather constant, since ammonia saw minimal emission changes over the decade, and only experience small reductions which are a buffered response to the decrease in sulfate levels. Local reductions (~20%) in ammonia are seen over North Carolina and Louisiana. Aerosol nitrate concentrations remain relatively constant on average over the domain, with small increases over the Eastern US. The highest levels of ammonium are observed in areas with significant livestock, such as North Carolina; sulfate concentrations are the highest around the area of the Ohio River Valley, and so is nitrate due to significant NO_x and SO_x emissions.

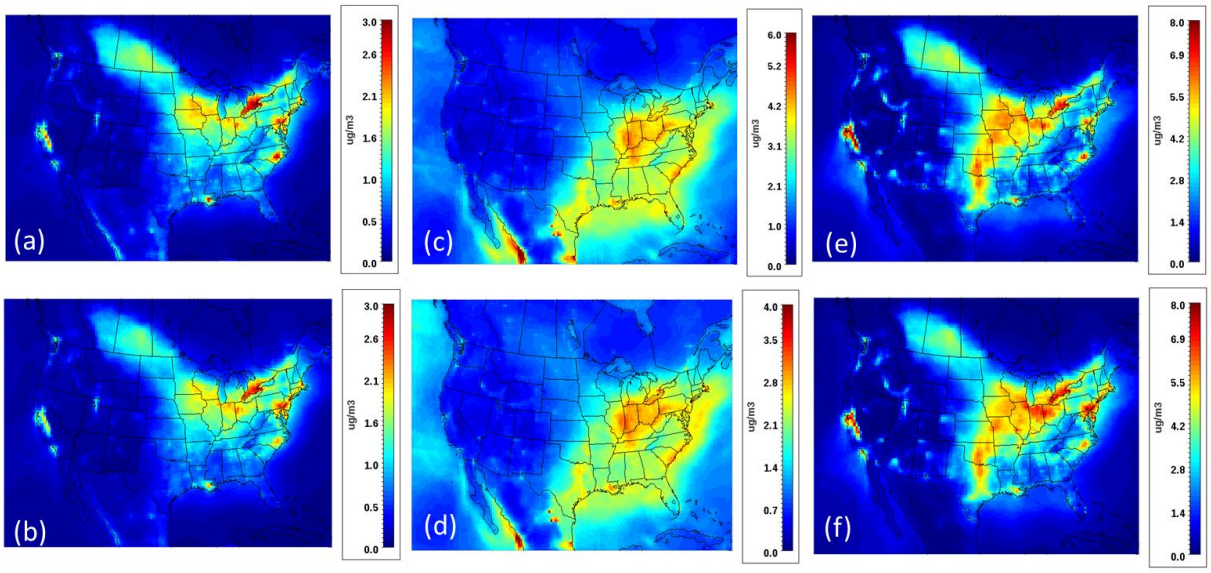

Figure 5.1 Yearly averaged predicted concentration fields of (a) 2001 NH_4, (b) 2011 NH_4, (c) 2001 SO_4 (d) 2011 SO_4, (e) 2001 NO_3, (f) 2011 NO_3. Color scales between years are kept the same for parity, except for sulfate, due to its drastic reduction during the decade

5.3.2 Predicted Annual & seasonal pH

Figure 5.2 depicts the annual average pH fields over the US for 2001 and 2011 for $PM_{2.5}$, with the study domain of the Eastern US outlined. Simulations show that there are noticeable differences between the two years, localized mainly in desert regions along the US-Mexico border, Southern Texas and the Eastern US. The sulfate reductions in the Eastern US, appear to have a major impact on model results, leading to significant increases of aerosol pH in the area. For 2001, the average yearly pH for the Eastern US is 1.6, consistent with recent literature and observations from the WINTER campaign (Guo et al. 2015 & 2016, Weber et al. 2016) (Figure 5.2a). For 2011, however, predicted pH increases to about 2.5 – almost a unit higher (Figure 5.2b). This trend suggests that pH will keep increasing with future sulfate reductions, something that can lead to significant increases in predicted nitrate, as well as changes in SOA chemistry which heavily depends on acidic

aerosols (Xu et al. 2015, Pye et al. 2013, Surrat et al. 2010, Eddingsaas et al. 2010), especially in the SE US.

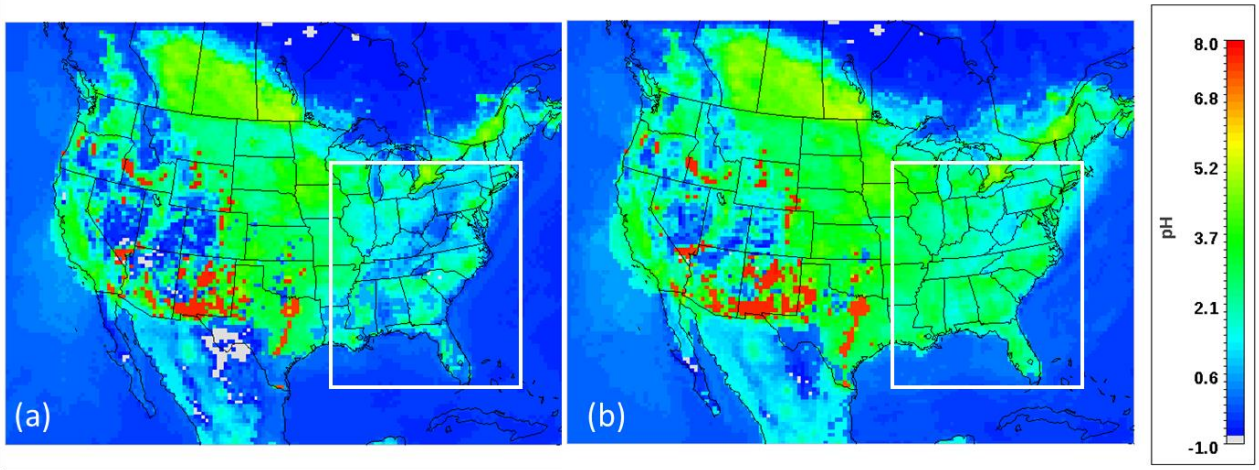

Figure 5.2 Annual averaged $PM_{2.5}$ pH over CONUS for (a) 2001 and (b) 2011, calculated offline using ISORROPIA, using the annual averaged CMAQ concentration fields. The white outline specifies the Eastern US domain used for further analysis.

Seasonal pH trends are also positive over the Eastern US, with the summertime (Figure 5.3f) experiencing stronger increases than in the winter (Figure 5.3c), being 0.5-1.5 for winter and 0.5-2 for summer. Much of the seasonal variability is driven by changes in temperature and relative humidity; increased relative humidity (RH) leads to less acidic aerosol, since liquid water content and pH are inversely related (Guo et al. 2015 & 2016), while increased temperatures promote low RH and therefore more acidic aerosol. The desert areas of the Western US, Southern Texas, Florida, SW Alabama and Mississippi are the most sensitive in the wintertime (Figure 5.3a, b), while the Central US is mostly unaffected. During the summer, the entire Central US is much more strongly impacted, while the wintertime sensitive areas exhibit only minor pH increases (Figure 5.3d, e).

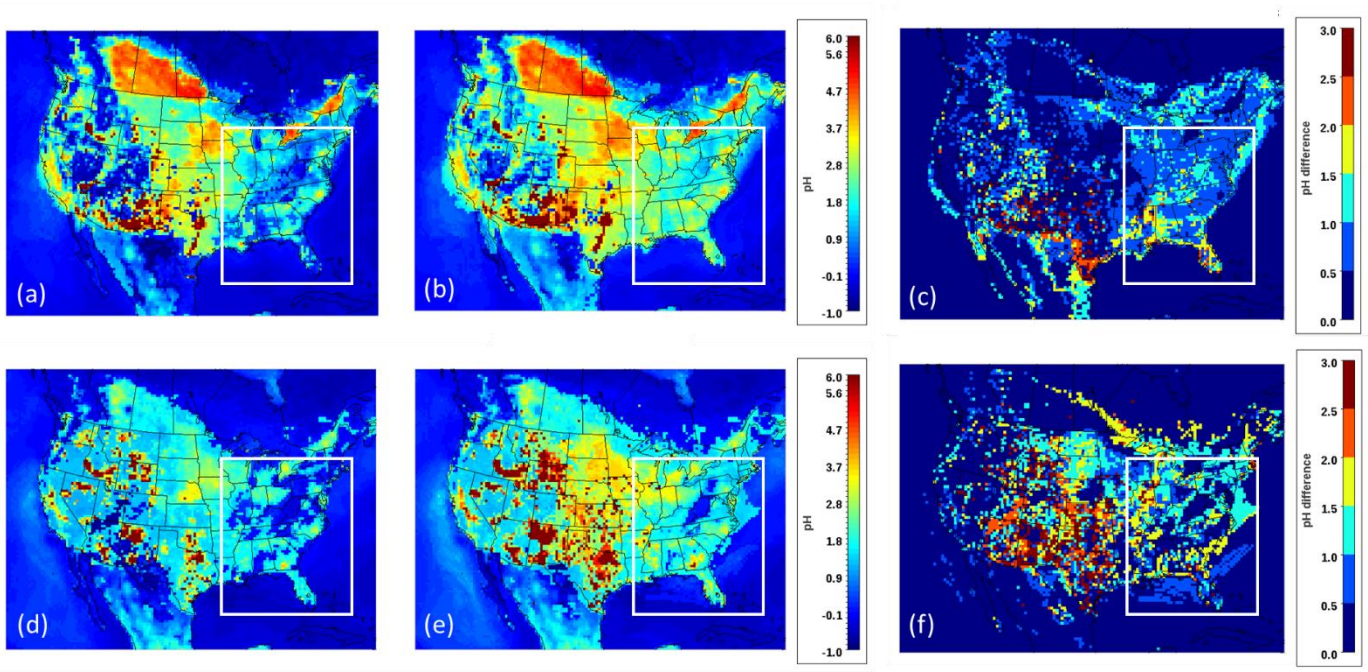

Figure 5.3 Seasonally averaged pH over CONUS for the winter (January) of (a) 2001, (b) 2011, the summer (July) of (d) 2001, (e) 2011. Panel (c) is difference between the simulation years for the winter, and (f) is the difference for the summer. As in Figure 3, the study domain is highlighted.

5.3.3 Model evaluation of pH

Model results for both simulation years were compared to thermodynamic analysis of measurements from three urban sites (Jefferson Street, JST; Georgia Tech, GT; Atlanta Road-Side, RS) and two rural (Yorkville, YRK; and Centerville CTR) SEARCH network sites (Guo et al. 2015). Measurements for the urban cites and the YRK site, were taken between May and December 2012 for the SCAPE study, while measurements from the CTR site were for the SOAS campaign period (June 1st to July 15th 2013) (Guo et al. 2015, Xu et al. 2015). The three urban sites are contained within the same CMAQ grid cell. All urban sites (Figure 5.4a, b, c, d), exhibit an early morning/late night pH maximum, and an afternoon minimum throughout the year (Guo et al. 2015). This a combination of two

factors; RH being highest during the early morning/late night, which increases water uptake and hence decreases acidity (Figure 5.5), and the presence of crustal elements in significant quantities during that time (Figure 5.6). The model pH closely tracks the diurnal profile of predicted cations (Figure 5.6), indicating that they have an important impact on predicted pH, which, however, is not seen in the measurements (Figure 5.7), since they make up a much smaller percentage of observed $PM_{2.5}$. Despite the presence of NVCs, the pH remains low for both simulation years but it tends to be higher in 2011, because of sulfate levels that are approximately half of those in 2001 across all sites, leading to the increased relative effect of NVCs (Weber et al. 2016). Removal of all NVCs from the thermodynamic calculations, allows the simulated diurnal profiles to better track the measurements. At the same time, a negative bias is introduced to the simulated pH, which is more prominent for the urban sites even after the sulfate reductions.

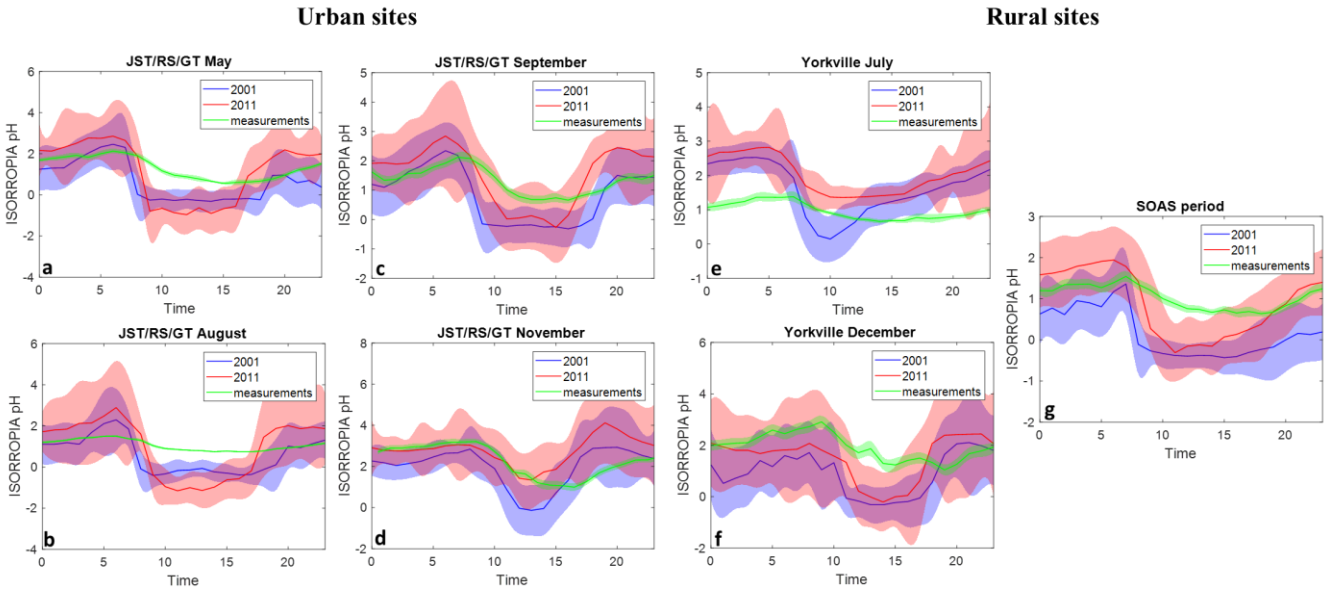

Figure 5.4 pH diurnal profiles for May (a), August (b), September (c) and November (d) at JST/RS/GT, July (e) and December (f) at YRK and for the SOAS campaign period (g). Blue and red lines are the CMAQ predicted pH for 2001 and 2011 respectively, while the shaded areas are one model standard deviation. The green line represents the pH calculated through the thermodynamic analysis of the measurements and the shaded area is standard

error. The plots are in different scales for each case given the large differences between each season and site.

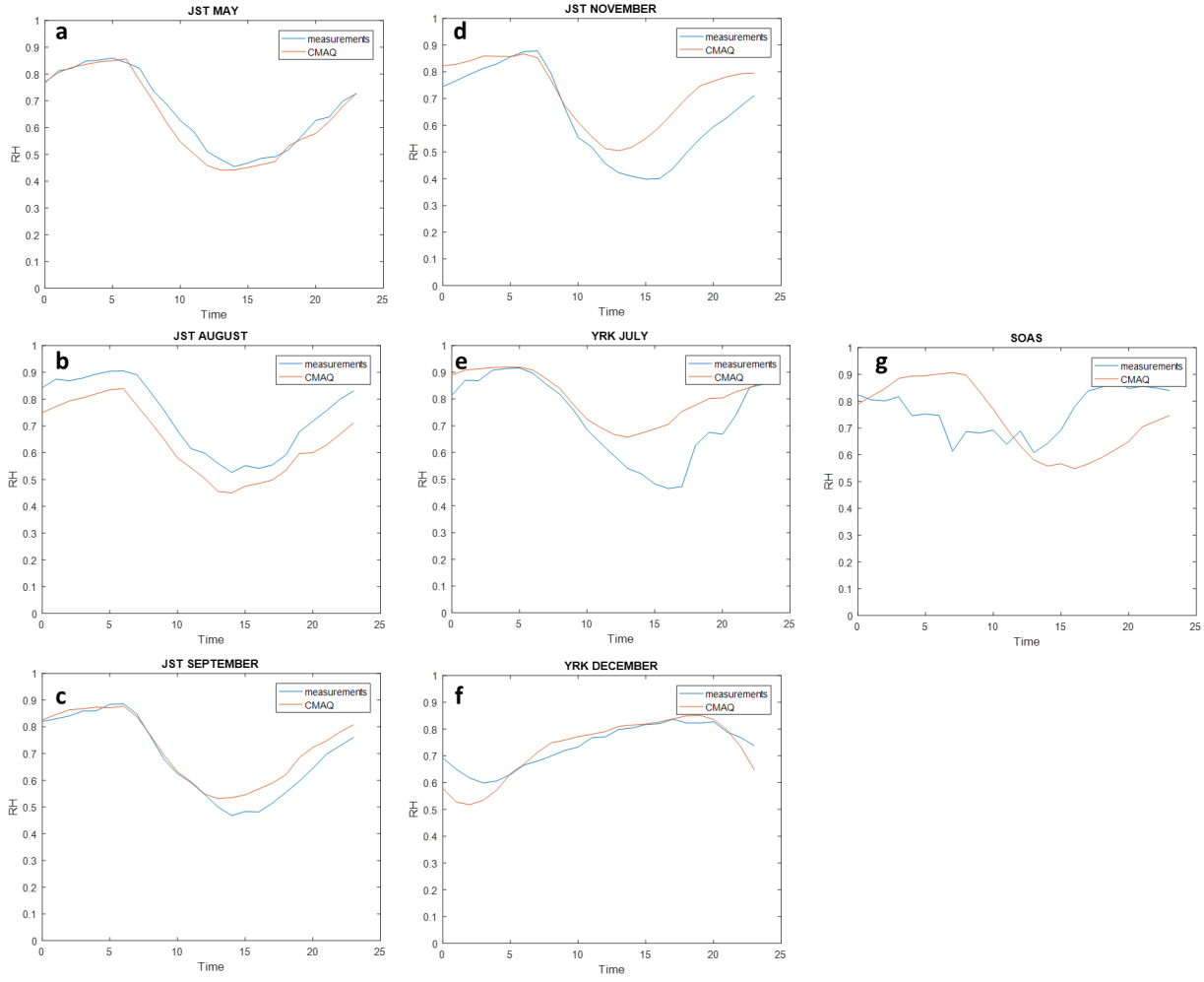

Figure 5.5 RH diurnal profiles for May (a), August (b), September (c) and November (d) at JST/RS/GT, July (e) and December (f) at YRK and for the SOAS campaign period (g). Blue line is the CMAQ predicted RH for 2001 and 2011, while the red line represents the measurements

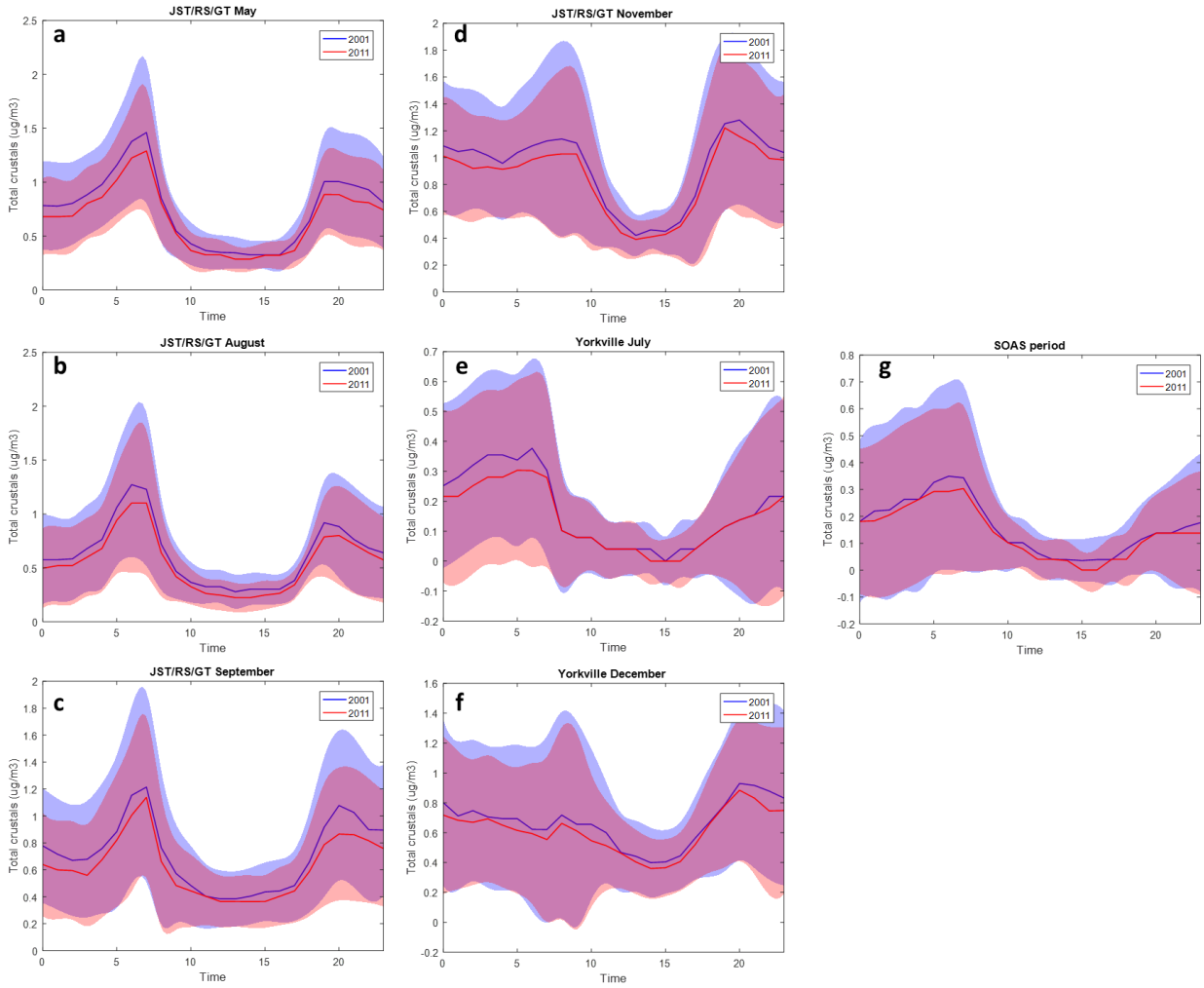

Figure 5.6 Total NVC diurnal profiles (Na^{+}, Ca^{+2}, K^{+} and Mg^{+2}) for May (a), August (b), September (c) and November (d) at JST/RS/GT, July (e) and December (f) at YRK and for the SOAS campaign period (g). Blue and red lines are the CMAQ predicted NVCs for 2001 and 2011 respectively, while the shaded areas are one model standard deviation.

The increase in pH is not proportional to the reduction in sulfate, since aerosol responds non-linearly to such reductions, through the volatilization of ammonia (Weber et al. 2016). Depending on location, sulfate reductions range from 38 to 55%, while the corresponding pH increase is much lower, pointing to the fact that cations, although small in amount, tend to have a disproportionately strong impact on acidity. For the SOAS campaign period

(Figure 5.4g), pH is underestimated especially for 2001. The biases follow the pattern of NVCs present, by being negatively biased until noon and positively biased for the rest of the day (Figure 5.6 and Figure 5.7). For the YRK site (Figure 5.4b, e), pH is overall underestimated during the winter and overestimated during the summer. Similarly to the urban sites, the predicted RH agrees well with the measurements (Figure 5.5), albeit with a positive afternoon bias during the summer. The diurnal profile of pH closely tracks the one of cations, further suggesting they may be directly related to the bias.

When evaluating the predicted pH trend for CTR, the model results exhibit a clear, increasing trend of 0.6 pH units per decade (Figure 5.7). This trend is inconsistent with recent thermodynamic analysis of observations suggesting a decrease in pH over the same time period for the SE US (Guo et al. 2015 & 2016, Weber et al. 2016). If this bias in predicted pH trend continues, it can have profound implications for future regulatory modeling, since the increased pH can lead to elevated levels of model nitrate, reproducing nitrate substitution (Bauer et al. 2007, Bellouin et al. 2011, Li et al. 2014, Goto et al. 2016). Possible reasons behind this pH bias could be overestimated ammonia emissions, underestimated sulfate, or, the presence of NVCs in $PM_{2.5}$.

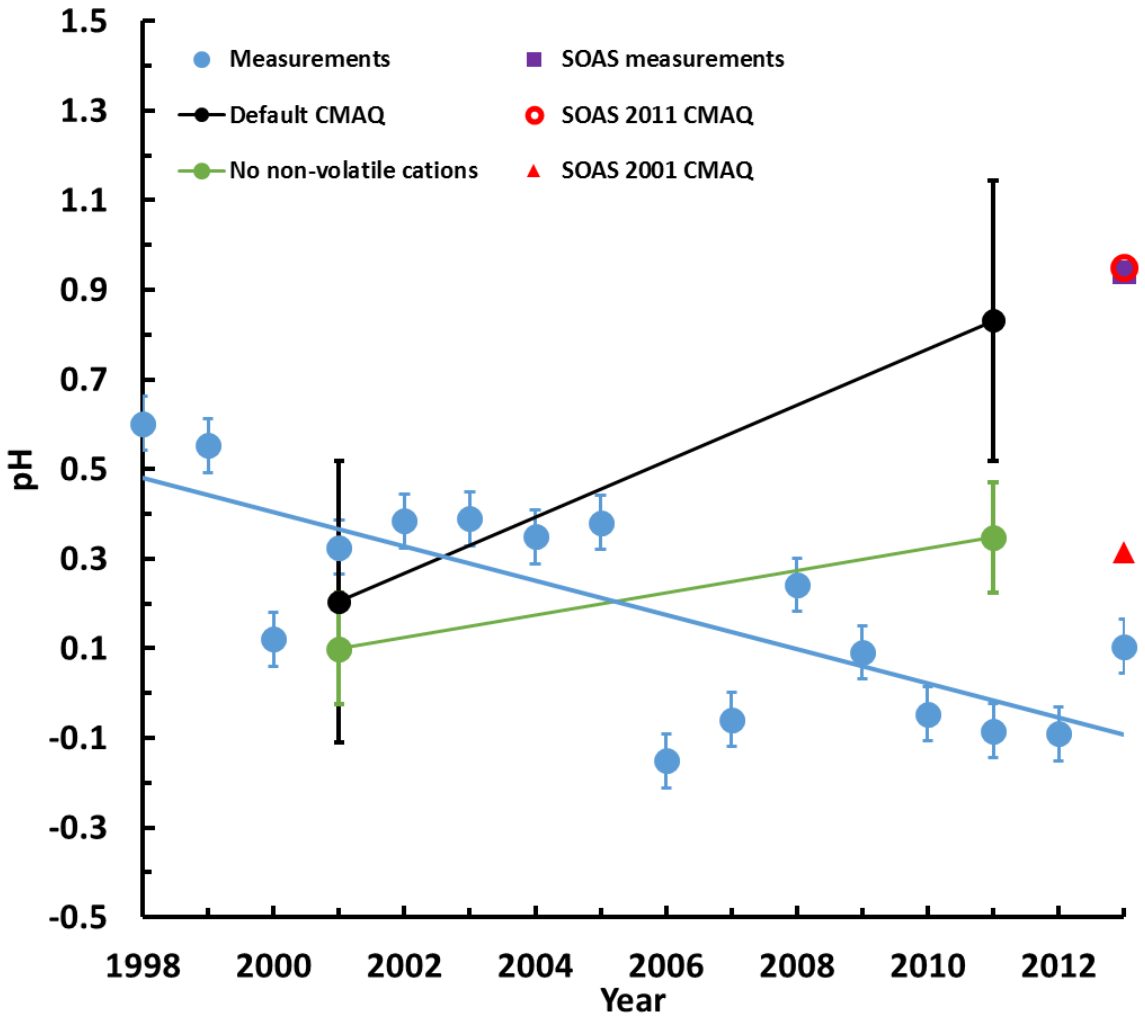

Figure 5.7 Decadal pH trends from the thermodynamic analysis of the measurements from Weber et al. 2016 (blue line), default CMAQ (black line) and CMAQ results without crustal elements (green line). Also shown, is the pH for the SOAS campaign, and for the CMAQ predicted pH for June 1st-July 15th 2001 and 2011. CMAQ exhibits a clear positive trend, with pH increasing throughout the decade, both due to sulfate reductions and the increasingly important role of NVCs. Standard error is also plotted for all data points.

The first two possibilities are unlikely, given the agreement of predicted ammonium and sulfate with previous studies (Park et al. 2006, Hand et al. 2012, Blanchard et al. 2013a, b, Kim et al. 2015, Saylor et al. 2015), and, the relative insensitivity of pH to ammonia and

sulfate (Weber et al. 2016, Silvern et al. 2017). However, NVCs, if inappropriately distributed in $PM_{2.5}$, can exert important biases on pH (Meskhidze et al. 2003, Karydis et al. 2016, Guo et al. 2017a, Foroutan et al. 2017). Indeed, offline calculations of aerosol pH excluding the influence of NVCs mitigates most of the predicted positive trend of 0.25 pH units per decade when all the aerosol species are considered (Figure 5.7), while also reducing standard error. The remaining bias may arise from errors in model RH, given that it controls water uptake and drives much of the diurnal variability in pH (Guo et al. 2015). However, usage of observed (instead of predicted) RH in the thermodynamic calculations, did not impact the predicted pH more than 0.1 units. A more thorough evaluation of the remainder of the pH bias, as well as the impact of NVCs when included in appropriate quantities, requires a far more extensive dataset than the one available at this study (Henneman et al., in review, Guo et al. 2017).

The pH bias becomes negative for most of the CMAQ Eastern US when removing all NVCs from the calculations (Figure 5.8). This, combined with the considerable model skill for sulfate, nitrate and ammonium when compared to literature (Henneman et al., in review) implies that pH biases are not related to errors in the major inorganic ions, but rather in the NVCs which are minor contributors to $PM_{2.5}$, hence poorly constrained. For the SEARCH sites NVCs comprise 5 to 10% of the total inorganic $PM_{2.5}$ (Guo et al. 2015), which is significantly less than what the model predicted values that are a factor of 4 higher than the measurements. The most important result therefore is that NVCs are a considerable source of pH prediction uncertainty when not accounted for correctly. It should be noted that for the summertime at the CTR location, the ammonium and sulfate values are biased

low in CMAQ by a factor of 3 using the Weber et al. 2016 data. These biases however are consistent with literature and typical of CTMs (Henneman et al, in review).

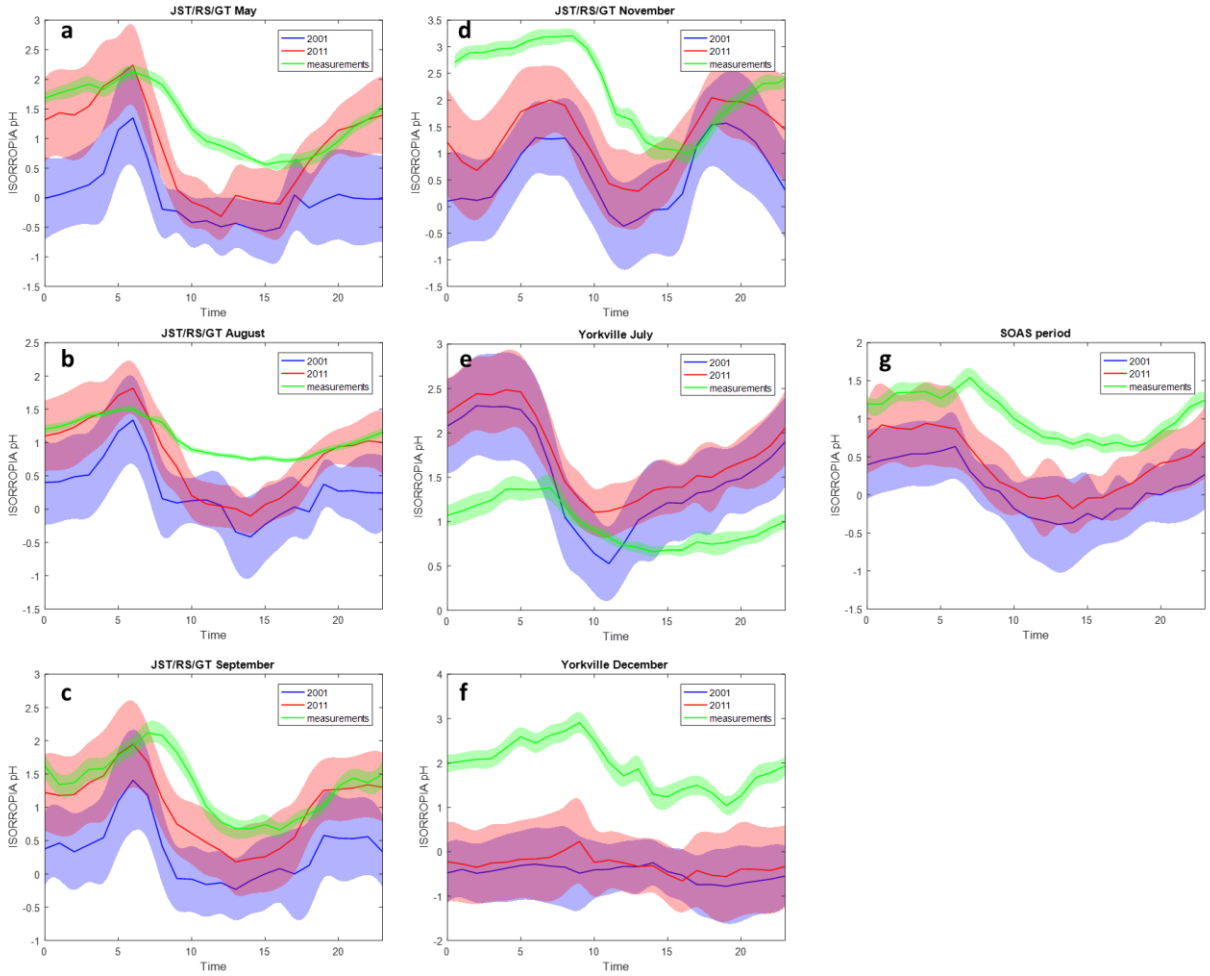

Figure 5.8 pH diurnal profiles when not accounting for NVCs, for May (a), August (b), September (c) and November (d) at JST/RS/GT, July (e) and December (f) at YRK and for the SOAS campaign period (g). Blue and red lines are the CMAQ predicted pH for 2001 and 2011 respectively, while the shaded areas are one model standard deviation. Green line represents the measurements and the shades area is standard error.

5.3.4 Organic acids and pH

The SEARCH sites have been thoroughly studied in previous literature (Guo et al, 2015 & 2017a, Xu et al. 2015, Weber et al. 2016), and given the high concentrations of organic mass observed throughout the year, they present an excellent case study for the potential impact of organics on pH. Recent studies indicate that organic aerosol can have an appreciable impact on aerosol pH, especially when allowed to interact with inorganics (Pye et al. 2018). Current models do not account for potential, non-ideal interactions between the two, in addition to not including organics in thermodynamic calculations, which, if the above statement is true, can lead to significant predictive pH errors.

To investigate the role of organics on pH we used the popular E-AIM model (Wexler & Clegg 2002, Friese & Ebel 2010, Clegg et al. 1992) on our model results for the SEARCH sites, which performs thermodynamic calculations to resolve the partitioning for mixtures of organics/inorganics. We tested a variety of organic compounds under different scenarios to determine the potential of organics to influence pH. More specifically, we assumed that a set amount (25 or 50% on a mole basis) of either oxalic, maleic, succinic or malonic acid already exists in the aerosol phase but is not accounted for. Given the constant reductions in sulfate, we also tested the potential of sulfate to be substituted by the same organics. To avoid the potential biases that NVCs can incur on simulations, all runs were conducted without them. E-AIM was run using the comprehensive Model IV configuration, in metastable mode. The baseline case that we used, was the average composition, temperature and RH across all sites.

When comparing the total aerosol partitioning (particle to gas) for each SEARCH site between ISORROPIA and E-AIM, they compare favorably, displaying an almost linear correlation between the two (Figure 5.9). For the low temperatures of December in Yorkville ($\overline{\overline{T}} \leq 10^{o}C$) E-AIM predicts a near complete absence of gas phase, in contrast to ISORROPIA, which is attributed to the difference of how the activity coefficients are calculated between the two models (Wexler & Clegg 2002, Friese & Ebel 2010, Clegg et al. 1992). Acidity between the two models is not well correlated, but both predict low values for pH for all sites (Figure 5.10).

Initially, an amount of 25 or 50% of additional oxalic acid on a mole basis was added to the baseline case, and then the pH was compared (Table 5.1). We find that for the cases presented in this study, addition of organic compounds to the model did not have a significant impact on acidity when compared to the baseline run, apart from the cases where RH was higher than 80% and the mole fraction of organic acids in the aqueous phase is greater than 25%. pH remains rather insensitive to the addition of oxalic acid for most cases, apart from the case that has the highest RH=0.8, and subsequently the highest amount of liquid water. For all other cases, most of oxalic acid partitions to the gas phase and its impact is negligible. Similarly, when other organic acids are tested against the baseline, under the same conditions (maleic, succinic, malonic), they incur a maximum 4% change on pH (Table 5.2).

For the substitution tests with oxalic acid, removal of sulfate from the system rapidly decreases the amount of total water in the particulate phase (Figure 5.10). This leads to the partitioning of organics to the gas phase (Figure 5.10), abating their impact on pH, since the relative composition on a mole fraction basis remains largely the same.

The above analysis demonstrates that, for the cases presented in this paper, organics do not have an appreciable impact on pH when only one liquid phase exists. Allowing more than one liquid phase of different compositions to form, can still potentially impact pH (Pye et al. 2018). We find that for the cases presented in this study, addition of organic compounds to the model, did not have a significant impact on acidity (≤2% pH deviation from the baseline value) compared to the baseline run, apart from the cases where RH was higher than 80% and the mole fraction of organic acids in the aqueous phase is greater than 25%.. However, E-AIM does not take into account multiple liquid phases in which organics could be the dominant species, and therefore in such cases organics could still play a major role on particle acidity (Pye et al. 2018).

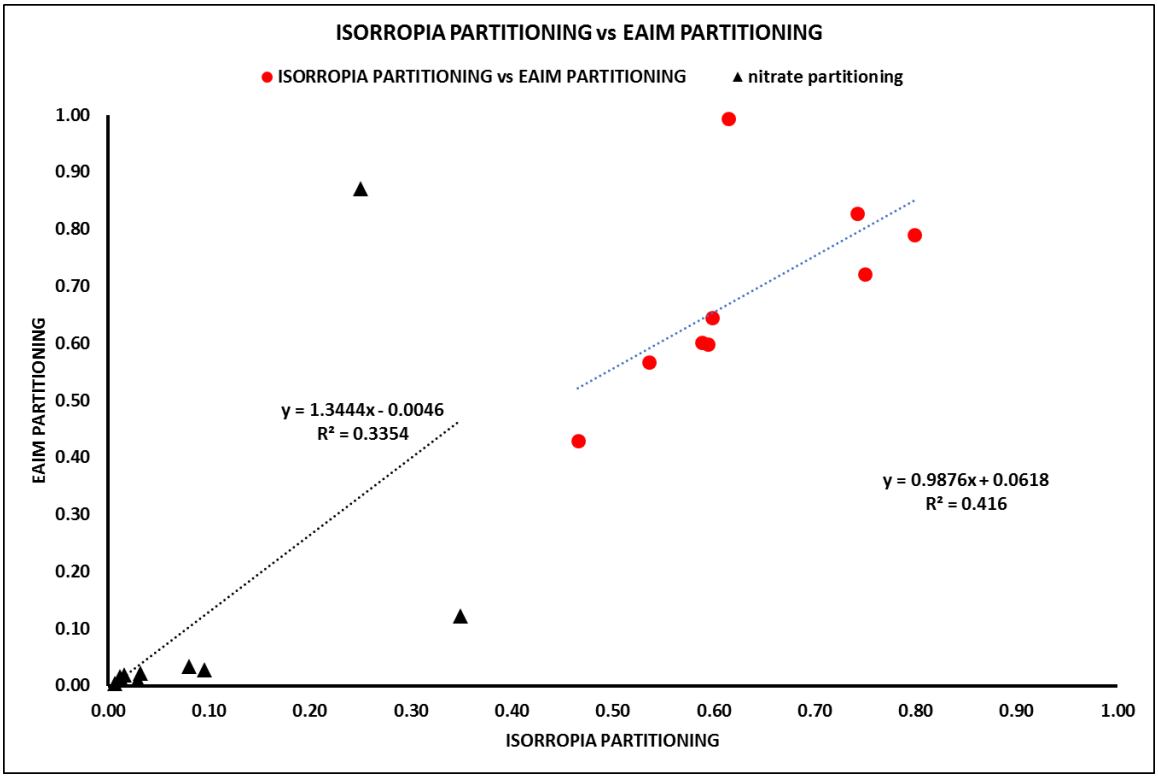

Figure 5.9 Nitrate (black) and total (red) particle-to-gas partitioning predicted between E-AIM and ISORROPIA.

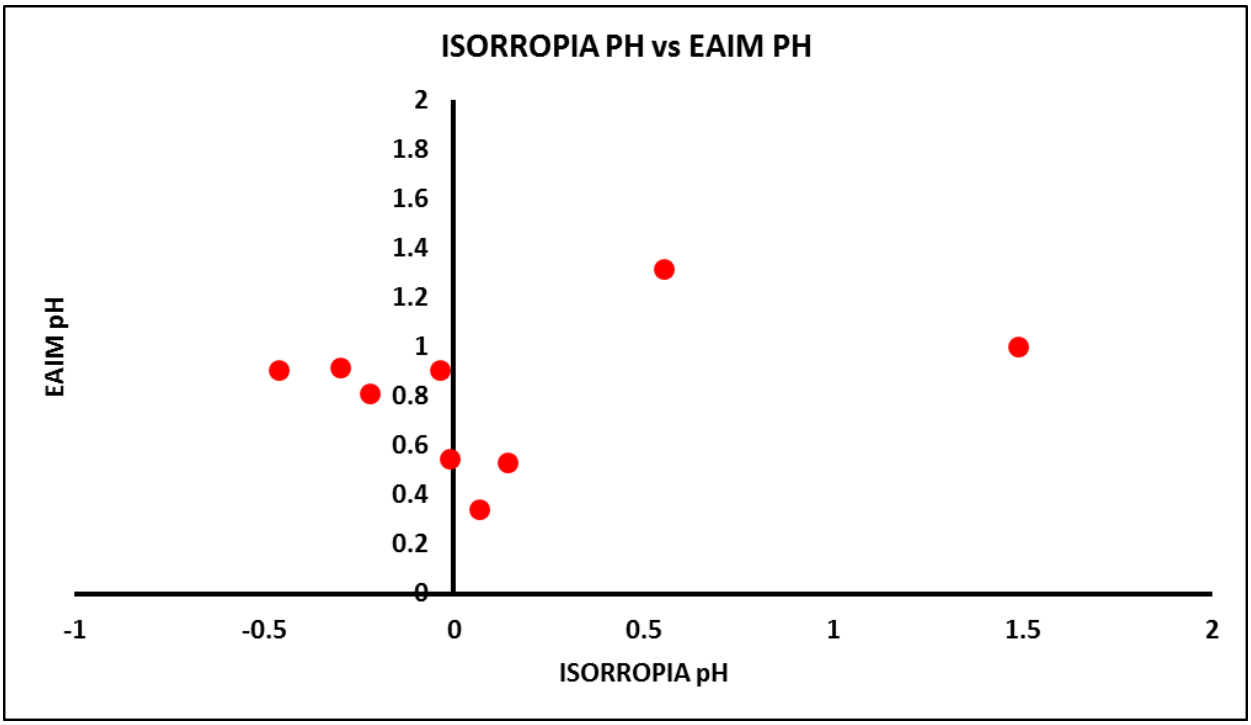

Figure 5.10 Comparison of predicted pH between E-AIM and ISORROPIA for all sites**.**

Table 5.1 ISORROPIA, E-AIM and E-AIM with an additional 25 and 50% oxalic acid predicted pH for all sites.

ISORROPIA PH	pH EAIM	pH 25% OXALIC	pH 50% OXALIC
-0.22	0.81	0.82	0.83
-0.30	0.92	0.92	0.91
0.55	1.31	1.32	1.25
-0.04	0.91	0.90	0.83
-0.01	0.55	0.55	0.55
0.07	0.34	0.34	0.34
0.14	0.53	0.53	0.52
-0.46	0.91	0.71	0.57
1.49	1.00	1.10	1.18

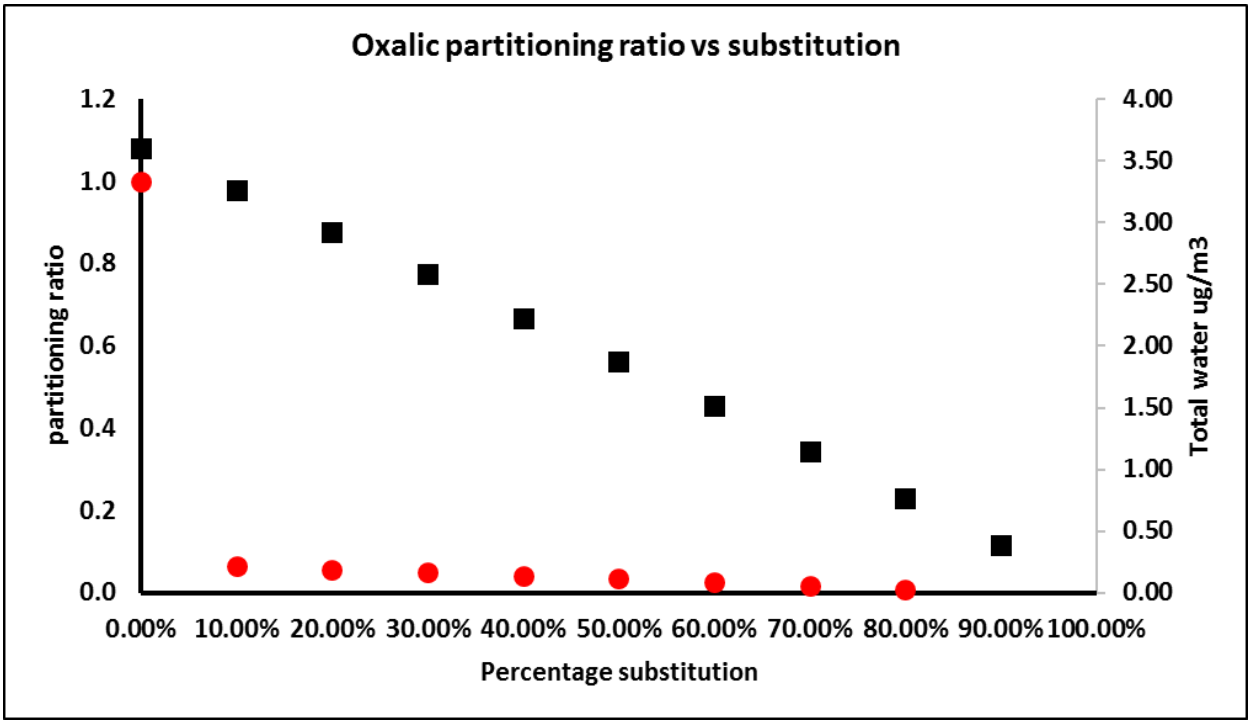

Figure 5.11 Comparison of predicted particle-to-gas partitioning of oxalic acid (red) and total water (black) between E-AIM and ISORROPIA as a function of sulfate substitution to oxalic acid.

Table 5.2 E-AIM predicted pH for the baseline case and for the cases with 25 and 50% addition of maleic, succinic or malonic acid.

Default pH EAIM	
0.809500489	
pH 25% MALEIC	**pH 50% MALEIC**
0.827689031	0.832387327
pH 25% SUCCINIC	**pH 50% SUCCINIC**
0.821886748	0.821886748
pH 25% MALONIC	**pH 50% MALONIC**
0.81276138	0.808548986

5.3.5 The impact of pH biases on nitrate partitioning and "sulfate substitution"

To understand the importance of pH biases on nitrate partitioning and the potential for predicting a behavior consistent with "nitrate substitution", we express the CMAQ output in each grid cell in terms of the nitrate partitioning ratio, $\varepsilon_{NO3} = \frac{[NO_3^-]}{[HNO_3]+[NO_3^-]}$. It can be shown that ε_{NO3} follows a simple sigmoidal curve (Meskhidze et al. 2013, Guo et al. 2016), $\varepsilon_{NO3} = 1 - \frac{[H^+]}{[H^+]+L\cdot T\cdot \Psi}$, where L is the liquid water content, T is ambient temperature , $[H^+]$ is the concentration of H^+ in the aerosol aqueous phase, and $\Psi = \frac{R\cdot[H_{NO_3}]}{1000\cdot P_0}$ is a constant that depends on the universal gas constant (R), the effective Henry's law constant for nitric acid in the aerosol aqueous phase (H_{NO3}) and the ambient pressure (P_0). Depending on the value of pH, nitrate partitioning in CMAQ can either be insensitive ($\frac{\partial \varepsilon_{NO3}}{\partial pH} \sim 0$) or sensitive

($\frac{\partial \varepsilon_{NO3}}{\partial pH} \sim 0.5$) to pH biases, depending on the month of the year considered (Figure 5.12). We generally find that nitrate partitioning is insensitive ($\frac{\partial \varepsilon_{NO3}}{\partial pH} \sim 0$) and heavily shifted to the gas phase (ε_{NO3} ~0) during the summer and spring (Figure 5.12), while it becomes quite sensitive to pH errors ($\frac{\partial \varepsilon_{NO3}}{\partial pH} \sim 0.5$) in the winter and fall. For the latter case, this means that small pH perturbations in either direction can strongly affect the amount of nitrate that partitions in the aerosol phase; if the weather is sufficiently cold and NO_x emissions and pH predictions are biased sufficiently high, ε_{NO3} ~1, meaning that all nitrates are partitioned to the aerosol phase and the emergence of "nitrate partitioning" behavior.

To exemplify the above, we determine the amount of excess nitrate from pH prediction biases as follows. Perturbing the acidity by ΔpH from the monthly mean value along the ε_{NO3} curves (Figure 5.12) gives the corresponding change in the partitioning ratio ($\Delta\varepsilon_{NO3}$).

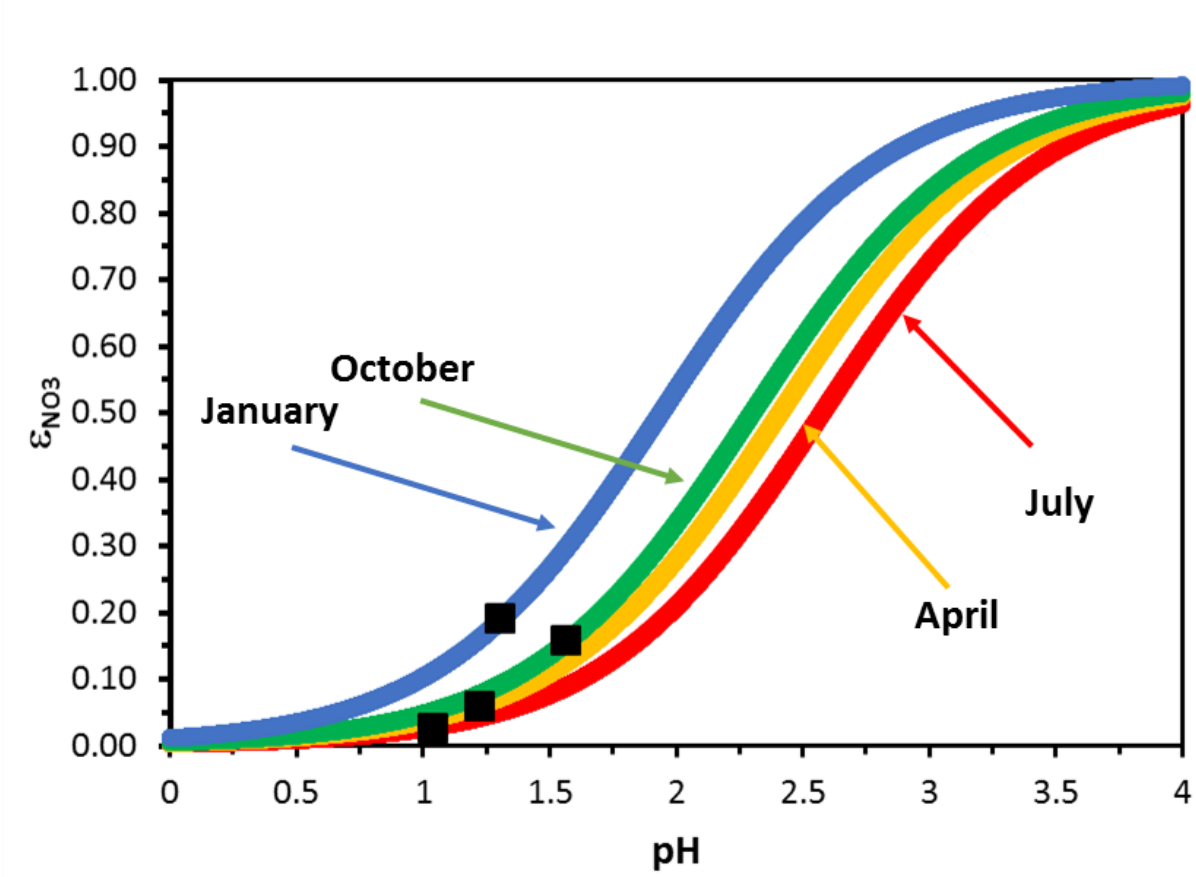

Figure 5.12 CMAQ-derived nitrate partitioning ratio for the E.US and select months of 2001. The black squares denote the average pH values for each month. Note the insensitivity of nitrate partitioning to pH biases in the summer for pH values of less than 1 ($\frac{\partial \varepsilon_{NO3}}{\partial pH} \sim \mathbf{0}$), which is not the case for colder months.

Multiplying $\Delta\varepsilon_{NO3}$ with the total nitrate ($HNO_{3(g)}$+NO_3) predicted in CMAQ in each grid cell gives the total nitrate response (ΔNO_3) to ΔpH. When applied to the Eastern US for ΔpH=+1 (the average pH impact of including NVCs in the $PM_{2.5}$ calculations over the entire Eastern US) gives the ΔNO_3 distributions shown in Figure 5 for the winter (Figure 5.13a) and the summer (Figure 5.13b).

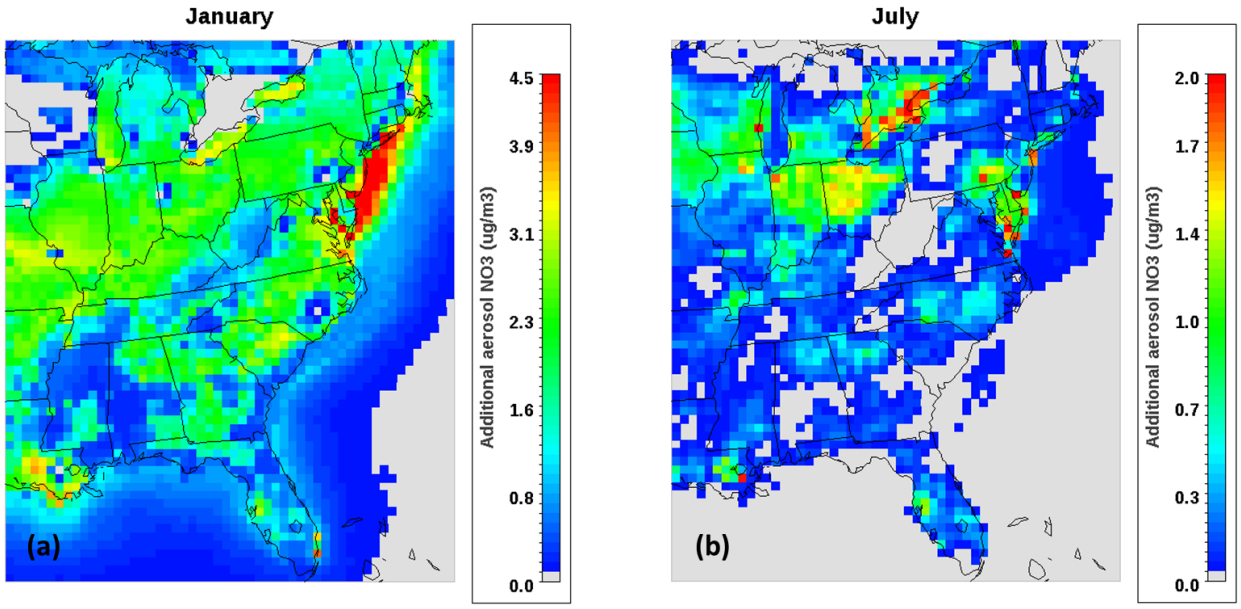

Figure 5.13 Increase in aerosol nitrate corresponding to a one-unit positive in pH for a) winter and b) summer. Emissions for 2011 are assumed, but to account for pH prediction biases from NVCs, they are removed from the thermodynamic calculations. Plots are on different scales due to the large differences in predicted nitrate increases.

The predicted wintertime nitrate bias tends to be higher than in the summer, owing to the lower temperatures and higher aerosol pH levels present (which shift ε_{NO3} towards higher values; Figure 5.12) and the higher values of total available nitrate in the wintertime. The combination of both factors (available nitrate and high pH) is necessary for appreciable quantities of nitrate to partition, but in general the locations with a pH of between 0.5 and 1 are the most susceptible to positive pH biases, since a unit increase places nitrate partitioning into the ascending part of the S-curve (Figure 5.12), rapidly increasing the amount of aerosol nitrate that can form. During both seasons, areas rich in total nitrate, and a pH between 0.5 and 1.5, such as the Ohio River Valley, New York, New Jersey and South Louisiana (Figure 5.2, 5.1e, f), exhibit the largest increases in aerosol nitrate. Other locations that have low pH, and low total nitrate such as West Virginia see minimal

changes. A notable exception is North Carolina which has a higher pH than the aforementioned locations - mainly due to the high NH_3 emissions from livestock - which pushes the partitioning beyond the sensitive regime, where increases in pH do not drive additional nitrate in the particle phase.

To investigate the potential of NVCs and sulfate reductions to induce nitrate substitution, the sensitivity of the nitrate increase ΔNO_3, to the corresponding sulfate reduction ΔSO_4, was quantified for the Eastern US, both when NVCs are included in the calculations and when they were not (Figure 5.14).

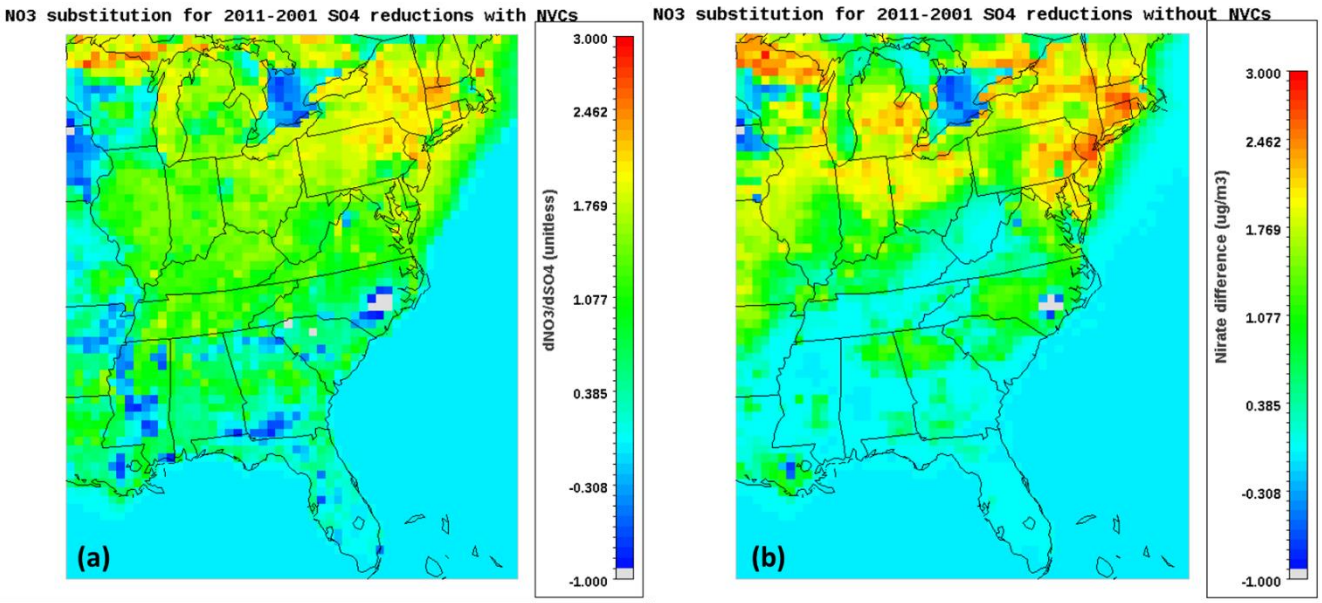

Figure 5.14 CMAQ predicted nitrate substitution ($\frac{NO_3^{2011}-NO_3^{2001}}{SO_4^{2001}-SO_4^{2011}}$) over the decade, when NVCs are accounted for (a), and when they are removed from the thermodynamic calculations (b).

Over the decade, nitrate has seen increases in the Eastern US (Figure 5.15) ranging from 0.5 to 2.5 μg m^{-3}, and NVCs can have a profound impact on how these increases are

distributed across the domain (Figure 5.15a, b). In the presence of NVCs (Figure 5.14a), there is a 1 μg m^{-3} increase of nitrate for a sulfate reduction of the same value over the Eastern US.

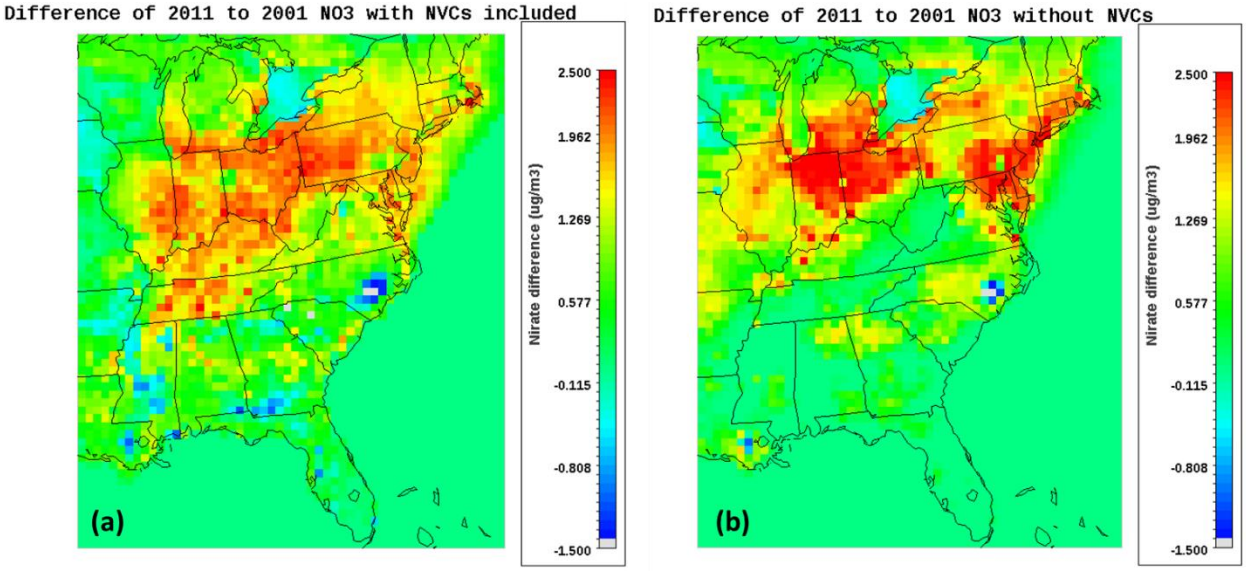

Figure 5.15 Difference in predicted nitrate over the Eastern US between 2011 and 2001 when NVCs are included in calculations (a), and when they are excluded (b).

For this case, substitution is predicted across the entire Eastern US, with only a few gridcells in South Georgia, Mississippi and North Carolina exhibiting the opposite trend (nitrate reduction), attributed to the formation of insoluble $CaSO_4$, which reduces the availability of aerosol water, and in turn inhibits the formation of NO_3 with the co-condensation of NH_3. When NVCs are removed (Figure 5.14b), the corresponding nitrate increase is much less (0-0.2 μg m^{-3} per 1 μg m^{-3} of sulfate), especially in the Eastern US, while substitution is still predicted in the Northern parts of the domain such as Ohio, Indiana and Michigan. The aforementioned areas, tend to have higher seasonal pH values than the SE US (Figure 5.2), and the removal of NVCs reduces the pH to values where

nitrate partitioning is more sensitive to small pH perturbations (Figure 5.12), leading to a higher predicted sensitivity to sulfate reductions. This analysis suggests that nitrate substitution is of a much smaller magnitude than expected (West et al. 1999, Heald et al. 2012, Bauer et al. 2007, Bellouin et al. 2011, Li et al. 2011, Goto et al. 2016, Vayenas et al. 2005, Karydis et al. 2016), and heavily impacted by pH biases introduced from NVCs.

Given the importance of aerosol acidity for almost any aerosol-related process and impact, it is imperative that aerosol studies evaluate acidity inferred from thermodynamic analysis of ambient data as presented here. We demonstrate that in the case of nitrate substitution, the distribution of nonvolatile cations over particle size can have a profound impact on model behavior, and requires better constraints from emissions to observations (or at least appropriate sensitivity studies, such as those carried out here, to unravel the potential impact of nonvolatile cations). Understanding aerosol pH and the drivers thereof, is a powerful tool for evaluating model performance that has never been used before. Usage of molar ratios, ion balances and other conceptual models of aerosol acidity (Hennigan et al. 2015, Wang et al. 2016, Silvern et al. 2017) provide limited insights in aerosol pH and should be strongly avoided to limit incorrect conclusions.

CHAPTER 6

FUTURE RESEARCH DIRECTIONS

On a microphysics scale, this thesis investigated the impact of radioactive charging on the lifetime of radioactive aerosol populations, as well as, the linkage between energy sector emissions and air quality on a regional scale, with specific chapters focusing on the impact of specific Phillips 66 operations and potential expansions, secondary aerosol formation, and the dynamics of aerosol pH. While many updates were implemented in CMAQ and TOMAS, there still exists significant room for improvement if important scientific questions for the future of air quality are to be answered.

6.1 Transport of radioactive aerosol and the physics of charged populations

The TOMAS-RC model that was developed in this thesis, presents an ideal starting point to study the physics of radioactive aerosols. However, this version only resolves charged coagulation, and other processes that could potentially be affected by charging, such as condensation/evaporation and nucleation, are not taken into account. Future experimental research should focus on elucidating the mechanisms that are underlying to these processes, as to allow for better model representation of the physics and subsequently more accurate predictions of dispersion patterns of fallout.

Many other families of atmospheric particles also become charged in the atmosphere, albeit through different charging mechanisms. A prominent type of aerosol

that is known to carry significant charge is volcanic ash, which becomes charged through frictional forces (Langmann 2013). Eruptions can be catastrophic events, not only short-term in the immediate vicinity, but also long-term since volcanic ash is launched high into the troposphere and can travel great distances, affecting air quality and causing disruptions in flight routes, as it was the case after the Eyjafjallajokull in 2010, when the cloud from the eruption covered a significant part of the Northern hemisphere for months. Such events, although rare, have profound effects on short term climate and air quality, and therefore accurate modelling of the physics is necessary to minimize their impact on human activities.

6.2 SOA production and minimizing model uncertainties

Although great progress has been made in expanding the model chemistry in recent years, many biases still exist that prevent closure of organic mass between model and observations. There is an abundance of literature studies with regards to SOA production yields for BVOCs, but they are mostly derived through chamber data from experiments often done in conditions that are not representative of ambient concentrations. Fields campaigns such as SOAS, provide a wealth of data that can be used to better constrain experimentally derived chemical mechanisms and improve model accuracy. In the future, experiments using outdoor chambers with atmospherically realistic conditions (temperature, RH etc.) could be designed to study the formation of SOA as it occurs in ambient conditions.

Chemical mechanisms designed for model use such as the popular cb05 and saprc often lump many species together to minimize the number of reactions that the model has to resolve in order to increase computational speed. This is also a source of bias, since it

limits model species to the order of hundreds; one of these model species could be representative of a few thousands of atmospheric species. Since more and more species and production pathways are discovered every year, these mechanisms should be updated in a way that allows for better accuracy, while still retaining the computational speed they offer.

6.3 Aerosol pH as a proxy for model evaluation

Models are currently not evaluated for their ability to accurately predict pH, and since it can play an important role in the formation of regulatory-important species such as nitrate and SOA, future work should be aimed at addressing pH predictive biases in CTMs. To that end, the correct attribution of NVCs in the appropriate aerosol modes in CMAQ needs to be resolved, allowing model predicted pH to be used as a proxy for model accuracy, along with other established metrics.

Given the importance of aerosol pH in solubilizing ecosystem nutrients (Myriokefalitakis et al. 2016) it can be used as a tool to study the interactions between plumes of anthropogenic pollutants and mineral dust in a coupled ocean-atmosphere model, especially over the Atlantic where dust and pollutant plumes from 3 continents interact. Preliminary work in this subject (Stockdale et al, 2016, Myriokefalitakis et al. 2016, Li et al. 2017), underscores the importance of dust acidification in providing phytoplankton with sufficient phosphorus.

Another consideration would be the quantification of the impact of organics on aerosol acidity. While under the current atmospheric conditions, they do not appear to play an important role in modulating pH, the constant reductions in sulfate could potentially

turn organics into major players that control pH. The popular model ISORROPIA could also be updated in the future in order to include organics in thermodynamic calculations, since it is the to-go model for the current state-of-the-art global and regional models.

Finally, although a link between some particulate species and human health has already been established, the role that pH has not yet been elucidated. The oxidative potential of some acid-soluble, transition metals has been studied (Fang et al. 2017), but the potential of acidic particles to have health effects remains unknown. Future studies could focus on determining the impact that low pH particles can have on the respiratory tract *in vivo* since the high concentrations of hydronium ions could render cellular membranes permeable to foreign substances with adverse health effects.

REFERENCES

Acosta, J.P., A Model Study of the Global Emissions of Terpenoid Volatile Organic Compounds from Terrestrial Vegetation in the Last Millennium, *Master Thesis*, Institute of Physics of Helsinki, 2013

Adams, P. J., and J. H. Seinfeld, Predicting global aerosol size distributions in general circulation models, J. Geophys. Res., 107(D19), 4370, doi,10.1029/2001JD001010, 2002.Adeyini, M. O. and Oladiran, E. O. Recent results on atmospheric radioactivity at Ibadan, Nigeria, *Radiation Measurements*, 41, 330-336, doi, 10.1016/j.radmeas.2005.07.028, 2006

Air Pollutant Emissions Trends Data, https ://www.epa.gov/air-emissions-inventories/air-pollutant-emissions-trends-data

Allen, H. M., Draper, D. C., Ayres, B. R., Ault, A., Bondy, A., Takahama, S., Modini, R. L., Baumann, K., Edgerton, E., and Knote, C., Influence of crustal dust and sea spray supermicron particle concentrations and acidity on inorganic NO 3− aerosol during the 2013 Southern Oxidant and Aerosol Study, *Atmospheric Chemistry and Physics*, 15, 10669-10685, 2015.

Arimoto, R., Webb, J. L., Conley, M., Radioactive contamination of atmospheric dust over Southwestern New Mexico, *Atmospheric Environ.* 2005, 39, 4745

Bauer, S. E., Koch, D., Unger, N., Metzger, S. M., Shindell, D. T., and Streets, D. G., Nitrate aerosols today and in 2030, a global simulation including aerosols and tropospheric ozone, *Atmos. Chem. Phys.*, 7, 5043-5059, doi,10.5194/acp-7-5043-2007, 2007

Bellouin, N., J. Rae, A. Jones, C. Johnson, J. Haywood, and O. Boucher (2011), Aerosol forcing in the Climate Model Intercomparison Project (CMIP5) simulations by HadGEM2-ES and the role of ammonium nitrate, *J. Geophys. Res.*, 116,D20206, doi,10.1029/2011JD016074

Blanchard, C.L., Hidy, G.M., Tanenbaum, S., Edgerton, E.S. and Hartsell, B.E., The Southeastern Aerosol Research and Characterization (SEARCH) study, Temporal trends in gas and PM concentrations and composition, 1999-2010. J. *Air Waste Manage. Assoc*., 63,247-259, doi,10.1080/10962247.2012.748523, 2013a

Blanchard, C.L., Hidy, G.M., Tanenbaum, S., Edgerton, E.S. and Hartsell, B.E. 2013b. The Southeastern Aerosol Research and Characterization (SEARCH) study, Spatial variations and chemical climatology, 1999-2010. J. *Air Waste Manage. Assoc*., 63,260-275.

Bougiatioti, A., Nikolaou, P., Stavroulas, I., Kouvarakis, G., Weber, R., Nenes, A., Kanakidou, M., and Mihalopoulos, N., Particle water and pH in the eastern Mediterranean, source variability and implications for nutrient availability, *Atmos. Chem. Phys*., 16, 4579-4591, doi,10.5194/acp-16-4579-2016, 2016

Brophy, P., and Farmer, D., A switchable reagent ion high resolution time-of-flight chemical ionization mass spectrometer for real-time measurement of gas phase oxidized species, characterization from the 2013 southern oxidant and aerosol study, *Atmospheric Measurement Techniques*, 8, 2945-2959, 2015.

Budisulistiorini, S. H., Li, X., Bairai, S. T., Renfro, J., Liu, Y., Liu, Y. J., McKinney, K. A., Martin, S. T., McNeill, V. F., Pye, H. O. T., Nenes, A., Neff, M. E., Stone, E. A., Mueller, S., Knote, C., Shaw, S. L., Zhang, Z., Gold, A., and Surratt, J. D.,

Examining the effects of anthropogenic emissions on isoprene-derived secondary organic aerosol formation during the 2013 Southern Oxidant and Aerosol Study (SOAS) at the Look Rock, Tennessee ground site, *Atmos. Chem. Phys.*, 15, 8871-8888, doi,10.5194/acp-15-8871-2015, 2015

Budisulistiorini, S. H., Nenes, A., Carlton, A.G, McNeill, V. F., Pye, H. O., Surratt, J. D, Simulating Aqueous-Phase Isoprene-Epoxydiol (IEPOX) Secondary Organic Aerosol Production During the 2013 Southern Oxidant and Aerosol Study (SOAS), *Environmental Science & Technology*, 51 (9), 5026-5034, doi, 10.1021/acs.est.6b05750, 2017

Byun, D. W., and K. L. Schere, 2006, Review of the governing equations, computational algorithms, and other components of the Models-3 Community Multiscale Air Quality (CMAQ) Modeling System. *Appl. Mech. Rev.*, 59, 51-77.

Carlton, A. G., Baker, K. R., Photochemical Modeling of the Ozark Isoprene Volcano: MEGAN, BEIS, and Their Impacts on Air Quality Predictions, *Environmental Science & Technology* 45 (10), 4438-4445, DOI: 10.1021/es200050x, 2011

Carlton A.G., Goldstein A., Jimenez J.F., The Southern Oxidant and Aerosol Study (SOAS), Measuring and modeling at the interface of air quality and climate change to understand biosphere-atmosphere interactions, *SOAS White Paper*, 2013

Cerully, K., Hite, J., McLaughlin, M., and Nenes., A., Toward the Determination of Joint Volatility-Hygroscopicity Distributions, Development and Response Characterization for Single-Component Aerosol, *Aer.Sci.Tech.*, 48, doi,10.1080/02786826.2013.870326, 2014

Chan, M. N., Surratt, J. D., Claeys, M., Edgerton, E. S., Tanner, R. L., Shaw, S. L., Zheng, M., Knipping, E. M., Eddingsaas, N. C., Wennberg, P. O., Seinfeld, J. H. Characterization and quantification of isoprene-derived epoxydiols in ambient aerosol in the southeastern United States. *Environ. Sci. Technol*. 2010, 44, 4590−4596

Chesser, R.K., Bondarkov, M., Baker, R.J., Wickliffe,J.K., Rodgers, B.E., Reconstruction of radioactive plume characteristics along Chernobyl's Western trace, *J. Environ. Radioactivity*, 71, 147-157, doi,10.1016/S0265-931X(03)00165-6, 2004

Christoudias, T., Proestos, Y., and Lelieveld, J., Global risk from the atmospheric dispersion of radionuclides by nuclear power plant accidents in the coming decades, *Atmos. Chem. Phys*. Discuss., 2013, 13, 30287-30309, doi,10.5194/acpd-13-30287-2013

Clegg, S. L., Pitzer, K. S., and Brimblecombe, P., Thermodynamics of multicomponent, miscible, ionic solutions. II. Mixtures including unsymmetrical electrolytes. *J. Phys. Chem*. 96, 9470-9479, DOI, 10.1021/j100202a074, 1992

Clement, C.F., Clement, R.A., Harrison, R.G. Charge Distributions and Coagulation of Radioactive Aerosols. *J. Aerosol Sci*, 26, 1207-1225, doi, 10.1016/0021-8502(95)00525-0, 1995

Clement, C.F., Harrison, R.G. The Charging of Radioactive Aerosols. *J. Aerosol Sci*., 23, 481-504, doi, 10.1016/0021-8502(92)90019-R, 1992

Cohan, D. S, Hakami, A., Hu Y. and Russell, A.G., Nonlinear Response of Ozone to Emissions, Source Apportionment and Sensitivity Analysis, *Environmental Science & Technology*, 39 (17), 6739-6748 doi, 10.1021/es048664m, 2005

Eddingsaas, N. C., VanderVelde, D. G., Wennberg, P. O. Kinetics and products of the acid-catalyzed ring-opening of atmospherically relevant butyl epoxy alcohols. *J. Phys. Chem*. A 2010, 114, 8106−8113.

Edgerton, E. S., Hartsell, B. E., Saylor, R. D., Jansen, J. J., Hansen, D. A., and Hidy, G. M., The Southeastern Aerosol Research and Characterization Study, Part II. Filter-based measurements of fine and coarse particulate matter mass and composition, *Journal of the Air & Waste Management Association*, 55, 1527-1542, 2005.

Edgerton, E. S., Hartsell, B. E., Saylor, R. D., Jansen, J. J., Hansen, D. A., and Hidy, G. M., The Southeastern Aerosol Research and Characterization Study, part 3, Continuous measurements of fine particulate matter mass and composition, *Journal of the Air & Waste Management Association*, 56, 1325-1341, 2006.

Fang, T., Guo, H., Zeng, L., Verma, V., Nenes, A., Weber, R.J. (2017) Highly acidic ambient particles, soluble metals and oxidative potential, A link between sulfate and aerosol toxicity, *Env.Sci.Tech*., 51 (5), pp 2611–2620, doi,10.1021/acs.est.6b06151

Farina, S. C., P. J. Adams, and S. N. Pandis, Modeling global secondary organic aerosol formation and processing with the volatility basis set, Implications for anthropogenic secondary organic aerosol, *J. Geophys. Res*., 115, D09202, doi,10.1029/2009JD013046, 2010

Fisher, J.A., D.J. Jacob, Q. Wang, R. Bahreini, C.C. Carouge, M.J. Cubison, J.E. Dibb, T. Diehl, J.L. Jimenez, E.M. Leibensperger, Z. Lu, M.B.J. Meinders, H.O.T. Pye, P.K. Quinn,

S. Sharma, D.G. Streets, A. van Donkelaar, and R.M. Yantosca. 2011. "Sources, distribution, and acidity of sulfate-ammonium aerosol in the Arctic in winter-spring." *Atmospheric Environment* 45, 7301-7318.

Foroutan, H., J. Young, S. Napelenok, L. Ran, K. W. Appel, R. C. Gilliam, and J. E. Pleim (2017), Development and evaluation of a physics-based windblown dust emission scheme implemented in the CMAQ modeling system, *J. Adv. Model. Earth Syst*., 9, 585–608, doi,10.1002/2016MS000823.

Fountoukis, C. and Nenes, A, ISORROPIA II, A Computationally Efficient Aerosol Thermodynamic Equilibrium Model for K+, Ca2+, Mg2+, NH4+, Na+, SO42-, NO3-, Cl-, H2O Aerosols, *Atmos.Chem.Phys*., 7, 4639–4659, doi, 10.5194/acp-7-4639-2007, 2007

Friese, E. and Ebel, A., Temperature dependent thermodynamic model of the system H+ - NH4+ - Na+ - SO42− - NO3− - Cl− - H2O. *J. Phys. Chem.* A, 114, 11595-11631, DOI, 10.1021/jp101041j, 2010

Fuchs, N.A. The Mechanics of Aerosols, *Pergamon Press*, New York, 1964

Gensdarmes, F., Boulaud, D., Renoux, A. Electrical Charging of Radioactive Aerosols—Comparison of the Clement–Harrison Models with New Experiments. *J. Aerosol Sci*., 32, 1437-1458, doi, 10.1016/S0021-8502(01)00065-9, 2001

Ghio, A. J., Carraway, M. S. & Madden, M. C. Composition of air pollution particles and oxidative stress in cells, tissues, and living systems. *J. Toxicol. Environ. Health* B 15, 1–21 (2012).

Goto, D., Ueda, K., Ng, C.F.S., Takami, A., Ariga, T., Matsuhashi, K., Nakajima, T., Estimation of excess mortality due to long-term exposure to PM2.5 in Japan using a high-resolution model for present and future scenarios. *Atmospheric Environment* 2016,140,320–332. doi,10.1016/j.atmosenv.2016.06.015

Greenfield, S. M., Ionization of radioactive particles in the free air. *J. Geophys. Res*., 61, 27-33, doi,10.1029/JZ061i001p00027, 1956

Greenfield, S. M., Rain scavenging of radioactive particulate matter from the atmosphere. *J. Atmos. Sci*., 14, 115-125, doi, 10.1175/1520-0469(1957)014<0115,RSORPM>2.0.CO,2, 1957

Goldstein, A.H., et al., Biogenic carbon and anthropogenic pollutants combine to forma cooling

haze over the southeastern United States. *Proceedings of the National Academy of Scienc es of*

the United States of America, 2009. 106(22), p. 8835-8840

Guenther, A., Karl, T., Harley, P., Wiedinmyer, C., Palmer, P. I., Geron, C. Estimates of global terrestrial isoprene emissions using MEGAN (Model of Emissions of Gases and Aerosols from Nature). *Atmos. Chem. Phys*. 2006, 6, 3181−3210.

Gunn, R., Diffusion charging of atmospheric droplets by ions, and the resulting combination coefficients. *J. Meteor*., 11, 329, 339-347 doi, 10.1175/1520-0469(1954)011<0339,DCOADB>2.0.CO,2, 1954

Guo, H., Xu, L., Bougiatioti, A., Cerully, K. M., Capps, S. L., Hite Jr., J. R., Carlton, A. G., Lee, S.-H., Bergin, M. H., Ng, N. L., Nenes, A., and Weber, R. J., Fine-particle water and pH in the southeastern United States, *Atmos. Chem. Phys*., 15, 5211-5228, doi,10.5194/acp-15-5211-2015, 2015.

Guo, H., Sullivan, A.P., Campuzano-Jost, P., Schroder, J.C., Lopez-Hilfiger, F.D., Dibb, J.E., Jimenez, J.L., Thornton, J.A, Brown, S.S., Nenes, A., and Weber, R.J., Fine particle pH and the partitioning of nitric acid during winter in the northeastern United States, *J.Geoph.Res*., 121, doi,10.1002/2016JD025311, 2016

Guo, H., Weber, R.J., Nenes, A. (2017a) The sensitivity of particle pH to NH3, Can high NH3 cause London Fog conditions?, *Sci.Rep*., 7, 12109, doi,10.1038/s41598-017-11704-0

Guo, H., Liu, J., Froyd, K. D., Roberts, J. M., Veres, P. R., Hayes, P. L., Jimenez, J. L., Nenes, A., and Weber, R. J., Fine particle pH and gas–particle phase partitioning of inorganic species in Pasadena, California, during the 2010 CalNex campaign, *Atmos. Chem. Phys*., 17, 5703-5719, doi,10.5194/acp-17-5703-2017, 2017.

Guo, H., Nenes, A., and Weber, R. J., The underappreciated role of nonvolatile cations on aerosol ammonium-sulfate molar ratios, *Atmos. Chem. Phys. Discuss*., https,//doi.org/10.5194/acp-2017-737, in review, 2017

Haagen-Smit, A. J. & Fox, M. M. Photochemical Ozone, Formation with Hydrocarbons and Automobile Exhaust, *Air Repair*, 4,3, 105-136, DOI, 10.1080/00966665.1954.10467649, 1954

Hand, J. L., Schichtel, B. A., Malm, W. C., and Pitchford, M. L., Particulate sulfate ion concentration and SO2 emission trends in the United States from the early 1990s through 2010, *Atmos. Chem. Phys*., 12, 10353-10365, doi,10.5194/acp-12-10353-2012, 2012

Harrison, R. G., and K. S. Carslaw, Ion-aerosol-cloud processes in the lower atmosphere, *Rev. Geophys*., 41, 1012, doi,10.1029/2002RG000114, 3, 2003

Heald, C. L. et al. Atmospheric ammonia and particulate inorganic nitrogen over the United States. *Atmos. Chem. Phys*. 12, 10295–10312 (2012).

Hennigan, C. J., Izumi, J., Sullivan, A. P., Weber, R. J., and Nenes, A., A critical evaluation of proxy methods used to estimate the acidity of atmospheric particles, *Atmos. Chem. Phys*., 15, 2775-2790, doi,10.5194/acp-15-2775-2015, 2015

Henneman, L.R.F., Liu, C., Hu, Y., Mulholland, J.A., Russell, A.G. (in review). "Air quality modeling for accountability research, Operational, dynamic, and diagnostic evaluation."

Hu, X.-M., P. M. Klein, and M. Xue, (2013), Evaluation of the updated YSU planetary boundary layer scheme within WRF for wind resource and air quality assessments, *J. Geophys. Res. Atmos*., 118, 10,490–10,505, doi,10.1002/jgrd.50823, 2013.

Huang, D.D., Seinfeld, J.H. and Marlow, W.H., BGK equation solution of coagulation for large Knudsen number aerosols with a singular attractive contact potential. *J. Colloid Interface Sci*., 140, 258-276, https,//doi.org/10.1016/0021-9797(90)90341-K, 1990

Husar, R.B., Whitby, K.T., Liu, B.Y.H., Physical mechanisms governing the dynamics of Los Angeles smog aerosol, *Journal of Colloid and Interface Science*, Volume 39, Issue 1, 1972, Pages 211-224, ISSN 0021-9797, https://doi.org/10.1016/0021-9797(72)90155-5.

Jacobs, M.I., Darer, A.I., and Elrod, M.J., Rate Constants and Products of the OH Reaction with Isoprene-Derived Epoxides, *Environmental Science & Technology* **2013** *47* (22), 12868-12876 DOI, 10.1021/es403340g

Karydis, V. A., Tsimpidi, A. P., Pozzer, A., Astitha, M., and Lelieveld, J., Effects of mineral dust on global atmospheric nitrate concentrations, *Atmos. Chem. Phys*., 16, 1491-1509, doi,10.5194/acp-16-1491-2016, 2016.

Kauppinen, E.I., Hillamo, R.E., Aaltonen, S.H., Sinkko, K.T.S. Radioactivity Size Distributions of Ambient Aerosols in Helsinki, Finland, during May 1986 after the Chernobyl accident, Preliminary Report. *Environ. Sci. Technol*., 20, 1257-1259, doi, 10.1021/es00154a01, 1986

Kim, Y.-H., Yiacoumi, S., Lee, I., McFarlane, J., Tsouris, C., Influence of radioactivity on surface charging and aggregation kinetics of particles in the atmosphere, *Environ. Sci. Technol*., 48, 182-189, doi, 10.1021/es4047439, 2014

Kim, Y.-H., Yiacoumi, S., and Tsouris, C., Surface charge accumulation of particles containing radionuclides in open air, *J. Environ. Radioactivity*, 143, 91-99, doi, 10.1016/j.jenvrad.2015.02.017, 2015

Kim, Y.-H., Yiacoumi, S., Nenes, A., and Tsouris, C., Incorporating radioactive decay into charging and coagulation of multicomponent radioactive aerosols, *J. Aerosol. Sci*., 114, 283-300, https://doi.org/10.1016/j.jaerosci.2017.09.024, 2017

Kim, Y.-H., Yiacoumi, S., Nenes, A., and Tsouris, C., Charging and coagulation of radioactive and nonradioactive particles in the atmosphere. *Atmos. Chem. Phys*., 16, 3449-3462, doi, 10.5194/acp-16-3449-2016, 2016

Kim, P. S., Jacob, D. J., Fisher, J. A., Travis, K., Yu, K., Zhu, L., Yantosca, R. M., Sulprizio, M. P., Jimenez, J. L., Campuzano-Jost, P., Froyd, K. D., Liao, J., Hair, J. W., Fenn, M. A., Butler, C. F., Wagner, N. L., Gordon, T. D., Welti, A., Wennberg, P. O., Crounse, J. D., St. Clair, J. M., Teng, A. P., Millet, D. B., Schwarz, J. P., Markovic, M. Z., and Perring, A. E., Sources, seasonality, and trends of southeast US aerosol, an integrated analysis of surface, aircraft, and satellite observations with the GEOS-Chem chemical transport model, *Atmos. Chem. Phys*., 15, 10411-10433, doi,10.5194/acp-15-10411-2015, 2015.

Kleindienst, T.E., Jaoui, M., Lewandowski, M., Offenberg, J.H., Lewis, C.W., Bhave, P.V., Edney, E.O., Estimates of the contributions of biogenic and anthropogenic hydrocarbons to secondary organic aerosol at a southeastern US location, *Atmospheric Environment*, Volume 41, Issue 37, December 2007, Pages 8288-8300, ISSN 1352-2310, http://dx.doi.org/10.1016/j.atmosenv.2007.06.045.

Langmann, B. (2013). Volcanic Ash versus Mineral Dust, Atmospheric Processing and Environmental and Climate Impacts. ISRN *Atmospheric Sciences*. 2013. . 10.1155/2013/245076

Laskin, A., R. C. Moffet, M. K. Gilles, J. D. Fast, R. A. Zaveri, B. B. Wang, P. Nigge, and J. Shutthanandan (2012), Tropospheric chemistry of internally mixed sea salt and organic particles, Surprising reactivity of NaCl with weak organic acids, *Journal Of Geophysical Research-Atmospheres*, 117, D017743.

Lee, Y., P. Adams. A fast and efficient version of the two-moment aerosol sectional (TOMAS) global aerosol microphysics model. *Aerosol. Sci. Technol*., 46 (6), 678-689, doi, 10.1080/02786826.2011.643259, 2012

Li, W., Xu, L., Liu, X., Zhang, J., Lin, Y., Yao, X., Gao, H., Zhang, D., Chen, J., Wang, W., Harrison, R., Zhang, X., Shao, L., Fu, P., Nenes, A., Shi, Z. Air pollution- aerosol interactions produce more bioavailable iron for ocean ecosystems. Sci. Adv. 2017, 3, e1601749 Li, J., W.-C. Wang, H. Liao, and W. Chang. 2014. Past and future direct radiative forcing of nitrate aerosol in East Asia. *Theor. Appl. Climatol*. 1–14. doi,10.1007/s00704-014-1249-1

Lin, Y.-H., Zhang, H., Pye, H. O. T., Zhang, Z., Marth, W. J., Park,S., Arashiro, M., Cui, T., Budisulistiorini, S. H., Sexton, K. G., Vizuete, W., Xie, Y., Luecken, D. J., Piletic, I. R., Edney, E. O., Bartolotti, L. J., Gold, A., and Surratt, J. D., Epoxide as a precursor to secondary organic aerosol formation from isoprene photooxidation in the presence of nitrogen oxides, *P. Natl. Acad. Sci*. USA, 110, 6718–6723, doi,10.1073/pnas.1221150110, 2013.

Liu, Y., Wu Z., Wang, Y., Xiao, Y., Gu, F., Zheng, J., Tan, T, Shang, D., Wu, Y., Zeng, L., Hu, M., Bateman, A. P., and Martin, S.T., Submicrometer Particles Are in the Liquid State during Heavy Haze Episodes in the Urban Atmosphere of Beijing, China, *Environmental Science & Technology Letters Article ASAP*, doi, 10.1021/acs.estlett.7b00352, 2017

Liu, Y., Wu Z., Wang, Y., Xiao, Y., Gu, F., Zheng, J., Tan, T, Shang, D., Wu, Y., Zeng, L., Hu, M., Bateman, A. P., and Martin, S.T., Submicrometer Particles Are in the Liquid State during Heavy Haze Episodes in the Urban Atmosphere of Beijing, China, *Environmental Science & Technology Letters Article ASAP*, DOI, 10.1021/acs.estlett.7b00352, 2017

Lujanienė, G., Aninkevičius, V., Lujanas, V., Artificial radionucleotides in the atmosphere over Lithuania, *J. Environ. Radioactivity*, 100(2), 108-119, doi,10.1016/j.jenvrad.2007.07.015, 2007

Maisels, A., Kruis, F.E., and Fissan, H. Mixing selectivity in bicomponent, bipolar aggregation. *J. Aerosol Sci*., 33, 35-49, https,//doi.org/10.1016/S0021-8502(01)00070-2, 2002a

Maisels, A., Kruis, F.E., and Fissan, H. Determination of coagulation coefficients and aggregation kinetics for charged aerosols. *J. Colloid Interface Sci*., 255, 332-340, https,//doi.org/10.1006/jcis.2002.8657, 2002b

Marais, E. A., Jacob, D. J., Jimenez, J. L., Campuzano-Jost, P., Day, D. A., Hu, W., Krechmer, J., Zhu, L., Kim, P. S., and Miller, C. C., Aqueous-phase mechanism for secondary organic aerosol formation from isoprene, application to the southeast United

States and co-benefit of SO 2 emission controls, *Atmospheric Chemistry and Physics*, 16, 1603-1618, 2016.

Marlow, W.H., Derivation of aerosol collision rates for singular attractive contact potentials. *J. Chem. Phys*. 73, 6284-6287, https,//doi.org/10.1063/1.440126. 1980

Masson, O., Baeza, A., Bieringer, J., Brudecki, K., Bucci, S., Cappai, M., Carvalho, F.P., Connan, O., Cosma, C., Dalheimer, A., Didier, D., Depuydt, G., De Geer, L.E., De Vismes, A. , Gini, L., Groppi, F., Gudnason, K., Gurriaran, R., Hainz, D., Halldórsson, Ó., Hammond, D., Hanley, O., Holeý, K., Homoki, Zs., Ioannidou, A., Isajenko, K., Jankovic, M., Katzlberger, C., Kettunen, M., Kierepko, R., Kontro, R., Kwakman, P.J.M., Lecomte, M., Vintro, L.L., Leppänen, A.-P., Lind, B., Lujaniene, G. , Ginnity, P.M., Mahon, C. M., Malá, H., Manenti, S. , Manolopoulou, M., Mattila, A., Mauring, A., Mietelski, J.W., Møller, B., Nielsen, S.P. , Nikolic, J., Overwater, R.M.W., Pálsson, S. E., Papastefanou, C., Penev, I., Pham, M.K., Povinec, P.P., Ramebäck, H., Reis, M.C., Ringer, W., Rodriguez, A., Rulík, P., Saey, P.R.J., Samsonov, V., Schlosser, C., Sgorbati, G., Silobritiene, B.V., Söderström, C., Sogni, R., Solier, L., Sonck, M., Steinhauser, G., Steinkopff, T., Steinmann, P., Stoulos, S., Sýkora, I., Todorovic, D., Tooloutalaie, N., Tositti, L., Tschiersch, J., Ugron, A., Vagena, E., Vargas, A., Wershofen, H., Zhukova, O. Tracking of Airborne Radionuclides from the Damaged Fukushima Dai-Ichi Nuclear Reactors by European Networks. *Environ. Sci. Technol*., 45, 7670-7677, doi, 10.1021/es2017158, 2011

McBride, J.P., Moore, R.E., Witherspoon, J.P., Blanco, R.E., Radiological impact of airborne effluents of coal and nuclear-plants, *Science*, 202, 4372, 1045-1050 doi, 10.1126/science.202.4372.1045, 1978

Meskhidze, N., Chameides, W. L., Nenes, A. & Chen, G. Iron mobilization in mineral dust, can anthropogenic SO2 emissions affect ocean productivity? *Geophys. Res. Lett*. 30, 2085 (2003).

Mohnen, V. A., Formation, Nature, and Mobility of Ions of Atmospheric Importance, in Electrical Processes in Atmospheres, H. Dolezalek, R. Reiter, and H. Landsberg, eds., Steinkopff, Darmstadt, Germany, pp. 1–17, doi, 10.1007/978-3-642-85294-7_1, 1976

Mulpuru, S.R., Pellow, M.D., Cox, D.S., Hunt, C.E.L., Barrand, R.D. Characteristics of Radioactive Aerosols Generated from a Hot Nuclear Fuel Sample. *J. Aerosol Sci*., 23, S827-S830, doi, 10.1016/0021-8502(92)90539-8, 1992

Myriokefalitakis, S., Nenes, A., Baker, A. R., Mihalopoulos, N., and Kanakidou, M.: Bioavailable atmospheric phosphorous supply to the global ocean: a 3-D global modeling study, Biogeosciences, 13, 6519-6543, https://doi.org/10.5194/bg-13-6519-2016, 2016.

Nguyen, T. B., Coggon, M. M., Bates, K. H., Zhang, X., Schwantes, R. H., Schilling, K. A., Loza, C. L., Flagan, R. C., Wennberg, P. O., and Seinfeld, J. H., Organic aerosol formation from the reactive uptake of isoprene epoxydiols (IEPOX) onto non-acidified inorganic seeds, *Atmos. Chem. Phys*., 14, 3497-3510, doi,10.5194/acp-14-3497-2014, 2014a.

Nguyen, T. K. V., Petters, M. D., Suda, S. R., Guo, H., Weber, R. J., and Carlton, A. G.: Trends in particle-phase liquid water during the Southern Oxidant and Aerosol Study, *Atmos. Chem. Phys.*, 14, 10911-10930, https://doi.org/10.5194/acp-14-10911-2014, 2014.

Offenberg, J. H., Lewandowski, M., Jaoui, M., and Kleindienst, T. E., Contributions of biogenic and anthropogenic hydrocarbons to secondary organic aerosol during 2006 in Research Triangle Park, NC, *Aerosol and Air Quality Resarch*, 11, 99-108, 2011.

Ooe, H., Seki, R., Ikeda, N., Particle-size distribution of fission products in airborne dust collected at Tsukuba from April to June 1986., *J. Environ. Radioactivity*, 6(3), 219-223, doi, 10.1016/0265-931x(88)90078-1, 1988

Park, R. J., Jacob, D. J., Kumar, N. and Yantosca, R. N., Regional visibility statistics in the United States, Natural and transboundary pollution influences, and implications for the regional haze rule. *Atmospheric Environment* 40(28), 5405-5423, doi.org/10.1016/j.atmosenv.2006.04.059, 2006

Paulot, F., Crounse, J. D., Kjaergaard, H. G., Kurten, A., St Clair, J. M., Seinfeld, J. H., Wennberg, P. O. Unexpected epoxide formation in the gas-phase photooxidation of isoprene. *Science* 2009, 325, 730−733

Pinder, R. W., Gilliland, A. B. & Dennis, R. L. Environmental impact of atmospheric NH3 emissions under present and future conditions in the eastern United States. *Geophys. Res. Lett*. 35, L12808 (2008).

Pinder, R. W., Adams, P. J. & Pandis, S. N. Ammonia emission controls as a cost-effective strategy for reducing atmospheric particulate matter in the eastern United States. *Environ. Sci. Technol.* 41, 380–386 (2007).

Pye, H. O. T., H. Liao, S. Wu, L. J. Mickley, D. J. Jacob, D. K. Henze, and J. H. Seinfeld (2009), Effect of changes in climate and emissions on future sulfate-nitrate-ammonium aerosol levels in the United States, *J. Geophys. Res*., 114, D01205, doi,10.1029/2008JD010701.

Pye, H. O. T., Pinder, R. W., Piletic, I. R., Xie, Y., Capps, S. L., Lin, Y.-H., Surratt, J. D., Zhang, Z., Gold, A., Luecken, D. J., Hutzell, W. T., Jaoui, M., Offenberg, J. H., Kleindienst, T. E., Lewandowski, M., Edney, E. O. (2013) Epoxide Pathways Improve Model Predictions of Isoprene Markers and Reveal Key Role of Acidity in Aerosol Formation. *Environmental Science & Technology*, 47 (19), 11056–11064.

Pye, H. O. T., Zuend, A., Fry, J. L., Isaacman-VanWertz, G., Capps, S. L., Appel, K. W., Foroutan, H., Xu, L., Ng, N. L., and Goldstein, A. H., Coupling of organic and inorganic aerosol systems and the effect on gas–particle partitioning in the southeastern US, *Atmos. Chem. Phys*., 18, 357-370, https,//doi.org/10.5194/acp-18-357-2018, 2018.

Renard, J.-B., Tripathi, S. N., Michael, M., Rawal, A., Berthet, G., Fullekrug, M., Harrison, R. G., Robert, C., Tagger, M., and Gaubicher, B., In situ detection of electrified aerosols in the upper troposphere and stratosphere, *Atmos. Chem. Phys*., 13, 11187–11194, doi,10.5194/acp-13-11187-2013, 2013

Saylor, R., Myles, L., Sibble, D., Caldwell, J. & Xing, J. Recent trends in gas-phase ammonia and PM2.5 ammonium in the southeast United States. *J. Air Waste Manage. Assoc*. 65, 347–357 (2015).

Seinfeld, J.H., Pandis, S.N., Atmospheric Chemistry and Physics, From Air Pollution to Climate Changes. Wiley, New York, USA ISBN, 0-471-17815-2, 2006

Simons, S. The Coagulation and Deposition of Radioactive Aerosols. *Ann. Nucl. Energy*, 8, 287-294, doi, 10.1016/0306-4549(81)90094-3, 1981

Simon, H., Baker, R., Sharon., K. & P., Compilation and interpretation of photochemical model performance statistics published between 2006 and 2012. *Atmospheric Environment*. 61. 124–139, doi,10.1016/j.atmosenv.2012.07.012, 2012

Silvern, R. F., Jacob, D. J., Kim, P. S., Marais, E. A., Turner, J. R., Campuzano-Jost, P., and Jimenez, J. L., Inconsistency of ammonium–sulfate aerosol ratios with thermodynamic models in the eastern US, a possible role of organic aerosol, *Atmos. Chem. Phys*., 17, 5107-5118, doi,10.5194/acp-17-5107-2017, 2017

Skamarock, W.C., Klemp, J, Dudhia, Jimy, Gill, D.O., Barker, Dale, Wang, W, Powers, J.G, A Description of the Advanced Research WRF Version 3. NCAAR, 27. 3-27, 2008

Sow, M., Lemaitre, P., Influence of electric charges on the washout efficiency of atmospheric aerosols by raindrops. *Ann. Nucl. Energy*, 93, 107-113, doi,10.1016/j.anucene.2015.12.036, 2016

Spielman, L. A., Viscous interactions in Brownian coagulation, *J. Colloid Interface Sci*. 33, 562 doi, 10.1016/0021-9797(70)90008-1, 1970

Stockdale, A., Krom, M.D., Mortimer, R.J.G., Benning, L.G., Carslaw, K., Herbert, R., Shi, Z., Nenes, A, Understanding the nature of atmospheric acid processing of mineral dusts in supplying bioavailable phosphorus to the oceans, *Proc.Nat.Acad.Sci*., doi:10.1073/pnas.1608136113, 2016

Surratt, J. D., Chan, A. W. H., Eddingsaas, N. C., Chan, M. N., Loza, C. L., Kwan, A. J., Hersey, S. P., Flagan, R. C., Wennberg, P. O., Seinfeld, J. H. (2010) Reactive Intermediates Revealed in Secondary Organic Aerosol Formation from Isoprene. *Proceedings of the National Academy of Sciences of the United States of America*, 107 (15), 6640–6645.

Travis, K. R., Jacob, D. J., Fisher, J. A., Kim, P. S., Marais, E. A., Zhu, L., Yu, K., Miller, C. C., Yantosca, R. M., Sulprizio, M. P., Thompson, A. M., Wennberg, P. O., Crounse, J. D., St. Clair, J. M., Cohen, R. C., Laughner, J. L., Dibb, J. E., Hall, S. R., Ullmann, K., Wolfe, G. M., Pollack, I. B., Peischl, J., Neuman, J. A., and Zhou, X., Why do models overestimate surface ozone in the Southeast United States?, *Atmos. Chem. Phys*., 16, 13561-13577, https,//doi.org/10.5194/acp-16-13561-2016, 2016.

Tripathi, S., Harrison R. G., Scavenging of electrified radioactive aerosol. *Atmos. Environ*., 35, 5817-5821, doi,10.1016/S1352-2310(01)00299-0, 2001

Tsimpidi, A. P., Karydis, V. A. & Pandis, S. N. Response of inorganic fine particlulate matter to emission changes of sulfur dioxide and ammonia, the eastern United States as a case study. *J. Air Waste Manage. Assoc*. 57, 1489–1498 (2007).

Tzivion, S., Feingold, G., Levin, Z. An Efficient Numerical Solution to the Stochastic Collection Equation. *J. Atmos. Sci*., 44, 3139-3149, doi, 10.1175/1520-0469(1987)044<3139,AENSTT>2.0.CO,2, 1987

Vayenas, D. V., S. Takahama, C. I. Davidson, and S. N. Pandis, Simulation of the thermodynamics and removal processes in the sulfate-ammonia-nitric acid system during winter, Implications for PM2.5 control strategies, *J. Geophys. Res*., 110, D07S14, doi,10.1029/2004JD005038, 2005

Vukovich, J. and Pierce, T., The Implementation of BEIS3 withinthe SMOKE Modeling Framework, in, Proceedings of the 11th International Emissions Inventory Conference, Atlanta, Georgia, available at, www.epa.gov/ttn/chief/conference/ei11/modeling/vukovich.pdf, 15–18 April 2002

Wang, C., Yuan, T., Wood, S. A., Goss, K.-U., Li, J., Ying, Q., and Wania, F., Uncertain Henry's law constants compromise equilibrium partitioning calculations of atmospheric oxidation products, *Atmos. Chem. Phys*., 17, 7529-7540, https,//doi.org/10.5194/acp-17-7529-2017, 2017.

Wang, G., Zhang, R., Gomez, M. E., Yang, L., Levy Zamora, M., Hu, M., Lin, Y., Peng, J., Guo, S., Meng, J., Li, J., Cheng, C., Hu, T., Ren, Y., Wang, Y., Gao, J., Cao, J., An, Z., Zhou, W., Li, G., Wang, J., Tian, P., Marrero-Ortiz, W., Secrest, J., Du, Z., Zheng, J., Shang, D., Zeng, L., Shao, M., Wang, W., Huang, Y., Wang, Y., Zhu, Y., Li, Y., Hu, J., Pan, B., Cai, L., Cheng, Y., Ji, Y., Zhang, F., Rosenfeld, D., Liss, P. S., Duce, R. A., Kolb, C. E., and Molina, M. J.: Persistent sulfate formation from London Fog to Chinese haze, *P. Natl. Acad. Sci* USA, 113, 13630–13635, doi:10.1073/pnas.1616540113, 2016.

Weber, R. J., et al. (2007), A study of secondary organic aerosol formation in the anthropogenic-influenced southeastern United States, *J. Geophys. Res.*, 112, D13302, doi,10.1029/2007JD008408.

Weber, R.J., Guo, H., Russell, A.G., Nenes, A. (2016) High aerosol acidity despite declining atmospheric sulfate concentrations over the past 15 years, *Nature Geosci*., doi,10.1038/ngeo2665

West, J. J., Ansari, A. S. & Pandis, S. N. Marginal PM2.5, nonlinear aerosol mass response to sulfate reductions in the eastern United States. *J. Air Waste Manage. Assoc*. 49, 1415–1424 (1999).

Wexler, A. S., and S. L. Clegg, Atmospheric aerosol models for systems including the ions H+, NH4+, Na+, SO42−, NO3−, Cl−, Br−, and H2O, *J. Geophys. Res.*, 107(D14), DOI, 10.1029/2001JD000451, 2002, http,//www.aim.env.uea.ac.uk/aim/aim.php

Xu, L., Guo, H., Boyd, C., Klein, M., Bougiatioti, A., Cerully, K., Hite, J., Isaacman-VanWertz, G., Kreisberg, N. M., Knote, C., Olson, K., Koss, A., Goldstein, A., Hering, S. V., de Gouw, J., Baumann, K., Lee, S. H., Nenes, A., Weber, R. J., Ng, N. L. Effects of anthropogenic emissions on aerosol formation from isoprene and monoterpenes in the southeastern United States. *Proc. Natl. Acad. Sci.* U. S. A. 2014, 112 (1), 37−42.

Yoschenko, V. I., Kashparov, V. A., Protsak, V. P., Lundin, S. M., Levchuk, S. E., Kadygrib, A. M., Zvarich, S. I., Khomutinin, Yu. V., Maloshtan, I.M., Lanshin, V. P., Kovtun, M. V., and Tschiersch, J., Resuspension and redistribution of radionucleotides during grassland and forest fires in the Chernobyl exclusion zone. Part I, fire experiments, *J. Environ. Radioactivity*, 86 (2), 143-163, doi, 10.1016/j.jenvrad.2005.08.003, 2006

Yoschenko, V. I., Kashparov, V. A., Levchuk, S. E., Glukhovskiy, A. S., Khomutni, Y. V., Protsak, V. P., Lundin, S. M., Tschiersch, J., Resuspension and redistribution of radionucleotides during grassland and forest fires in the Chernobyl exclusion zone. Part II,

modeling the transport process, *J. Environ. Rad*., 87, 260-278, doi, 10.1016/j.jenvrad.2005.08.003, 2006

Yoshida, N., Kanda, J. Tracking the Fukushima Radionuclides. *Science*, 336, 1115-1116, doi, 10.1126/science.1219493, 2012